

The Electronic and Optical Properties of Close Packed Cadmium Selenide Quantum Dot Solids

by

Cherie Renee Kagan

B. S. E. Materials Science and Engineering
B. A. Mathematics
University of Pennsylvania, Philadelphia, PA 1991

Submitted to the Department of Materials Science and Engineering
in Partial Fulfillment of the Requirements
for the Degree of

DOCTOR OF PHILOSOPHY

at the

MASSACHUSETTS INSTITUTE OF TECHNOLOGY

September 1996

© 1996 Massachusetts Institute of Technology
All rights reserved

Signature of the Author _____
Department of Materials Science and Engineering
August 9, 1996

Certified by _____
Moungi G. Bawendi
Professor of Chemistry
Thesis Supervisor

Accepted by _____
Linn W. Hobbs
John F. Elliott Professor of Materials Science and Engineering
Chair, Department Committee on Graduate Students

ARCHIVES

MASSACHUSETTS INSTITUTE
OF TECHNOLOGY

SEP 27 1996

LIBRARIES



Room 14-0551
77 Massachusetts Avenue
Cambridge, MA 02139
Ph: 617.253.2800
Email: docs@mit.edu
<http://libraries.mit.edu/docs>

DISCLAIMER OF QUALITY

Due to the condition of the original material, there are unavoidable flaws in this reproduction. We have made every effort possible to provide you with the best copy available. If you are dissatisfied with this product and find it unusable, please contact Document Services as soon as possible.

Thank you.

The images contained in this document are of the best quality available.

The Electronic and Optical Properties of Close Packed Cadmium Selenide Quantum Dot Solids

by

Cherie Renee Kagan

Submitted to the Department of Materials Science and Engineering on August 9, 1996
in Partial Fulfillment of the Requirements for the Degree of
Doctor of Philosophy in Materials Science and Engineering

Abstract

The synthesis, structural characterization, optical spectroscopy, and electronic characterization of close packed solids prepared from CdSe QD samples tunable in size from 17 to 150 Å in diameter ($\sigma < 4.5\%$) are presented. We control the deposition of 3D QD glasses and superlattices by tailoring the solvent composition used to deposit the QD solids. We use high resolution scanning and transmission electron microscopies and small-angle x-ray scattering to develop a well-defined structural model for glassy and ordered solids. Locally the QDs in the solids are close packed with an interdot spacing of 11 ± 1 Å maintained by organic ligands coordinating the QD surfaces.

We show spectroscopically that electronic energy transfer occurs between proximal QDs in the solids and arises from dipole-dipole interdot interactions. In well-intermixed QD solids of small and large dots, we measure quenching of the luminescence (lifetime) of the small dots accompanied by enhancement of the luminescence (lifetime) of the large dots consistent with electronic energy transfer from the small to the large dots. In QD solids of single size dots, a red shifted and modified emission lineshape is consistent with electronic energy transfer within the sample inhomogeneous distribution. We use Förster's theory for long-range resonance transfer through dipole-dipole interdot interactions to explain electronic energy transfer in these QD solids.

We demonstrate photoconductivity in the QD solids. We measure the photocurrent as a function of excitation energy, voltage, excitation intensity, and temperature to uncover the carrier generation, separation, and transport mechanisms. The spectral response of the photocurrent follows the absorption spectra for the QD solids demonstrating carrier generation in the QDs. The photocurrent is linear with incident intensity consistent with a carrier generation efficiency that is scaled by the photon flux. The photocurrent exhibits an anomalous temperature dependence, reaching a maximum at ~ 75 K, consistent with a thermally activated process that is overcome at higher temperatures by the decreasing exciton lifetime. The I-V curves are nonlinear, independent of excitation energy and photon flux. We present three possible models, describing field-assisted charge separation, collective transport of carriers, and carrier tunneling, to explain the photoconductive properties of QD solids.

Thesis Supervisor: Mounji G. Bawendi, Ph.D.

Title: Professor of Chemistry

To My Family

Table of Contents

	<u>Page</u>
Title Page	1
Abstract	3
Dedication	5
Table of Contents	7
List of Figures	11
Chapter 1 Introduction	13
1.1 The Individual CdSe Quantum Dot (QD)	13
1.2 Close Packed CdSe QD Solids	16
1.3 Dipolar Coupling and Electronic Energy Transfer	19
1.4 Electronic Coupling and Photoconductivity	20
1.5 Summary	21
Chapter 2 Synthesis, Structural Characterization, and Optical Spectroscopy of Close Packed CdSe Quantum Dot Solids	23
2.1 Introduction	23
2.2 Experimental	24
2.2.1 Synthesis of CdSe QDs	24
2.2.2 QD Glasses	25
2.2.3 QD Superlattices	26
2.2.4 Structural Characterization	26
2.2.5 Optical Spectroscopy	27
2.3 Results and Discussion	27
2.3.1 Two-dimensional QD Monolayers	27
2.3.2 Three-dimensional QD Glasses	31
2.3.3 Three-dimensional QD Superlattices	38
2.3.4 Mixed Glassy and Ordered Solids of Small and Large QDs	68
2.3.5 Optical Absorption and Emission Spectra for Close Packed CdSe QD Solids	68
2.3.6 Room Temperature Photochemistry of QD Solids	76
2.4 Conclusion	78
Chapter 3 Preliminary Observations of Electronic Energy Transfer in Close Packed CdSe Quantum Dot Solids	79
3.1 Introduction	79
3.2 Experimental	80
3.3 Results	81
3.3.1 Structural Characterization	81

	<u>Page</u>
3.3.2 Optical Spectroscopy	83
3.4 Discussion	86
3.5 Conclusion	90
 Chapter 4 Long-Range Resonance Transfer of Electronic Excitations in Close Packed CdSe Quantum Dot Solids	 91
4.1 Introduction	91
4.2 Experimental	93
4.3 Structural Characterization	94
4.4 Optical Spectroscopy	95
4.5 Mixed CdSe QD Solid	98
4.5.1 Spectral Overlap of Donor Emission and Acceptor Absorption	103
4.5.2 Time Dependence of Electronic Energy Transfer	104
4.5.2.1 Long-Range Resonance Transfer	106
4.5.2.2 Exciton Diffusion	108
4.5.3 Quenching of the Luminescence Quantum Yield of the Small Dots	108
4.5.4 Summary	109
4.6 Single Size CdSe QD Solids	109
4.6.1 Sample Inhomogeneous Distribution	111
4.6.2 Probability of Electronic Energy Transfer	112
4.6.3 Simulation of Energy Transfer within the Sample Inhomogeneous Distribution	113
4.6.4 Effects of Sample Inhomogeneous Distribution	114
4.6.5 Concentration Dependence of Electronic Energy Transfer	116
4.7 Conclusion	116
 Chapter 5 Photoconductivity in Close Packed CdSe Quantum Dot Solids	 119
5.1 Introduction	119
5.2 Experimental	121
5.3 Results	127
5.3.1 Structural Characterization of QD Solid/Electrodes	127
5.3.2 Voltage Dependence of Photocurrent	131
5.3.3 Spectral Response of Photocurrent	131
5.3.4 Intensity Dependence of Photocurrent	136
5.3.5 Temperature Dependence of Photocurrent	138
5.3.6 Effects of the Electric Field on the Photoluminescence of the QD Solid	144
5.4 Discussion	144
5.4.1 Charge Generation and Separation	144
5.4.2 Onsager Model of Field-Assisted Charge Separation	147
5.4.3 The Scaling Law for Collective Transport of Carriers	157
5.4.4 Tunneling	159
5.4.5 Exciton Interaction with Electrodes	161

	<u>Page</u>
5.4.6 Two Quantum Processes	161
5.4.7 Multiple Trapping	161
5.4.8 Polarization	162
5.5 Conclusion	163
Bibliography	165
Acknowledgments	169

List of Figures

	<u>Page</u>
Figure 1.1	Electronic Structure of the Individual CdSe QD 14
Figure 1.2	Individual QD versus Coupled QDs 16
Figure 1.3	Local Ordering of Close Packed QD Solids 18
Figure 2.1	Monolayer of Close Packed CdSe QDs 29
Figure 2.2	QD Glass, Nanostructure and Microstructure 33
Figure 2.3	Small-angle X-ray Scattering of QD Glasses 36
Figure 2.4	Self-assembled Islands of Close Packed QDs 41
Figure 2.5	Islands of QDs Coalescing 45
Figure 2.6	3D QD Superlattices, Epitaxial Thin Films 49
Figure 2.7	Transition from Ordered to Glassy Deposition of QD Solid 53
Figure 2.8	Colloidal Crystals 57
Figure 2.9	Spatial Organization of Colloidal Crystals 61
Figure 2.10	Optical Micrograph of Colloidal Crystals 65
Figure 2.11	HRTEM and Small-angle X-ray Scattering of fcc QD Superlattice 67
Figure 2.12	Mixed Glassy and Ordered QD Solids 71
Figure 2.13	Room Temperature Optical Absorption and Emission for Close Packed CdSe QD Solids 73
Figure 2.14	Temperature Dependence of Absorption Spectra 75
Figure 2.15	Room Temperature Photochemistry of QD Solids 77
Figure 3.1	Small-angle X-ray Scattering for QDs in Mixed System 82
Figure 3.2	Optical Absorption and Emission for Mixed System of QDs Dispersed in Solution versus Close Packed into a Solid 84
Figure 3.3	Photoluminescence Excitation for Mixed System of QDs 85
Figure 3.4	Luminescence Decays for Pure and Mixed QD Solids 87
Figure 4.1	10 K Optical Absorption and Emission for Close Packed QD Solids 96
Figure 4.2	Cartoon Depicting Energy Transfer in the Mixed System of QDs 99
Figure 4.3	RT and 10 K Spectral Overlap 100
Figure 4.4	RT and 10 K Absorption Spectra for Pure and Mixed QD Solids 101
Figure 4.5	RT and 10 K Luminescence Spectra for a Mixed QD Solution and for Pure and Mixed QD Solids 102
Figure 4.6	Luminescence Decays, Comparison of Energy Transfer Mechanisms 105
Figure 4.7	Comparison of Luminescence Spectra for QDs Dispersed in Solutions and Close Packed into Solids 110
Figure 4.8	Effects of Sample Spectral Inhomogeneity on Energy Transfer Effects 115
Figure 4.9	Concentration Dependence of Luminescence Spectrum 117
Figure 5.1	Sample Design for Photoconductivity Measurements 122
Figure 5.2	Electrical Connections for Photoconductivity Measurements 124
Figure 5.3	Laser Setup for Photoconductivity Measurements 125
Figure 5.4	Image of QD Solid on Patterned Substrate 129
Figure 5.5	I-V Curves Showing Nonlinear Behavior 132
Figure 5.6	Spectral Response of Photocurrent for a 30.3 Å CdSe QD Solid 133

	<u>Page</u>
Figure 5.7 Spectral Response of Photocurrent for a 41.4 Å CdSe QD Solid	134
Figure 5.8 Spectral Response of Photocurrent for a 49.5 Å CdSe QD Solid	135
Figure 5.9 Intensity Dependence of Photocurrent	137
Figure 5.10 Temperature Dependence of I-V Curves for a 41.4 Å CdSe QD Solid	139
Figure 5.11 Temperature and Voltage Dependence of Maximum Photocurrent for a 41.4 Å CdSe QD Solid	140
Figure 5.12 Temperature Dependence of I-V Curves for a 49.5 Å CdSe QD Solid	141
Figure 5.13 Temperature and Voltage Dependence of Maximum Photocurrent for a 49.5 Å CdSe QD Solid	142
Figure 5.14 Temperature Dependence of I-V Curves for a 30.3 Å CdSe QD Solid	143
Figure 5.15 Effects of Electric Field on Photoluminescence	145
Figure 5.16 Band Diagram for QDs and Au Electrodes	149
Figure 5.17 Comparison of Experimental I-V Curves with Onsager Model and the Scaling Law	150
Figure 5.18 Original and Modified Onsager Model	152
Figure 5.19 Temperature Dependence of Absorption and Emission for a 41.4 Å CdSe QD Solid	155
Figure 5.20 Temperature Dependence of Absorption and Emission for a 49.5 Å CdSe QD Solid	156

Chapter 1

Introduction

1.1 The Individual CdSe Quantum Dot (QD)

Controlling the physical size of a material can be used to tune its electronic, optical, and magnetic properties. The key is making the physical dimensions of the material small compared to the natural length scale characteristic of the materials property. In semiconductors, shrinking its dimensions to nanometer length scales comparable to the bulk exciton Bohr radius, the natural extent of the electron-hole pair, alters its electronic structure and optical properties. Reducing the size of a bulk solid in one direction produces a two-dimensional quantum well (QW). Excitations generated in the QW are free to move in the plane of the well, but their motion is confined in the reduced dimension. In the confined direction, an electronic carrier is like a “particle in a box,” occupying discrete energy levels¹.

The QD is the zero-dimensional analog of the two-dimensional QW. Nanometer size semiconductor QDs smaller than the bulk exciton Bohr radius strongly confine electronic excitations in all three dimensions. Photoexcitation of the QD creates an electron-hole pair which is confined to and delocalized over the volume of the dot [Fig. 1.1(a)]. The spectroscopic and photophysical properties of the QD are analogous to those of a large molecule. In the strong confinement regime, the electron and hole can be treated independently and the electronic structure of the QD can be modeled using simple effective mass theory². The effective mass approximation assumes parabolic conduction and valence bands, shown in Figure 1.1(b), with bulk effective masses for the electron and hole. Each carrier can be treated as a “particle in a sphere” bound at the QD surface by an infinite potential [Fig. 1.1(a)]. The electron and hole in the QD are

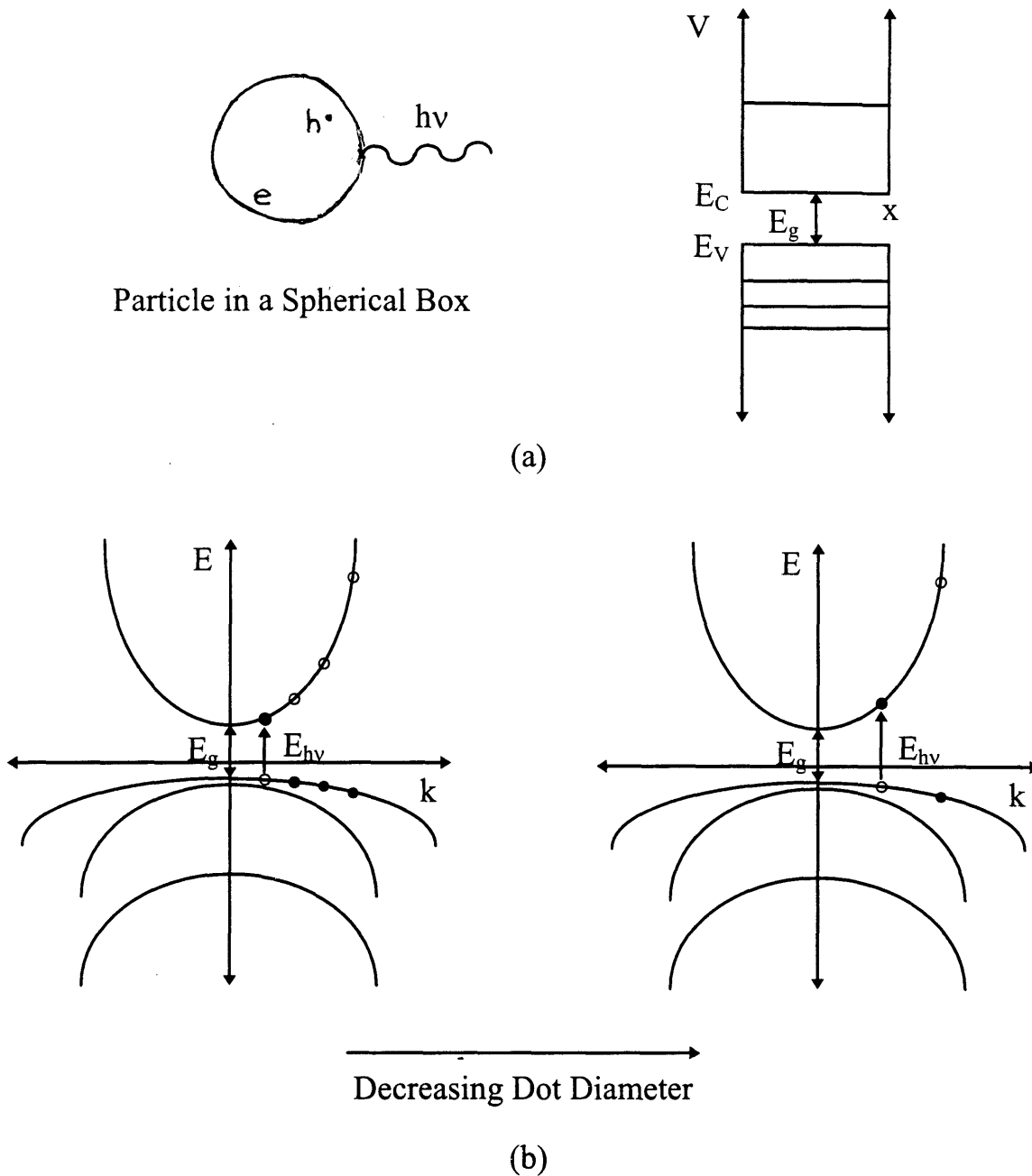


Figure 1.1 (a) Photoexcitation of a QD creates an electron-hole pair which is confined to and delocalized over the volume of the dot. The electron (hole) can be modeled as a particle in a sphere bound by an infinite potential at the surface of the QD. The electron and hole have hydrogenic wavefunctions and occupy discrete electronic states. (b) The bulk conduction and valence bands are assumed to be parabolic in the simple effective mass approximation. The energy diagrams show the complexity of the valence band for CdSe, important in the spectroscopy of the QDs³. The finite size of the QD quantizes the allowed k values. Decreasing the dot diameter shifts the first state to larger values of k and increases the separation between states. This is seen spectroscopically as a blue shift in the absorption edge and a larger separation between electronic transitions.

described by hydrogenic wavefunctions and occupy discrete electronic energy levels. The QD has been coined “the artificial atom” due to the atomic-like nature of its electronic wavefunctions and energy levels⁴.

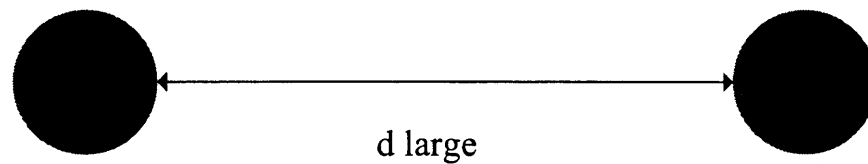
Three-dimensional confinement effects collapse the continuous density of states of the bulk solid into the discrete electronic states of the QD. This can be seen in Figure 1.1(b) where the finite size of the QD quantizes the allowed k values. Decreasing the diameter of the QD shifts the first state to larger k values and increases the separation between states. This is observed spectroscopically as a blue shift in the absorption edge and a larger separation between electronic transitions with decreasing dot diameter.

Advances in synthetic methods produce samples of CdSe QDs tunable in size from 17 to 150 Å in diameter with standard deviations <4.5%⁵. The sizes of the QDs are smaller than the bulk exciton Bohr radius in CdSe (56 Å)⁶. Each CdSe QD is a small chunk of the bulk CdSe lattice consisting of 100's to 10,000's of atoms, spanning the size regime from molecular species to bulk solid. The surface of the QD is coordinated by an organic monolayer which sterically stabilizes the dot in solution and electronically passivates its surface⁷. The quality of these samples has made it possible to observe, assign, and monitor the size evolution of a series of discrete, excited electronic states^{8,9}. These samples have strong band edge emission with luminescence quantum yields ranging from 0.1 to 0.9 at 10 K. Norris deduced the size dependent optical absorption and emission spectra of “single” CdSe QDs using transient differential absorption⁸, photoluminescence excitation⁹, and fluorescence line narrowing spectroscopies¹⁰. Agreement between experimental observations and theoretical calculations provides a framework for understanding the size dependent optical spectrum of individual CdSe QDs^{6,8-11}. Recent luminescence studies of single CdSe QDs reveal “ultra-narrow” homogeneous linewidths for the QD emission, significantly narrower than those obtained previously using fluorescence line narrowing¹². The electronic structure of the QD is truly “atomic-like.”

1.2 Close Packed CdSe QD Solids

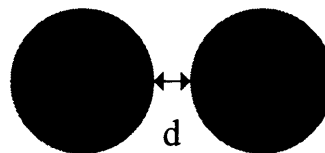
Previous studies have aimed at understanding the structural, electronic, and optical properties characteristic of individual QDs. Most studies have probed dilute samples of QDs where the distance between the dots is large and random and the dots behave as individual entities. Placing QDs in proximity raises the possibility of interdot couplings¹³ [Fig. 1.2].

Dilute in a Matrix



Individual Quantum Dot

Close Packed in the Solid



Coupled Quantum Dots

Figure 1.2 Cartoon. (a) When QDs are dilute in a matrix, the distance between QDs is large and random. Electronic and optical studies probe the characteristics of the individual QD. (b) Placing QDs in proximity, the QDs interact. Studies of proximal QDs probe a convolution of the individual properties of the QD and the collective properties of coupled QDs.

Building close packed QD solids presents opportunities to explore the collective physical phenomena that develop as proximal QDs interact and also the electronic and optical properties of new QD solid state materials. The QD solid provides a medium for potential novel electronic, optical, and optoelectronic applications which combine the unique properties of individual QDs and the collective properties of coupled QDs. Understanding the interactions between proximal QDs is the first step in designing QD solid state materials with tailored electronic and optical properties. Choosing both the size and composition of the QDs and the length and electronic structure of the matrix may be used to engineer new materials on the nanometer scale with tailored properties.

Recent advances in the fabrication of two- and three-dimensional QD solids by lithography¹⁴, molecular beam epitaxy¹⁵, and wet chemical routes¹⁶⁻¹⁸ make the study of interdot couplings possible. In chapter 2, we present a method to synthesize two- and three-dimensional glassy and ordered close packed QD solids^{16,18}. We control the deposition of QD glasses and superlattices by tailoring the composition of the solvents used to deposit the QD solids. We can also control the deposition of either ordered and oriented epitaxial thin films or colloidal crystals. Heterogeneous nucleation on an interface produces ordered and oriented epitaxial thin films. Homogeneous nucleation in solution forms colloidal crystals having regular geometries characteristic of its fcc lattice. In a mixed system of small and large QDs, deposition of an ordered QD solid leads to phase separation between the small and large dots. In a glassy QD solid the small and large dots remain well-intermixed. We use high resolution scanning and transmission electron microscopies in combination with small-angle x-ray scattering to establish a well-defined structural model for the QD glasses and superlattices. Small-angle x-ray scattering reveals the local ordering of the QDs in both glassy and ordered QD solids. The QD solids consists of close packed QDs with an interdot spacing of $11 \pm 1 \text{ \AA}$ maintained by the organic monolayer coordinating the surfaces of the QDs. Figure 1.3 is a cartoon depicting the local arrangement of QDs in glassy and ordered QD solids. At these small interdot separations, one might expect neighboring QDs to interact.

We can take advantage of our ability to prepare CdSe QD samples ranging in size from 17 to 150 \AA ($\sigma < 4.5\%$) in diameter to tune the electronic and optical properties of

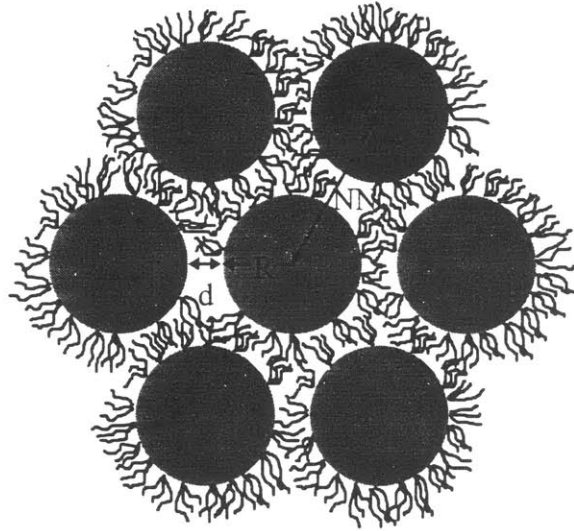


Figure 1.3 Cartoon depicting local arrangement of QDs in both glassy and ordered QD solids. The QDs are close packed with $d = 11 \pm 1 \text{ \AA}$.

the QD solids. Optical spectroscopy shows that the discrete, size dependent electronic transitions and sharp band edge emission characteristic of the individual QDs are maintained in the QD solids. We show some evidence for interdot couplings as the emission for QD solids is red shifted from that for QD solutions.

The QD solids are analogous to QW superlattices. Interwell couplings in QW heterostructures have long been observed and continue to be of great interest for both their fundamental physics and their device applications¹⁹. The QD solids are also similar to molecular solids in that the QDs behave like large molecules and the QD solids are weak van der Waals solids.

1.3 Dipolar Coupling and Electronic Energy Transfer

One possible interaction between proximal atoms, molecules, or as we will show, QDs, is dipolar coupling. When an excited molecule is placed in the near-field ($\lesssim 100$ Å) of a ground state molecule, the transition dipoles of resonant transitions in the excited molecule and the ground state molecule can couple through their generated electromagnetic fields²⁰⁻²². This coupling can cause the excitation in the excited molecule to be transferred to the ground state molecule, returning the excited molecule to its ground state and promoting the ground state molecule to a higher excited state. This electronic energy transfer process is a well known phenomenon between molecules in organic solids and between impurity centers in inorganic solids²⁰⁻²².

In chapters 3 and 4, we demonstrate and analyze electronic energy transfer arising from dipole-dipole interactions between proximal dots in close packed QD solids^{23,24}. In an optically thin and clear, close packed QD solid prepared from a mixed system of 82% 38.5 Å QDs (small) and 18% 62 Å QDs (large), we show dramatic evidence of electronic energy transfer from the small to the large QDs. We measure quenching of the luminescence quantum yield (lifetime) of the small dots accompanied by enhancement of the luminescence quantum yield (lifetime) of the large dots in the mixed solid. Photoluminescence excitation studies show that photoexcitations generated in the small dots contribute to the luminescence of the large dots. Using Förster's theory for long-range resonance transfer of electronic excitations through dipole-dipole interdot interactions, we obtain independent and consistent measures of the energy transfer efficiency from the spectral overlap of the emission of the small dots with the absorption of the large dots and from the quenching of the luminescence of the small dots in the mixed QD solid. The time dependence for the decrease in the luminescence decay for the small dots and the increase in the luminescence decay for the large dots is reproduced by the long-range resonance transfer model with the same energy transfer efficiency.

We show that in a sample of "single" size QDs, energy transfer within the sample inhomogeneous distribution leads to an observed red shift and narrowing of the emission lineshape in the close packed QD solid from that for the QD solution. In an artificially

broadened QD solid and solution, we see that the increased sample inhomogeneity increases the observed energy transfer effects in the solids. The magnitude of the red shift reflects both the efficiency of energy transfer and the spectral inhomogeneity of the QD sample.

1.4 Electronic Coupling and Photoconductivity

Photoconductivity is another well-known phenomenon in semiconductors and organic solids^{25,26}. It is therefore a natural extension to study the photoconductive properties in new, yet similar materials systems. Photoconductive measurements of QW superlattices reveal large photocurrent gains unique to the superlattice structure²⁷. Electronic coupling between QWs in the superlattice enables the electrons to tunnel between wells. The larger effective mass of the valence band localizes the holes, requiring them to hop between wells. It is the difference in carrier effective masses that leads to the large photocurrent gain. Photoconductivity has long been observed in otherwise insulating organic solids²⁸. The physics of electronic transport in these systems is not well understood. Photoconductive measurements have been used as a route to study the transport of carriers between the weakly interacting molecules in organic solids²⁶.

In chapter 5, we demonstrate photoconductivity in close packed CdSe QD solids. We measure the dependence of the photocurrent on applied voltage, excitation energy, excitation intensity, and temperature to elucidate the mechanisms of charge generation, separation, and transport. We show that the spectral response of the photocurrent follows the absorption spectra for the QD solids, demonstrating carrier generation in the QDs. The I-V characteristics for the QD solids are nonlinear having a threshold voltage to “turn-on.” The photocurrent is linear with incident intensity consistent with an efficiency of charge generation which is simply scaled by the incident photon flux. We also observe an anomalous temperature dependence. The photocurrent increases with increasing temperature for $T < 75$ K above which the photocurrent decreases. This is

consistent with a thermally activated process which is overcome by the exponentially decreasing lifetime of the exciton at higher temperatures. We present three possible models, describing field-assisted charge separation, collective transport of carriers, and carrier tunneling, to explain the photoconductive properties of QD solids.

1.5 Summary

This thesis describes the synthesis, structural characterization, optical spectroscopy, and electronic characterization of close packed solids prepared from CdSe QDs tunable in size from 17 to 150 Å in diameter ($\sigma < 4.5\%$). We show spectroscopically that electronic energy transfer occurs between proximal QDs in the solids and arises from dipole-dipole interdot interactions. We also demonstrate photoconductivity in these QD solids as carriers are generated in the QDs and transported through the QD solids. The physics of interdot interactions is important in understanding the fate of electronic carriers and excitations generated in QD structures.

Chapter 2

Synthesis, Structural Characterization, and Optical Spectroscopy of Close Packed CdSe Quantum Dot Solids *

2.1 Introduction

Nanometer size semiconductor quantum dots develop atomic-like electronic and optical properties as the dot radius is decreased to sizes comparable to the bulk exciton Bohr radius. Spatial confinement of electronic excitations gives rise to discrete electronic transitions that shift to higher energy with decreasing dot diameter². Previous investigations have aimed at understanding the physics of the individual QD and the development of the structural, electronic, and optical properties of materials from molecule to bulk solid. Advances in wet chemical routes produce samples of CdSe QD tunable from 17 to 150 Å in diameter and monodisperse to within the limits of atomic roughness⁵. Each of the QDs consists of an hexagonal crystallite core of CdSe coordinated by a monolayer shell of organic ligands^{5,7}. The high quality of these QD samples has made it possible to observe, assign, and monitor the size evolution of a series of excited electronic states resolved in optical spectra^{8,9}.

Manipulation of these semiconductor QDs into close packed solids presents opportunities to study the cooperative physical phenomena that develop as proximal QDs interact and to engineer the electronic, optical, and structural properties of materials on the nanometer size scale. The organic monolayer coordinating the QD surface enables the QDs to be manipulated as a colloid. In this chapter, we present the synthesis, structural

*Parts of Chapter 2 have appeared in print: C. B. Murray, C. R. Kagan, and M. G. Bawendi, *Science* **270**, 1335 (1995); C. R. Kagan, C. B. Murray, and M. G. Bawendi, *Phys. Rev. B*, in press.

characterization, and optical spectroscopy of close packed QD solids prepared from these CdSe QD samples. Tailoring the composition of the solvents used to disperse the QDs, we control the deposition of glassy and ordered close packed QD solids. High resolution scanning and transmission electron microscopies in combination with small-angle x-ray scattering are used to build a well-defined structural model for the QD solids. We show that the size-dependent optical properties characteristic of the individual QDs are maintained in the QD solids.

2.2 Experimental

2.2.1 Synthesis of CdSe QDs

Samples of CdSe QDs tunable in size from 17 to 150 Å in diameter with <4.5% standard deviation were synthesized according to the method of Murray, *et al*⁵. The preparation involves injecting a mixture of dimethyl cadmium and tri-octyl phosphine selenide into hot tri-octyl phosphine oxide and growing nucleated CdSe seeds to the desired dot size. Post-fabrication processing of the QD samples using size selective precipitation relies on the size dependent stability of the QDs in solvents and nonsolvents to further narrow the sample size distribution. Good solvents, such as alkanes, maintain the stability of the dots in solution. Addition of nonsolvents, such as alcohols, destabilize the QD dispersion causing the largest dots to precipitate from solution first. Once the dispersion becomes unstable, the solution is spun down in a centrifuge to separate the largest dots that precipitated from the smaller dots that remain in solution. The solution of smaller dots is decanted and the largest dots are redispersed in a good solvent. This step is repeated 3 times to obtain samples with distributions <4.5% standard deviation. During the size selection process the QDs are separated from the tri-octyl phosphine [TOP]/tri-octyl phosphine oxide [TOPO] growth medium, soluble in our nonsolvent, leaving each dot with a monolayer of trioctylphosphine chalcogenides coordinating surface Cd atoms.

2.2.2 QD Glasses

Samples of CdSe QDs were manipulated into two- and three-dimensional optically clear, close packed QD glasses ranging in thickness from single monolayers to centimeter thick solids. The glassy QD solids are prepared from size selected QD samples by completely drying the QD dispersions described above under vacuum and redispersing the dots in anhydrous solvents used to deposit the QD solids. Optically thin QD solids $\leq 1 \mu\text{m}$ in thickness are prepared from concentrated dispersions (~20% by weight) of the QDs in mixed alkane of (by volume) 90% hexane and 10% octane. A drop of a dispersion is deposited onto a substrate. The drop spreads radially across the surface and rapidly evaporates to produce an optically transparent, thin ($\leq 1 \mu\text{m}$) colored glass coating. Film optical density and therefore thickness is controlled by varying the concentration of dots in alkane. Repeating the size selection process, described in 2.2.1, 3 times is important in removing excess capping group from the dispersions, otherwise free TOP/TOPO crystallizes out upon formation of the QD solids. All samples were placed under vacuum to ensure there was no remaining solvent entrained. The QDs form uniform, optically clear, close packed QD solids on metal, semiconductor, and oxide surfaces.

Films thicker than $1 \mu\text{m}$ must be dried extremely slowly to avoid cracking. Thick films are prepared by dispersing ~300 mg of a dried QD sample in ~2 mL of nonane. The films are prepared by depositing the concentrated dispersion on a substrate placed in a 10 mL beaker capped with a septum. Monolithic solids are prepared by slow evaporation of concentrated dispersions in capped vials sealed with parafilm.

Single monolayers of the QDs self-assemble onto substrate surfaces upon immersing the substrates in dilute dispersions of the QDs in mixed alkane of 90% hexane and 10% octane. The dispersions appear barely colored to the eye in a ~1 cm path length. The substrate is left immersed in the QD dispersion overnight. Once removed from the dispersion the excess solvent is wicked off and the sample is dried under vacuum.

2.2.2 QD Superlattices

Three-dimensional QD superlattices are prepared by gently adding a mixed solvent of 90% octane and 10% 1-octanol to a size selected CdSe QD sample. Ordered and oriented epitaxial thin films are prepared by depositing the QD dispersion on a substrate surface. The dispersion is dried by placing the substrate in a vacuum oven at 80 °C under ambient pressure and slowly reducing the pressure to ~1 Torr.

Colloidal crystals may be prepared by placing a dispersion of the QDs in a vial capped with a septum, puncturing the septum with a small bore needle, and placing the vial in the vacuum oven. The dispersion turns opalescent upon precipitation of the colloidal crystals. The crystals are then transferred in solution to a substrate and then dried in the vacuum oven to remove any remaining solvent. Alternatively, colloidal crystals may be nucleated by depositing the dispersion on an immiscible liquid subphase of ethylene glycol and heating it in the vacuum oven at ambient pressure. Again the colloidal crystals can be transferred to a substrate and dried in the vacuum oven. Similarly, chemically treated silicon wafers are used to nucleate colloidal crystals directly on the silicon surface. The wafers are treated with 1% hexamethyldisilazane or t-butyl alcohol in anhydrous hexane and rinsed with hexane. The QD dispersion is deposited on the silicon wafer and dried in the vacuum oven.

2.2.3 Structural Characterization

A JEOL JSM 6320FV high resolution scanning electron microscope was used to image the individual QDs close packed into glassy and ordered QD solids. QD solids were prepared from both pure samples of “single” size QDs and mixed samples of small and large QDs. The microscope was operated at 30 kV to detect secondary electron emission from the CdSe QD solids. The QD solids were deposited on silicon wafers and amorphous carbon substrates. The QD solids did not require coating to be imaged without charging effects by the electron beam. A conventional scanning electron microscope was used to image CdSe QD solids at low resolution. A rotatable stage enabled imaging of film fracture surfaces and measurement of

film thickness. A thin gold coat was sputtered on sample surfaces to prevent charging by the electron beam during observation.

A conventional Rigaku 300 Rotoflex powder diffractometer equipped with a Cu anode was used to acquire small-angle x-ray scattering (SAXS) patterns for a size series of CdSe QD samples close packed into solids and dispersed at 1 wt% in poly(vinyl butyral) (PVB). The diffractometer was operated in the Bragg configuration. Samples were deposited on machined (100) silicon wafers.

2.2.4 Optical Spectroscopy

Optically clear, thin solid films were deposited on sapphire optical flats. QD dispersions were loaded in a sample holder between two flats separated by a Viton O-ring. Dye solutions used in quantum yield measurements were loaded in the same manner as the QD dispersions. Samples were mounted in a cryostat for measurements at cryogenic temperatures.

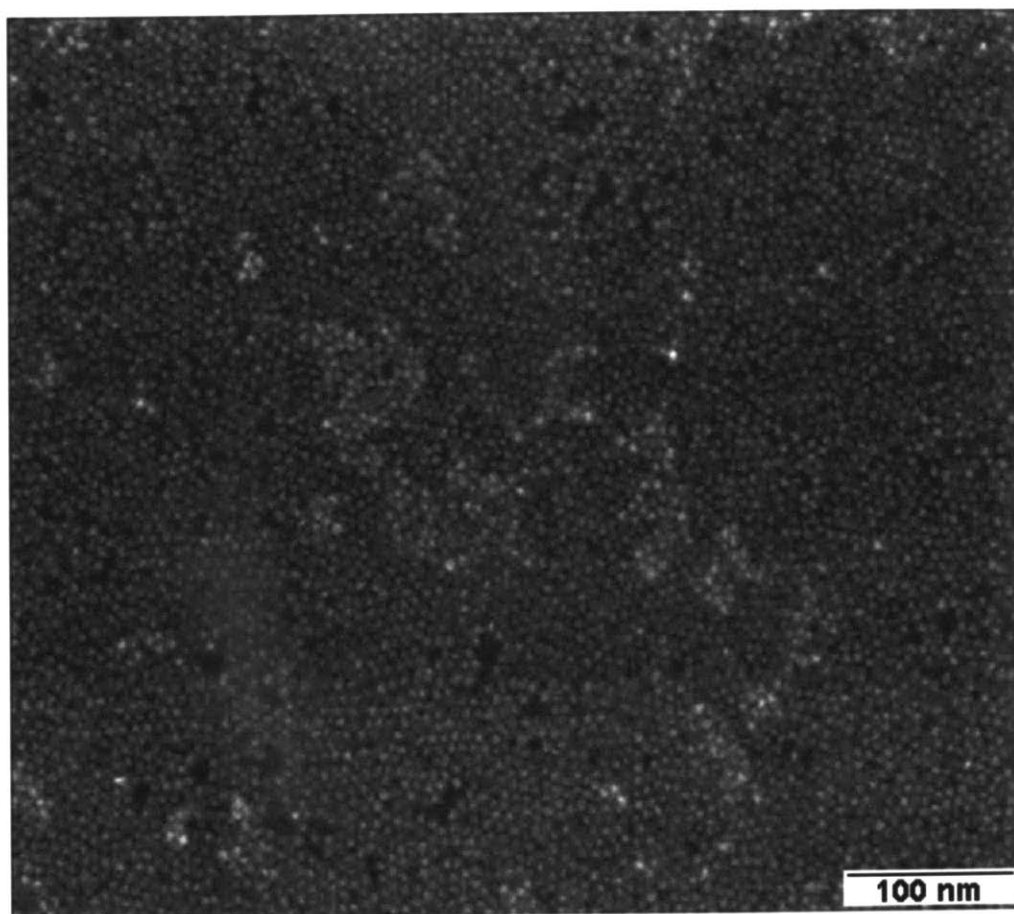
A Hg-Xe arc lamp was used to collect optical absorption spectra. The 457.9 nm line from an argon-ion laser was used as the excitation source for photoluminescence measurements. The transmitted/luminescence light was dispersed through a 0.33 m monochrometer. The spectra were detected by an optical multichannel analyzer. Photoluminescence spectra were also acquired with a SPEX Fluorolog-2.

2.3 Results and Discussion

2.3.1 Two-Dimensional QD Monolayers

Two-dimensional monolayers of CdSe QDs naturally self-assemble from dilute solutions of QDs onto substrate surfaces. Figure 2.1 shows a HRSEM of a monolayer of ~ 7500 62 \AA CdSe QDs self-assembled on a silicon substrate. Locally the QDs form close packed hexagons in which each of the QDs remain separated from the other by the organic capping groups. The monolayer shows only a few holes in the layer and only small patches were a second layer began to form. Dabbousi studied the statistics of local ordering of QDs in

Figure 2.1 HRSEM image of a monolayer of close packed 62 Å CdSe quantum dots. Local ordering of the QDs can be seen by the hexagonal symmetry for each dot and its shell of nearest neighbors.



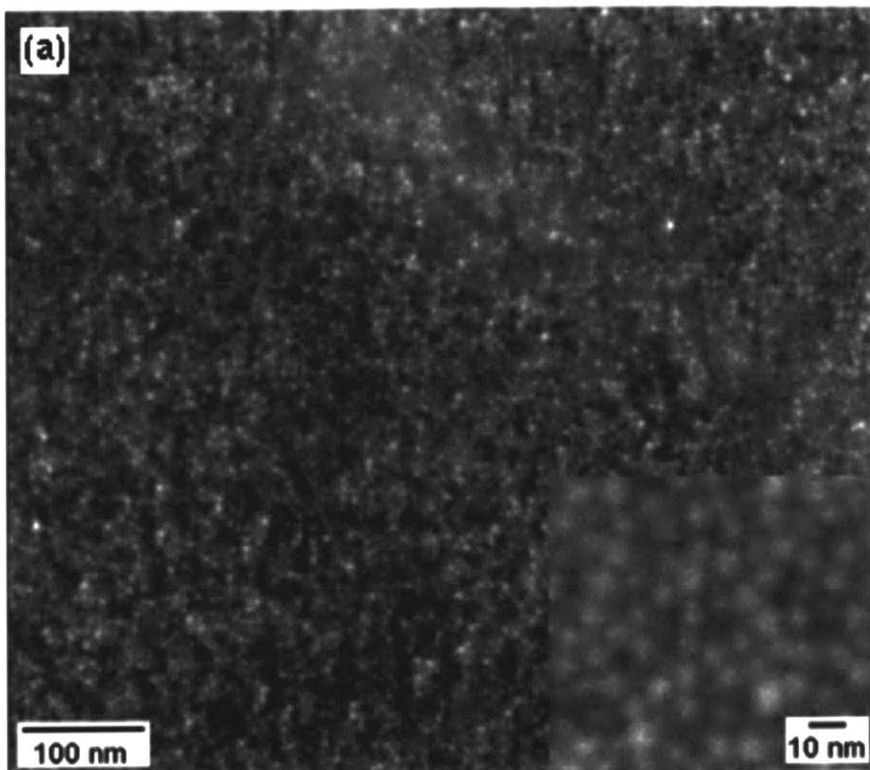
two dimensions from TEM images of QD monolayers prepared by the Langmuir-Blodgett technique²⁹.

2.3.2 Three-Dimensional QD Glasses

The alkyl chains of the TOP/TOPO ligands coordinating the QD surfaces sterically stabilize the dots in alkane, maintaining a repulsive interdot interaction. The stability of the QD dispersions is maintained as it is concentrated by evaporation until it solidifies. This is observed as the QD dispersion remains optically clear as it evaporates until it “freezes,” forming an optically clear solid. The mixed solvent of hexane and octane was chosen to produce optically clear, close packed QD solids with uniform submicron thickness over areas as large as 10 cm². The choice of solvents was critical to the film uniformity. Films ≤ 1 μm thick showed no signs of cracking.

We use the HRSEM to image the individual QDs building up three-dimensional QD solids. Figure 2.2(a) shows a QD solid prepared from 56 Å CdSe QDs. The inset shows the same sample imaged at higher magnification. The micrographs reveal that the QDs are close packed forming a glassy solid in which each dot remains separated from its neighbors by the organic capping groups. While each of the dots possesses nearest neighbors at definite interdot separation and direction, no long range ordering of the QDs is observed. The image also shows that the QD glasses form films of uniform thickness on the nanometer scale over hundreds of nanometers in the lateral direction. We are limited by the field of view with which we can image the solid and still resolve the individual QDs. Profilometry measurements show that films may be deposited that are uniform to <10% over diameters of 1 cm. Correlating film thickness with room temperature optical densities for many QD solids yields an average film optical density of ~ 0.1 measured at the peak of the first exciton for every 1500 Å in thickness. The film optical density will increase with decreasing dot size for the same film thickness. Each QD confines the bulk oscillator strength in the volume of the dot, smaller than bulk exciton Bohr radius. Packing these dots in the solids produces a material with optical densities larger than that of the bulk.

Figure 2.2 (a) Low and high (inset) magnification HRSEM micrographs show 56 Å CdSe QDs close packed in a glassy solid. Each dot remains separated from neighboring dots by the organic cap. (b) SEM micrograph of a ~240 μm thick, glassy QD solid of 38 Å CdSe QDs. To image the fracture surface, the QD solid was tilted 45° with respect to the incident electron beam. The conchoidal appearance of the fracture surface is characteristic of brittle failure in glassy materials.



Deposition of thick films from QDs dispersed in nonane slows the rate of solvent evaporation, reducing the stresses generated by shrinking during drying. Slowing the rate of evaporation produces thick films and monolithic solids without cracks. The thick films took days and the monolithic solids took weeks to months to dry to completion. The monolithic solids could be seen to gel at ~50% by weight and finally shrink isotropically, separating from the vial walls and drying to completion. Figure 2.2(b) shows the fracture surface of a QD glass ~240 μm thick consisting of 38 \AA CdSe QDs. To image the film fracture surface, the QD solid was tilted 45° with respect to the incident electron beam. The conchoidal appearance of the fracture surface is characteristic of brittle failure in glassy materials. This observation is consistent with the non-crystalline nanostructure imaged in the HRSEM. The QD solid has a dense morphology, showing no signs of microscopic porosity. The top surface shows the films have smooth surfaces and remain uniform at these larger thickness. Murray measured the density of glassy QD solids revealing densities >80% space filling, consistent with the random close packing of hard spheres (fill 64% volume) having soft shells that fill the interstices between the dots in the solids³⁰.

SAXS is used to characterize the average local structure of the QDs in the glassy solids. Fig. 2.3(a) shows scattered intensities from a size series of CdSe QD samples dispersed in films of PVB (filled circles). Each of the QDs in a sample acts as an independent scattering center in the polymer matrix and adds to the total scattered intensity. The observed ringings are characteristic of the size and shape of the QDs in the samples. We account for background scattering from the PVB matrix by subtracting the scattered intensity from an undoped PVB film. The scattering pattern, $I(s)$, for an individual, idealized spherical QD of radius R and of uniform electron density is represented by³¹

$$I(s) = f(s)^2 = \left[(\rho - \rho_o) \frac{4}{3} \pi R^3 \right]^2 \left[\frac{9 (\sin(2\pi Rs) - 2\pi s R \cos(2\pi Rs))^2}{(2\pi Rs)^6} \right] \quad (2.1)$$

where $f(s)$ is the Fourier transform of the form factor for a sphere and ρ and ρ_o are the electron densities of the QDs and the polymer matrix. Eq. 2.1 describes the oscillations observed in the SAXS patterns [Fig. 2.3(a)], accounting for the decrease in periodicity with increasing dot diameter and the decrease in scattered intensity with increasing

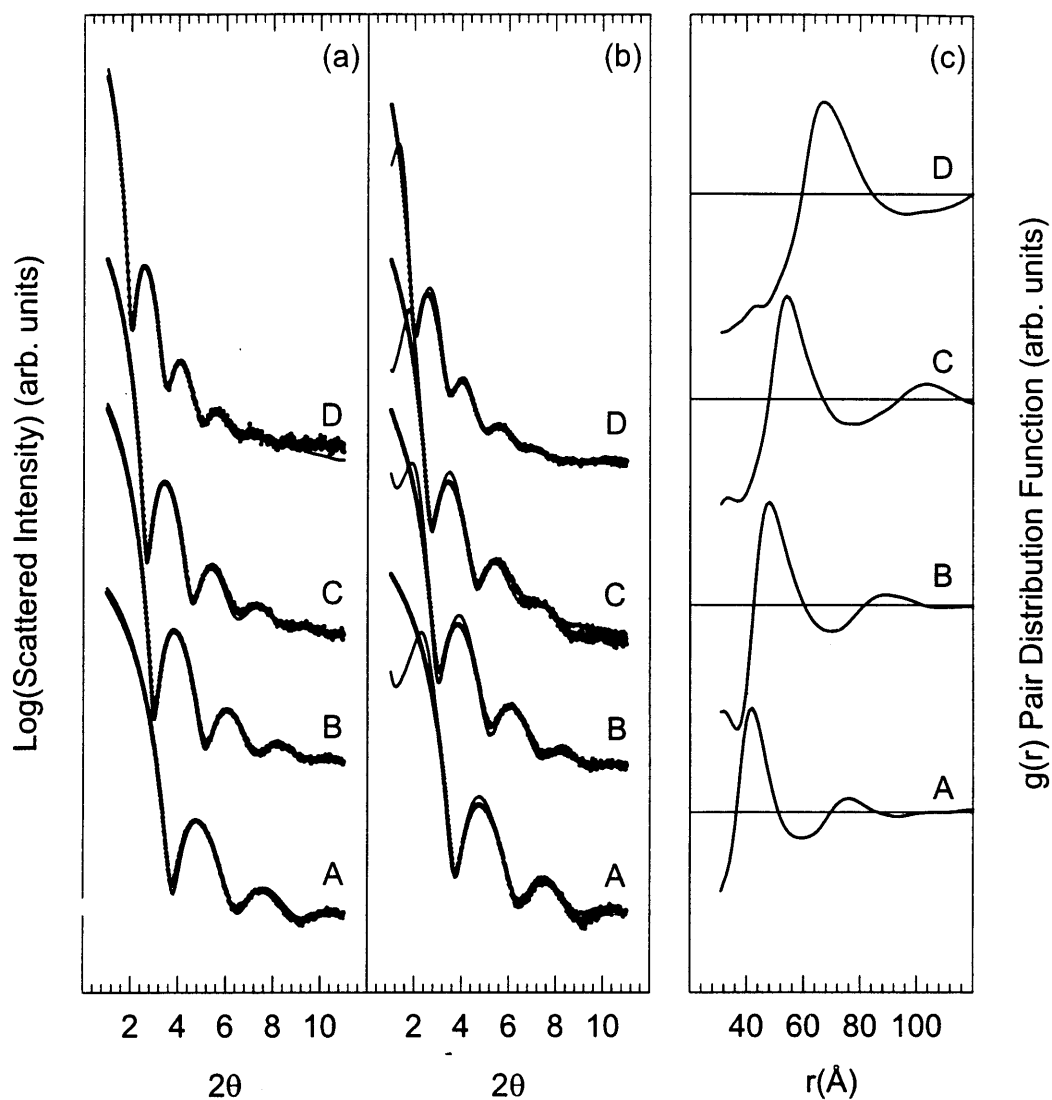


Figure 2.3 (a) SAXS patterns for CdSe QDs dispersed (filled circles) in PVB and fit to form factors for dots (solid lines) (A) $31.6 \pm 4.0\%$, (B) $40.3 \pm 4.0\%$, (C) $45.6 \pm 4.0\%$, and (D) $61.0 \pm 4.2\%$ Å in diameter. (b) Comparison of SAXS patterns for the 4 samples of CdSe QDs dispersed in PVB (filled circles) and close packed in QD solids (solid lines). (c) Pair distribution functions generated for the QD solids.

period. We resolve as many as five oscillations in the scattered intensities. These oscillations, long observed in classic colloidal systems³¹, were unresolved in previous studies of QDs where larger polydispersities broadened the oscillations and prevented their observation. Diffuse scattering of x-rays off the differing electron densities of the Cd and Se atoms in the QDs adds to the baseline in our SAXS patterns. The contribution from diffuse scattering $\propto R^3$ is small compared to $f(s)^2 \propto R^6$ in micrometer size particles but becomes significant on the nanometer scale. TEM observations and the relative intensities of reflections in the wide-angle region of the diffraction patterns reveal that the QDs become prolate with increasing dot size with aspect ratios ranging from 1.0 to 1.25⁵. We simulate the SAXS patterns by simultaneously fitting the small- and wide-angle regions of the diffraction patterns to account for the internal structure of the QD and for its size dependent aspect ratio^{18,30}. We also allow for a Gaussian distribution in dot size for each of our QD samples to weight the total scattered intensity. We fit (solid lines) each of the 4 SAXS patterns (open circles) [Fig. 2.3(a)] to extract average dot diameters for spheres of equivalent volume and sample size distributions. We obtain dot diameters ranging from 31.6 Å to 62.1 Å with standard deviations between 3.5 and 4.5%.

Figure 2.3(b) compares the scattered intensities for the four samples of dots dispersed in PVB (filled circles) with those for dots densely packed in QD solids (solid lines). The differences in the scattered intensities arise from interferences between dots as their positions become correlated in the solids. This is observed mainly as a reduction in the scattered intensity appearing as an additional peak at small angles. The scattered intensity for a QD solid is described by the expression³¹

$$I(s) = Nf(s)^2 \left[1 + \int 4\pi r^2 (\rho(r) - \rho_o) \frac{\sin(sr)}{sr} dr \right], \quad (2.2)$$

where the term in brackets represents the contributions from interferences, $\rho(r)$ describes the dot density as a function of radial distance from a reference dot in the sample, and N is the number of QDs in the solid. Using the experimental form factors $f(s)$ obtained from the scattered intensities of QDs dispersed in PVB [filled circles, Fig. 2.3(b)], we Fourier transform the contributions from interferences to generate pair distribution functions (PDFs)³²

$$g(r) = \frac{\rho(r)}{\rho_0} = 1 + \frac{1}{2\pi^2 r \rho_0} \int_0^\infty s \left(\frac{I(s)}{Nf(s)^2} - 1 \right) \sin(sr) ds \quad (2.3)$$

for the close packed QD solids [Fig. 2.3(c)]. The peak in the PDF represents the center-to-center distance between neighboring dots in the solid. The higher order oscillations are replicas of this same distance. The four QD solids are composed of close packed CdSe dots with an interdot spacing of $11 \pm 1 \text{ \AA}$ maintained by the organic capping groups. The monodispersity of our QD samples enables us to fabricate QD solids with well-defined close packed structures for optical studies.

2.3.3 Three-Dimensional QD Superlattices

Dispersing the QDs in a mixed solvent of 90% octane and 10% octanol results in mild destabilization of the dots as the lower boiling point octane evaporates preferentially over the nonsolvent, octanol. As the mixed solvent evaporates, the steric barrier stabilizing the dots is reduced and the interaction between dots changes from being repulsive to slightly attractive. The slow transition to a slightly attractive interaction causes the QDs to slowly come out of solution, ensuring that the arrival time of the dots from solution is larger than the time it takes for dots on the growing surface to find equilibrium lattice sites. This slow transition is of key importance in the deposition of ordered, 3D QD superlattices. If the arrival rate of the dots becomes larger than the rate of dot diffusion on the surface, an amorphous solid will form.

Deposition of the QD dispersion at an interface produces ordered and oriented epitaxial thin films. The substrate surface presents heterogeneous nucleation sites for nucleation and growth of the QD solids. The HRSEM captures the 3D morphology of QD structures revealing the stages of film deposition as the dots organize, nucleate, and grow into 3D QD superlattices. Figure 2.4(a) shows the initial stages of deposition as $\sim 750 \text{ \AA}$ CdSe QDs assemble on a silicon surface forming an ordered island of QDs. The HRSEM is capable of resolving the individual nanometer size CdSe QDs. Contrast between the substrate and the QDs results from the larger secondary electron emission from the high Z atoms comprising the dots than those of the substrate. The center of the

island shows the second and third layer of QDs adding to the larger surface layer as it begins to grow in three dimensions. Figure 2.4(b) images a larger island of 64 Å QDs deposited on an amorphous carbon substrate. It shows that growth continues perpendicular to the substrate surface as the dots add layer-by-layer forming a more extensive, ordered island of QDs.

As the density of nucleated islands increases, the islands coalesce extending the 3D QD superlattices in the plane of the substrate. Figure 2.5(a) shows what appears to be islands of 64 Å CdSe QDs coalescing to form a more extended, ordered solid of QDs. The number of different layers in each of the islands show that the islands are at different stages in their growth. As the islands grow in 3D, dots also add to the edges of the islands filling in the space between them. Figure 2.5(b) shows islands of 64 Å QDs as the growth of the islands has progressed, further extending the solid in three-dimensions. The necked regions where the islands appear to have grown together show that the dots maintain registry between islands forming an ordered domain with larger coherence length.

The dots continue to add to the growing surface producing ordered epitaxial thin films. Figure 2.6(a) shows an HRSEM image of 64 Å CdSe QDs showing many rows of QDs extending in the plane of the film. The film is many monolayers thick, as evidenced by the remaining hole on top. Following the diagonal line from the edge of the terraces through the extended region on the right shows the formation of an edge dislocation in the QD superlattice. Finally in Figure 2.6(b) again an HRSEM image of 64 Å CdSe QDs shows an ordered epitaxial film extending over 550 nm (field of view) across. Each of the QDs in the solid contain ~8000 atoms and are capped by ~600 TOP/TOPO ligands. The film shows remaining surface roughness as growing layers remain incomplete. These film shows terraces, ledges, and kinks analogous to the Burton, Cabrera, and Frank model for adatoms adding to a growing surface³³.

In the arrival limited regime, dots have enough time to diffuse at the growing surface to form crystalline solids. If the rate of arrival becomes too large, the dots will land on top of each forming an amorphous solid. Figure 2.7 shows the effects of an increase in the flux of atoms adding to the surface. Initially the 62 Å QDs deposited as

Figure 2.4 HRSEM images captures islands of close packed CdSe QDs self-assembling on a surface. (a) An island of $\sim 750 \times 62 \text{ \AA}$ CdSe QDs in the initial stages of deposition. (b) Layer-by-layer growth perpendicular to the substrate surface forming a more extensive island of ordered 64 \AA CdSe QDs.

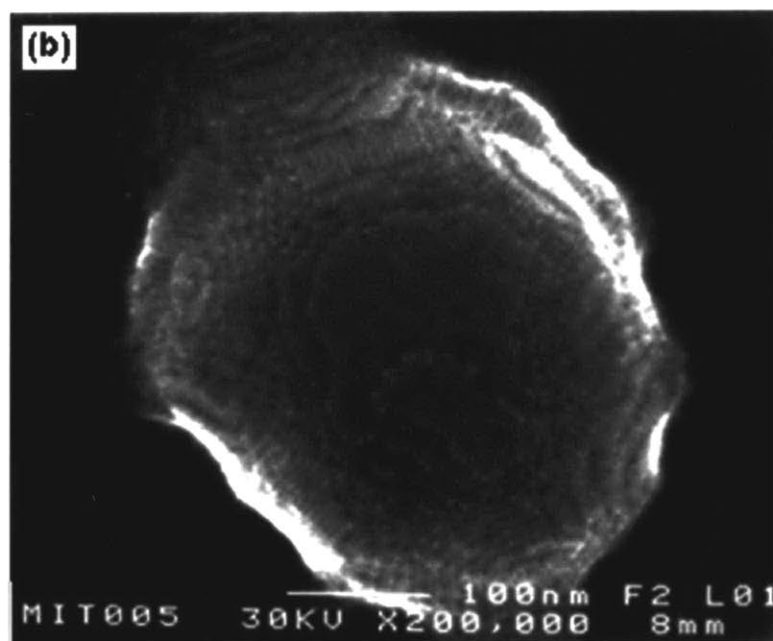
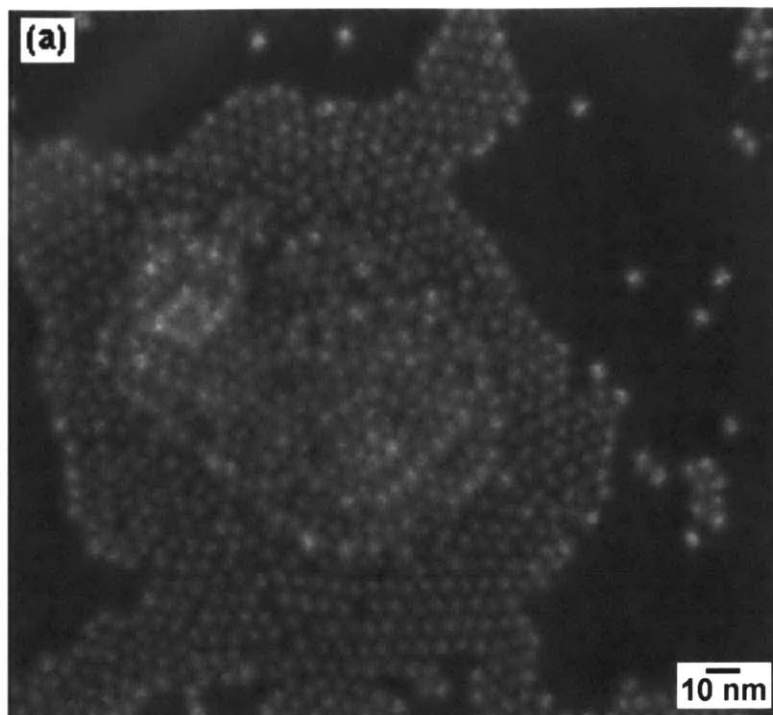


Figure 2.5 Islands of 64 Å CdSe QDs coalescing to form more extended, ordered solids of QDs. (a) The number of layers are indicative of islands at different stages of growth. The dots add both to the growing surface and at the edges of the islands, filling in the valleys between islands. (b) Necked regions show that the dots maintain their registry as the islands coalesce forming a domain with a larger coherence length.

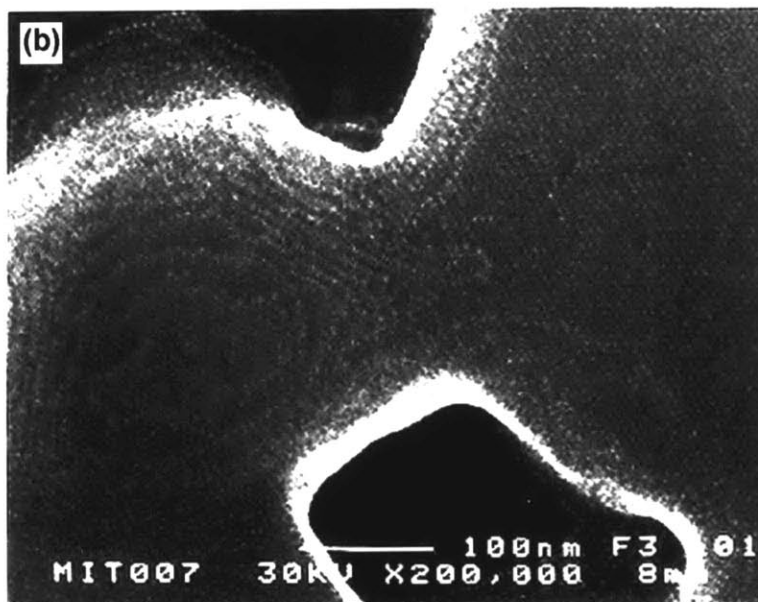
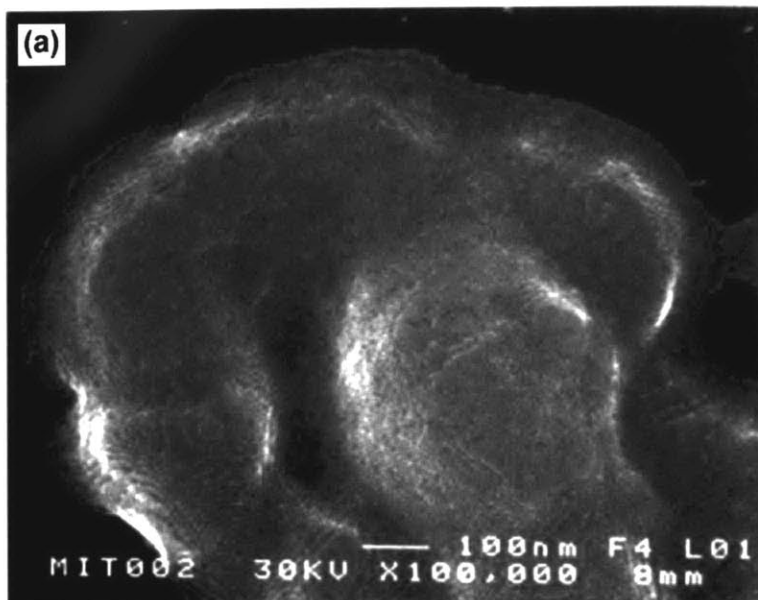


Figure 2.6 HRSEM micrographs show the organization of 64 Å CdSe QDs into 3D QD superlattices. (a) Ordered rows of dots form terraces, ledges, and kinks analogous to adatoms adding to a growing surface. The hole on the top of the micrograph shows that the solid is many monolayers thick. The diagonal line extending from the ledges across the extended planar region is an edge dislocation in the crystal lattice. (b) An ordered epitaxial film of 64 Å QDs with coherence greater than the 550 nm field of view. The film shows remaining surface roughness by the incomplete layers of QDs.

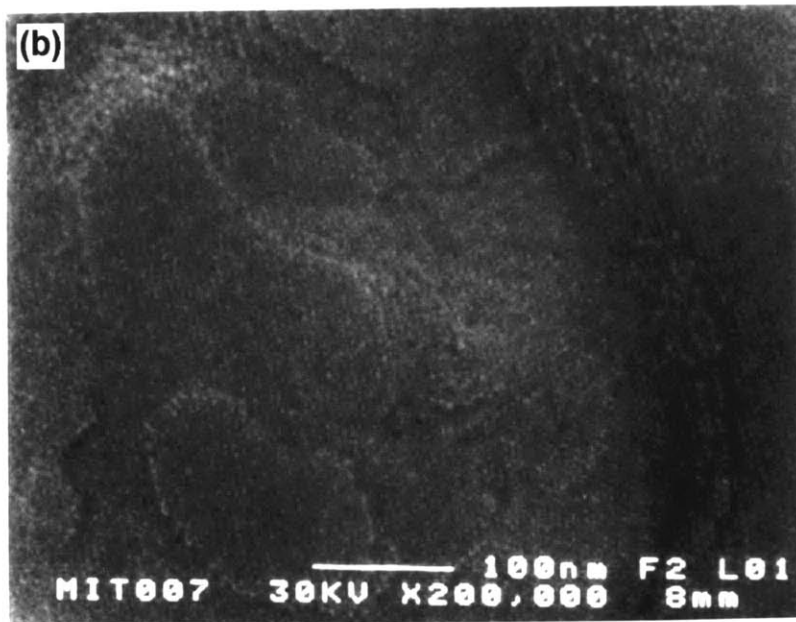
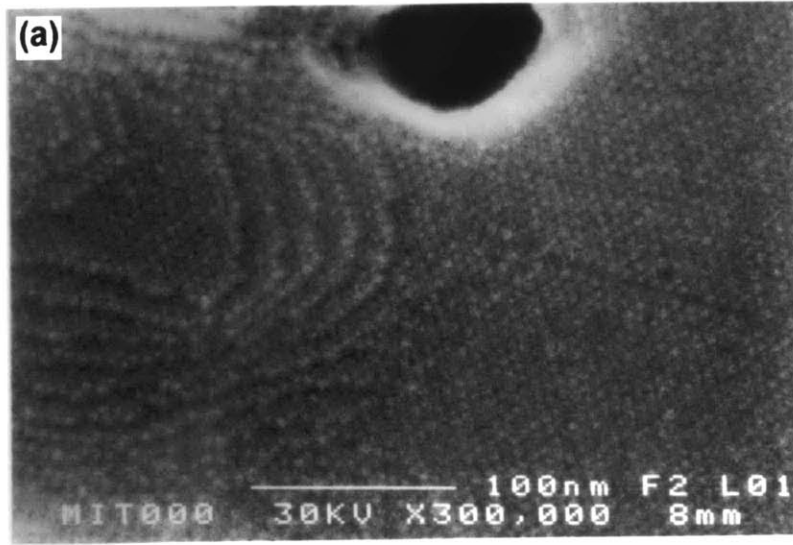
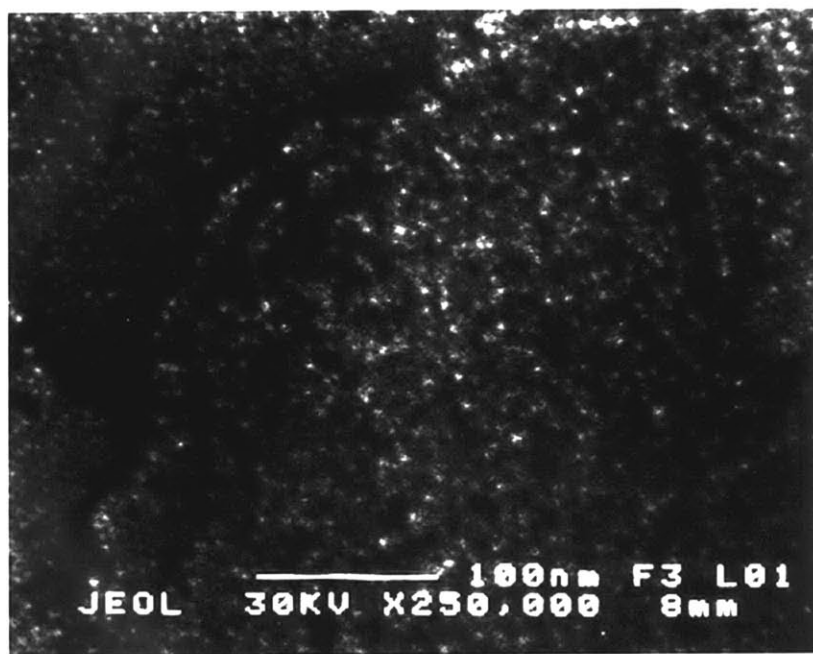


Figure 2.7 HRSEM images the transition from an ordered to glassy QD solid as the rate of deposition increases. The transition is made from arrival limited deposition, where the dots have enough time to find equilibrium lattice sites in the crystal, to diffusion limited deposition, where the dots land on top of one another.



an ordered QD solid. As the flux of dots increased, we see the transition to diffusion limited growth and the formation of an amorphous solid.

We also use the HRSEM to image colloidal crystals formed by homogeneous nucleation in solution. Figure 2.8(a) shows a micrometer size colloidal of 62 Å CdSe QDs. The image was taken at high enough magnification just to resolve the individual QDs making up the crystal. The crystal shows terraces and ledges closing off to form low-index faces. Slower growth rates produce larger colloidal crystals having regular geometries. Figure 2.8(b) shows a $\sim 1.7 \mu\text{m}$ pyramidal shaped colloidal crystal of 48 Å CdSe QDs. The pyramidal morphology is characteristic of a $\langle 111 \rangle_{\text{SL}}$ -oriented face-centered cubic (fcc) crystal structure (SL is used to identify directions and planes of the superlattice). The ledges and terraces seen in Fig. 2.8(a) have closed off to form vicinal $(100)_{\text{SL}}$ facets. The inset shows a square colloidal crystal characteristic of a $\langle 100 \rangle_{\text{SL}}$ -oriented fcc structure. Both structures were coated with Au to prevent charging by the electron beam during observation.

The chemical nature of the substrate surface can be used to control the deposition of epitaxial thin films or colloidal crystals. Above we saw that deposition of a QD dispersion on a silicon surface produced epitaxial thin films. Treating the silicon surface with hexamethyldisilazane (HMDS) or t-butyl alcohol presents a surface similar to the immiscible subphase. Colloidal crystals having regular geometries nucleate homogeneously in solution before precipitating onto the substrate surface. The most common shape of the colloidal crystals formed were incomplete $\langle 111 \rangle_{\text{SL}}$ -oriented pyramids, shown in Figure 2.9(a), similar to those imaged in Figure 2.8(b). Also within a crop of colloidal crystals, $<1\%$ square-pyramids were also seen to nucleate [Fig. 2.9(b)]. Figure 2.9(c) shows the similarity in the size and shape of the colloidal crystals in a crop of crystals deposited on the treated silicon surface. Imaging the individual QDs comprising the colloidal crystals is prohibited by the thickness of the crystals. Crystals of larger thickness do not dissipate charge well enough to prevent charging by the electron beam. Murray observed using high resolution TEM that colloidal crystals having regular geometries are in fact single crystals of QDs³⁰.

Figure 2.8 (a) A micrometer size colloidal crystal of 62 Å dots shows ledges and terraces closing off to form low-index facets. The image is taken at high enough magnification to resolve the individual QDs in the lattice. (b) Colloidal crystal of dots 48 Å in diameter shown the characteristic pyramidal shape of a $\langle 111 \rangle_{\text{SL}}$ -oriented fcc structure. Ledges and terraces have close off forming vicinal $(100)_{\text{SL}}$ facets. The inset shows a $\langle 100 \rangle_{\text{SL}}$ -oriented colloidal crystal from the same sample preparation. Both structures are coated with Au to prevent charging by the electron beam during observation.

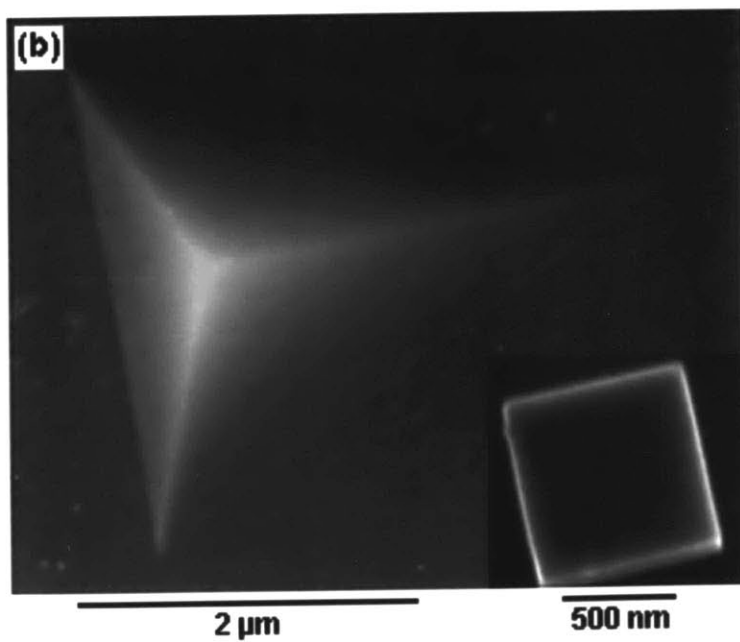
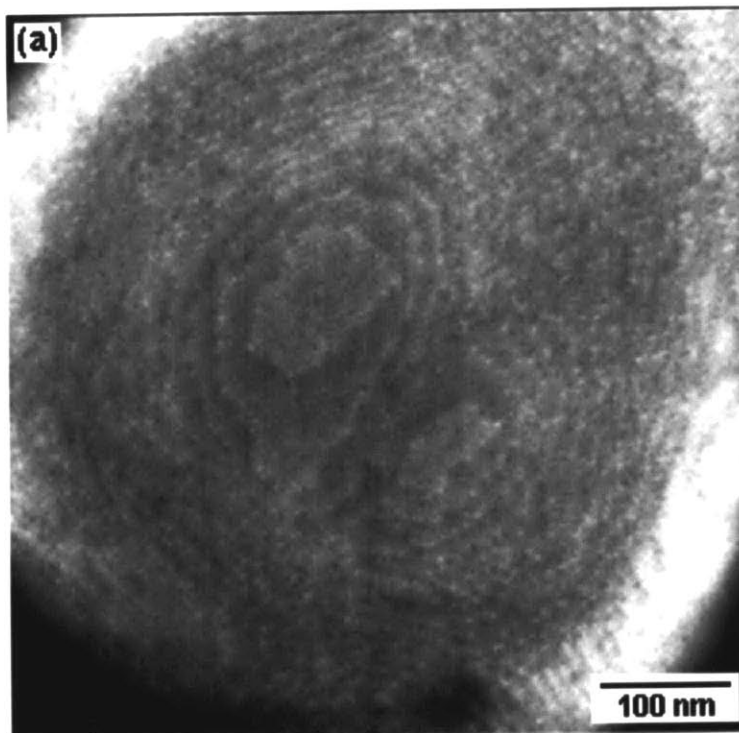
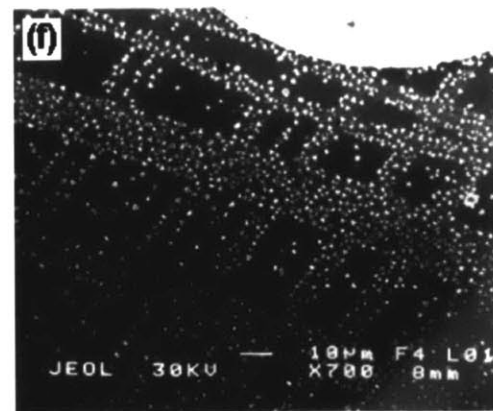
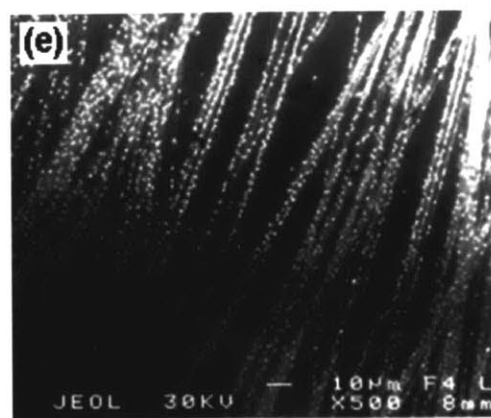
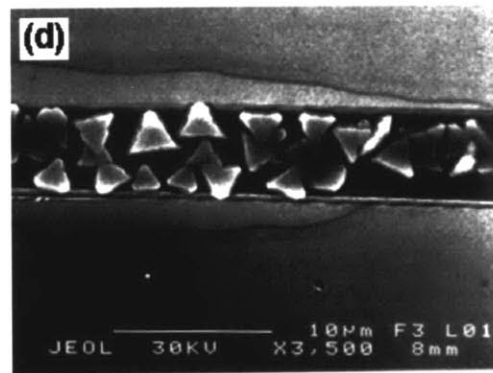
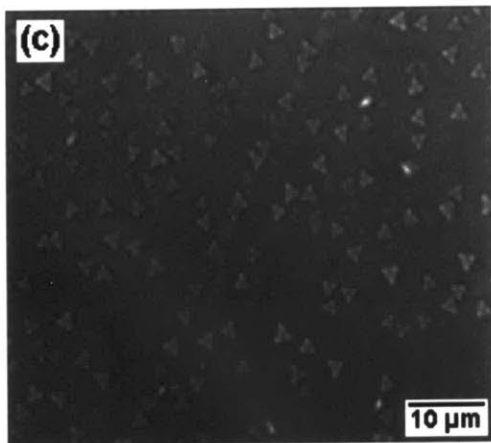
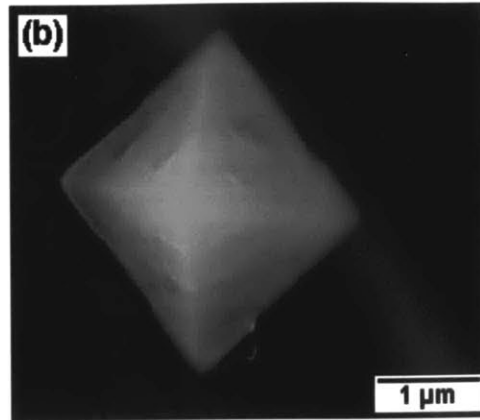
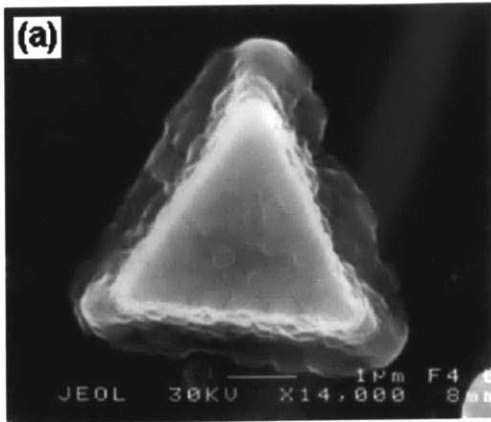


Figure 2.9 Colloidal crystals of dots 57 Å in diameter with shapes of (a) an incomplete pyramid (triangle) and (b) a square pyramid. Chemically and mechanically patterning a silicon surface leads to the spatial organization of colloidal crystals. (c) A crop of colloidal crystals have similar size and shape. (d) Colloidal crystals deposit in the crack in the substrate surface. Colloidal crystals deposit preferentially where gold was left behind by incomplete lift-off on a photolithographically patterned, thermally oxidized silicon surface. The surface was treated with hexamethyldisilazane before depositing the CdSe QDs.

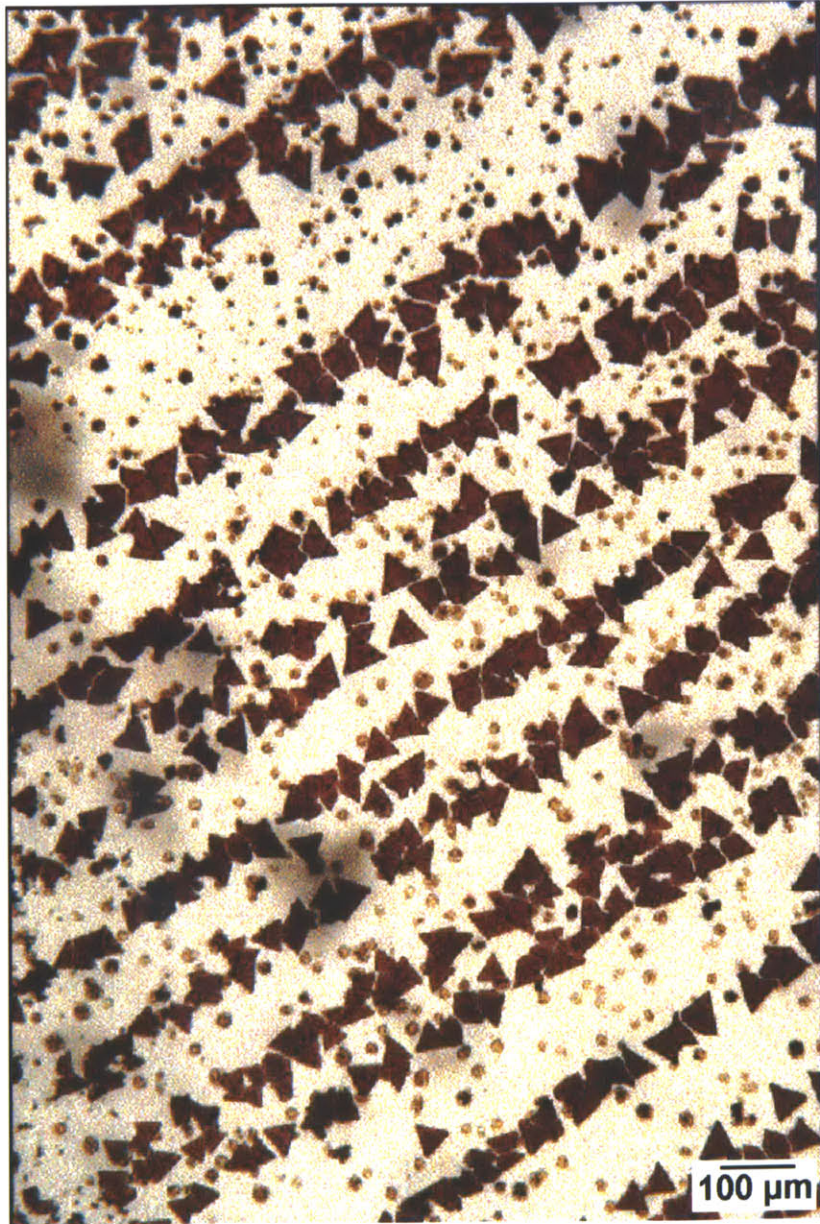


Chemically and mechanically patterning the treated silicon surface leads to the spatial organization of colloidal crystals on the substrate surface. Figure 2.9(d) shows that colloidal crystals self-assemble in a crack in the substrate, leaving the surface around the crack barren. Thermally oxidized, degenerately doped silicon wafers were photolithographically patterned to prepare Au/Cr electrodes. Incomplete lift-off of the Au/Cr where the photoresist was damaged during processing, left regions of the wafer patterned with additional “lines” and “grids” of Au/Cr on the surface. Chemically treating the surface of the substrates with HMDS presented a chemically inhomogeneous surface. Deposition of the QD dispersion still lead to the formation of colloidal crystals, but now the colloidal crystals deposited preferentially on the regions with remaining metal. In the image, the metal regions appear brighter as the yield of secondary electrons is larger from the metal than the substrate. The colloidal crystals formed in lines [Fig. 2.9(e)] and grids [Fig. 2.9(f)] leaving the regions between the metal devoid of colloidal crystals.

Figure 2.10 shows an optical micrograph of 3D colloidal crystals of 57 Å CdSe QDs. Each triangle is ~50 μm on a side. The triangles formed in lines extending radially outward from the center on the bottom of a glass vial. Mechanical stresses created in the walls of the glass vial during pulling may have influenced the deposition of the colloidal crystals. The red color of the triangles is true, arising from the optical spectrum for the 57 Å CdSe QDs.

Murray used TEM and SAXS to establish the fcc crystal lattice for the ordered epitaxial thin films and colloidal crystals^{16,30}. Figure 2.11(top) shows real space imaging, using Z contrast, of four major projections of the fcc crystal lattice of QDs for a 3D superlattice of 48 Å CdSe QDs. Small-angle electron diffraction patterns for each of the projections show sharp spots indicative of lateral perfection of the crystals over the 2 μm spot size. SAXS is used to characterize the average crystal structure over a large area. Figure 2.11(bottom) shows a SAXS patterning for a 3D superlattice of 34 Å CdSe QDs. The reflections in the pattern are indexed by an fcc lattice. TEM observation and SAXS scattering also show that the epitaxial films are both ordered and oriented. The

Figure 2.10 Optical micrograph of 3D colloidal crystals of 57 Å CdSe QDs. The triangles formed in lines extending radially outward from the center on the bottom of a glass vial. The spatial organization may have originated from mechanical differences in the glass as stresses in the walls of the vial are created during pulling. The red color of the triangles arises from the absorption spectrum for 57 Å CdSe QDs. [Photo by Felice Frankel]



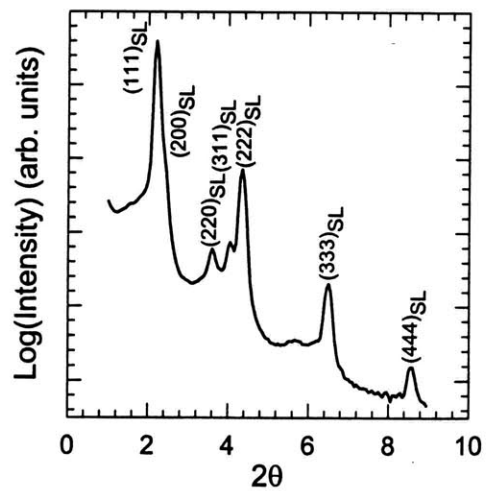
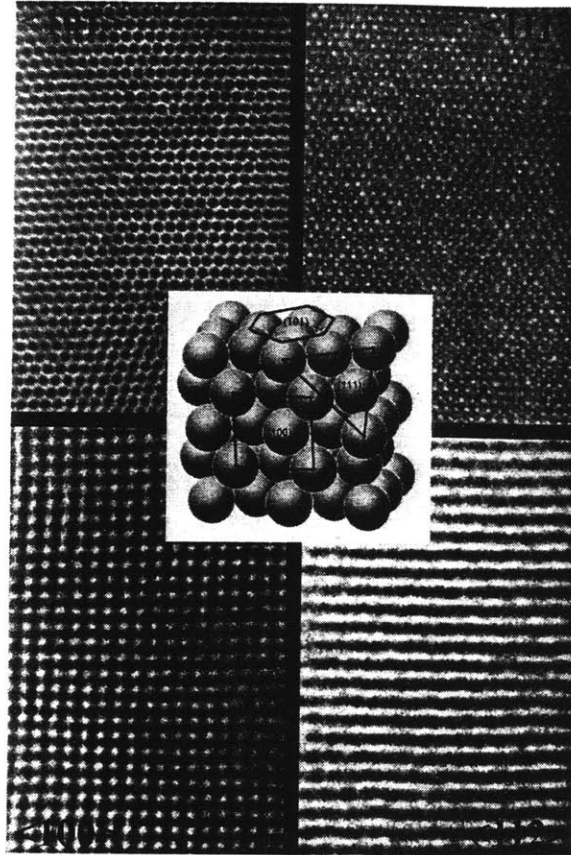


Figure 2.10 (Top) High resolution TEM images showing four projections of the fcc superlattice of 48 Å CdSe QDs. (Bottom) SAXS indexing the fcc QD superlattice of 34 Å CdSe QDs.

relative intensities of the fcc x-ray reflections indicate that the QDs deposit with >80% of their c-axis oriented parallel to the substrate surface.

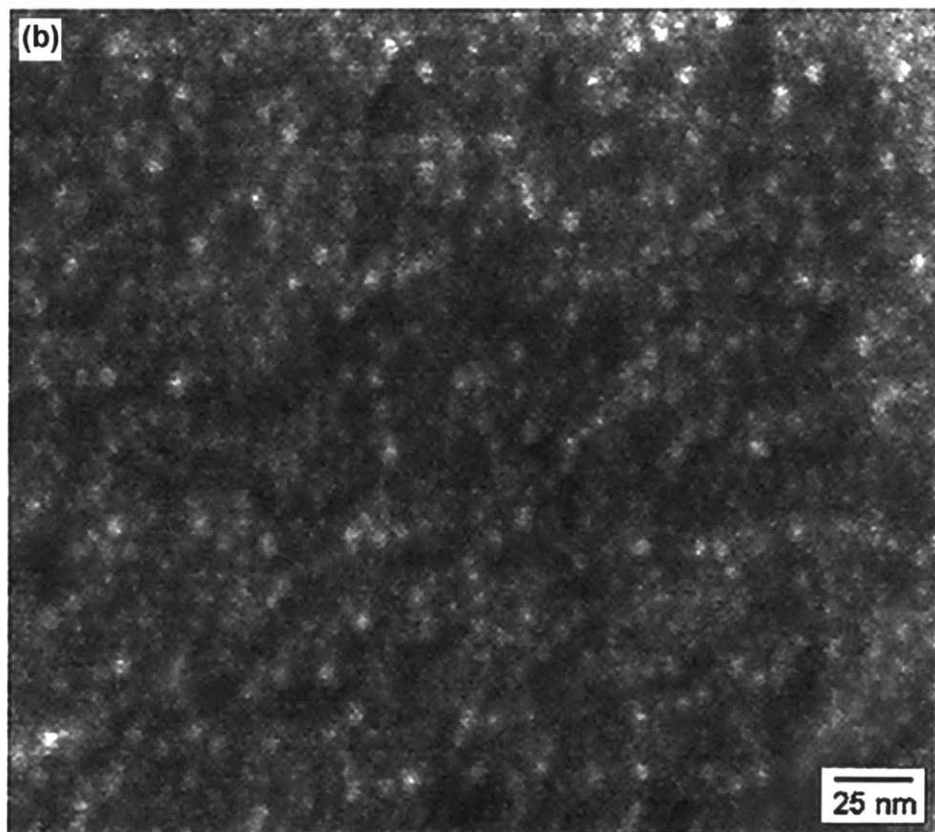
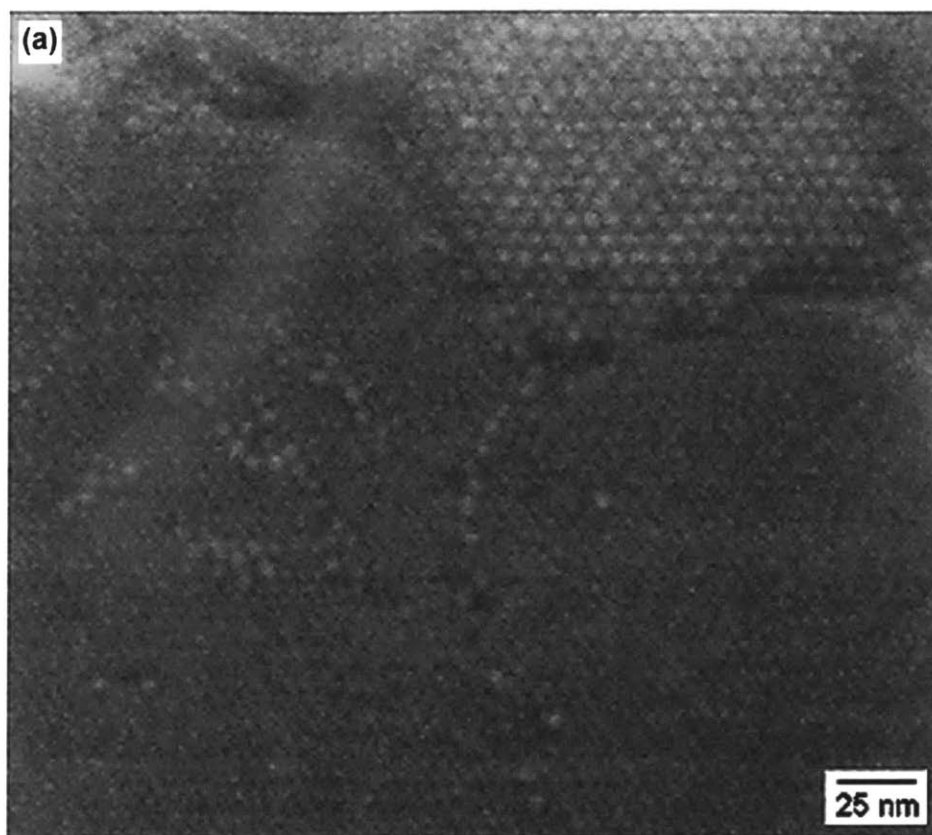
2.3.4 Mixed Glassy and Ordered Solids of Small and Large QDs

In solids prepared from a mixture of small and large dots, the arrangement of the dots in the solids depends on the degree to which the dots order during deposition²⁴. We control the preparation of ordered and glassy QD solids by tailoring the solvents from which the QD samples are deposited. Figure 2.12(a) shows a QD solid prepared from a mixture of 82% 37.5 Å and 18% 57 Å CdSe QDs in 90% octane/10% octanol. The small and large dots have phase separated into ordered regions. The size-dependent stability of the QDs causes the largest dots to precipitate from solution first as the dispersion destabilizes. If the deposition is slow enough, the small and large dots should fractionate completely. Figure 2.12(b) shows that in a glassy QD solid, prepared from 82% 38.5 Å and 18% 62 Å CdSe QDs in 90% hexane/10% octane, the small and large dots remain intermixed. The repulsive interaction between QDs is maintained as the dispersion evaporates until it solidifies. There is no differentiation between the two sizes of QDs as the film is deposited.

2.3.5 Optical Absorption and Emission Spectra for Close Packed CdSe QD Solids

Optical spectra of close packed CdSe QDs show the effects of quantum confinement on the individual dots as well as evidence of interdot interactions. Figure 2.13 shows room temperature (RT) optical absorption and emission spectra of thin solid films of close packed CdSe QDs ranging in size from 30.3 to 62.1 Å in diameter. The discrete and size-dependent optical absorption features and the band edge emission are characteristic of the quantized electronic transitions of individual QDs. The inset shows a comparison of optical spectra for the 30.3 Å dots close packed in the solid with that for the dots dilute in a matrix. It reveals that, although the absorption spectra for the QD solids and solutions are essentially identical, the emission lineshape for the dots in the solid is modified and red shifted, an indication of interdot coupling. Each of the QD solids shows the same red shifted emission spectrum from that for

Figure 2.12 (a) HRSEM micrograph of a mixed CdSe QD solid prepared from 82% 37.5 Å dots and 18% 57 Å dots. The mixture of dots is phase separated into ordered regions of the 37.5 Å dots and the 57 Å dots. (b) HRSEM image of a mixed CdSe QD solid prepared from 82% 38.5 Å and 18% 62 Å dots shows that the dots remain well-intermixed when close packed in a glassy solid. The deposition of ordered and glassy solids are controlled by tailoring the composition of the solvent used to deposit the QD solids.



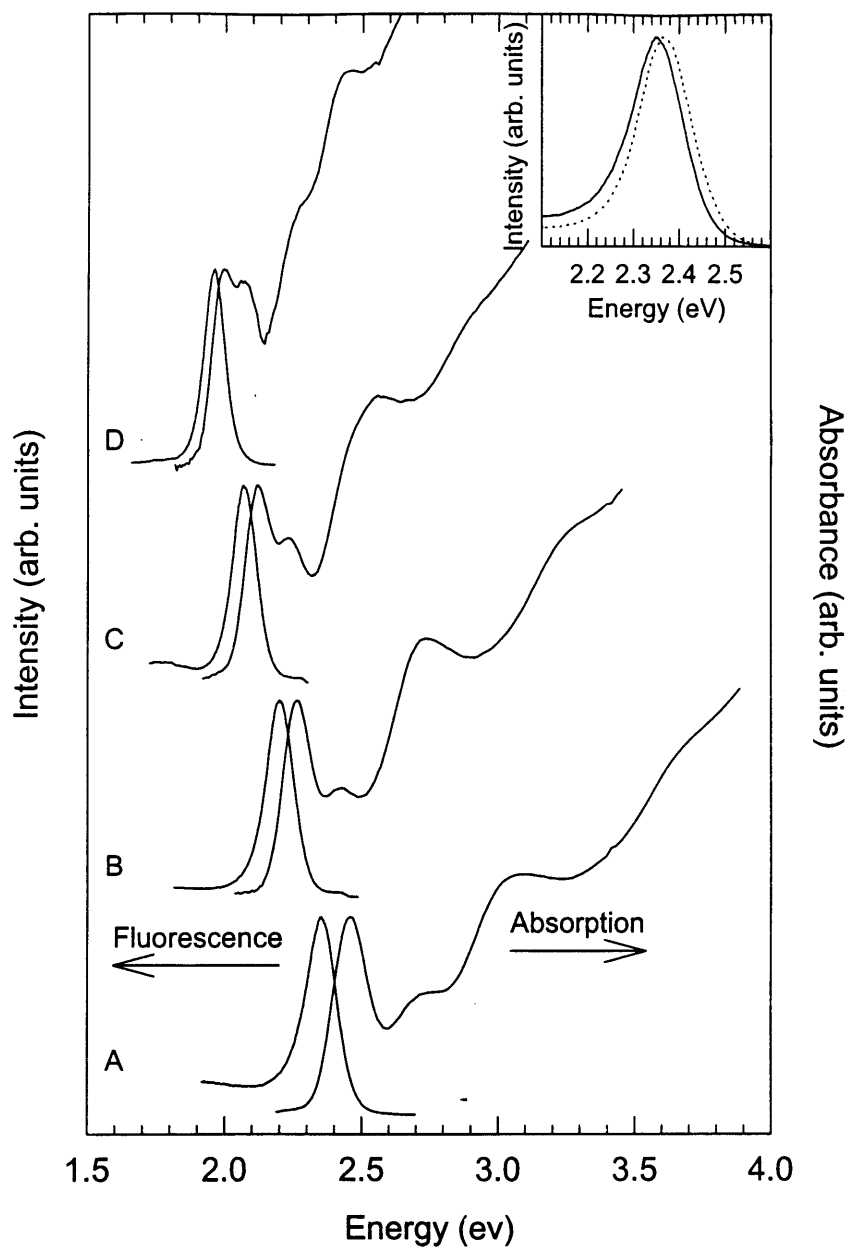


Figure 2.13 Room temperature optical absorption and emission spectra of optically thin and clear, close packed QD solids prepared from samples of CdSe QDs (A) 30.3, (B) 39.4, (C) 48.0, and (D) 62.1 Å in diameter. The inset shows the emission lineshape for the QD solid (solid line) is red shifted from that for the QD dispersion (dotted line) indicative of interdot interactions.

the QDs dilute in a matrix. Chapters 3 and 4 will address the nature of the interdot interactions which lead to the observed differences in the emission spectra for dots close-packed in a solid and dilute in a matrix.

Luminescence quantum yields for the QD solids measured at RT range from 0.001 to 0.01, a factor of ~ 10 lower than measured quantum yields in solution. Reduction in the quantum yield for the QD solids may arise in part from charge separation and transport between dots in the solid decreasing the probability of both the electron and hole residing in the same dot and recombining radiatively. Energy transfer and rapid nonradiative relaxation into lower energy states of non-luminescing dots may also contribute to quenching of the luminescence. Energy transfer and charge transport between QDs in the solid will be addressed in chapters 3 through 5.

The absorption spectra for the QD solids can be used to map the temperature dependence of the effective energy gap for the QDs. The absorption spectra are fit by a sum of Gaussians representing the electronic transitions observed in the spectra. This fitting procedure is repeated for each of the films at temperatures between 10 K and RT to extract the energy of the first exciton. Figure 2.14 plots the positions of the first exciton as a function of temperature. The temperature dependence of the band gap for a bulk semiconductors is described by³⁴

$$E_g(T) = E_g(0) - \frac{\alpha T^2}{(T + \beta)} \quad (2.4)$$

where $E_g(0)$ is the effective energy gap of the QD at 0 K and α and β are constants. β has a value close to the Debye temperature. We fit the temperature dependence for each of the QD solids using Eq. 4. Solid lines show the fits for each of the solids reproduces the measured temperature dependence. The fits yield an average value for $\alpha = 4.8 \times 10^{-4}$ eV / K, consistent with the temperature dependent shift of the bulk bands for CdSe, and $\beta = 194$ K, consistent with the Debye temperature for CdSe³⁵. This may be expected since excitons are known to follow the temperature dependence of the bulk band edges. Eq. 2.4 provides a simple relation to describe the temperature-dependent shift of the absorption spectrum. More rigorous fitting of the temperature dependence for CdS QDs was calculated by Weller using the Radkowsky-Fan relation and parameters for bulk CdS³⁶. He observes a deviation from the bulk behavior for QDs < 16 Å in diameter, smaller than the QDs we studied here.

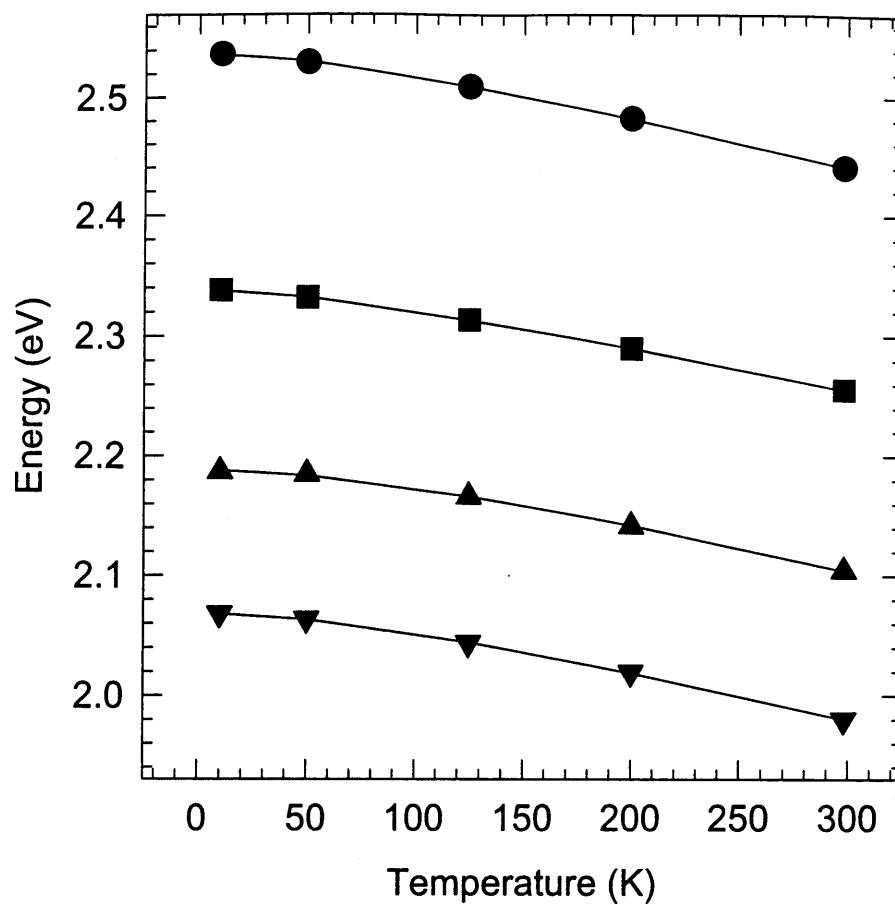


Figure 2.14 Temperature dependence of the position of the first exciton for QD solids prepared from dots (circles) 30.3 Å, (squares) 39.4 Å, (triangles pointed up) 48.0 Å, and (triangles pointed down) 62.1 Å in diameter. The solid lines are the fits to the temperature dependence of the bulk band gap.

2.3.6 Room Temperature Photochemistry of QD Solids

To explore the effects of long time exposure and high intensity photoexcitation on the structural and optical properties of close packed QD solids, a region of film was exposed to the Hg-Xe lamp for 6 hours. The film was mounted in a cryostat and the cryostat was evacuated to reduce the effects of oxygen on the observed photochemistry. PL spectra of the affected region were taken every 1.5 hours and absorption spectra were taken prior to and after illumination. Figure 2.15(a) shows that the absorption spectrum prior to photoexcitation (dashed line) shifts to the blue after illuminating the QD solid for 6 hours (solid line). The absorption spectrum does not change after 15 hours in the dark (dotted line). Using a new film prepared from the same dispersion of 38.5 Å CdSe QDs, the experiment was repeated in the spectrofluorometer. The excitation monochromator was fixed at 2.762 eV (450 nm). PL spectra were collected every 1.5 hours for 4.5 hours of illumination and after 8 hours in the dark. Figure 2.15(b) shows that the emission intensity increases and the peak shifts to the blue with longer exposure times. Our observations are consistent with possible state filling of trap sites, increasing the luminescence intensity, and the simultaneous deterioration of the QDs, leading to blue shifts in the absorption and emission spectra. The effects of photoexcitation can be seen visibly in reflection as a “burn” spot in the film, appearing whiter than the unexposed surrounding regions of the QD solid. This observation is also consistent with trapping of carriers. Increasing the carrier density will change the refractive index of the solid in the region exposed to light, while leaving its absorption properties relatively unaffected.

Small-angle x-ray diffraction patterns of irradiated and untreated films were collected and show no differences in the size of the QDs. The diffraction pattern shows that the volume of the inorganic core remains unchanged. It is possible that illuminating the sample amorphizes the outside of the dots, decreasing the effective volume which confines photoexcitations.

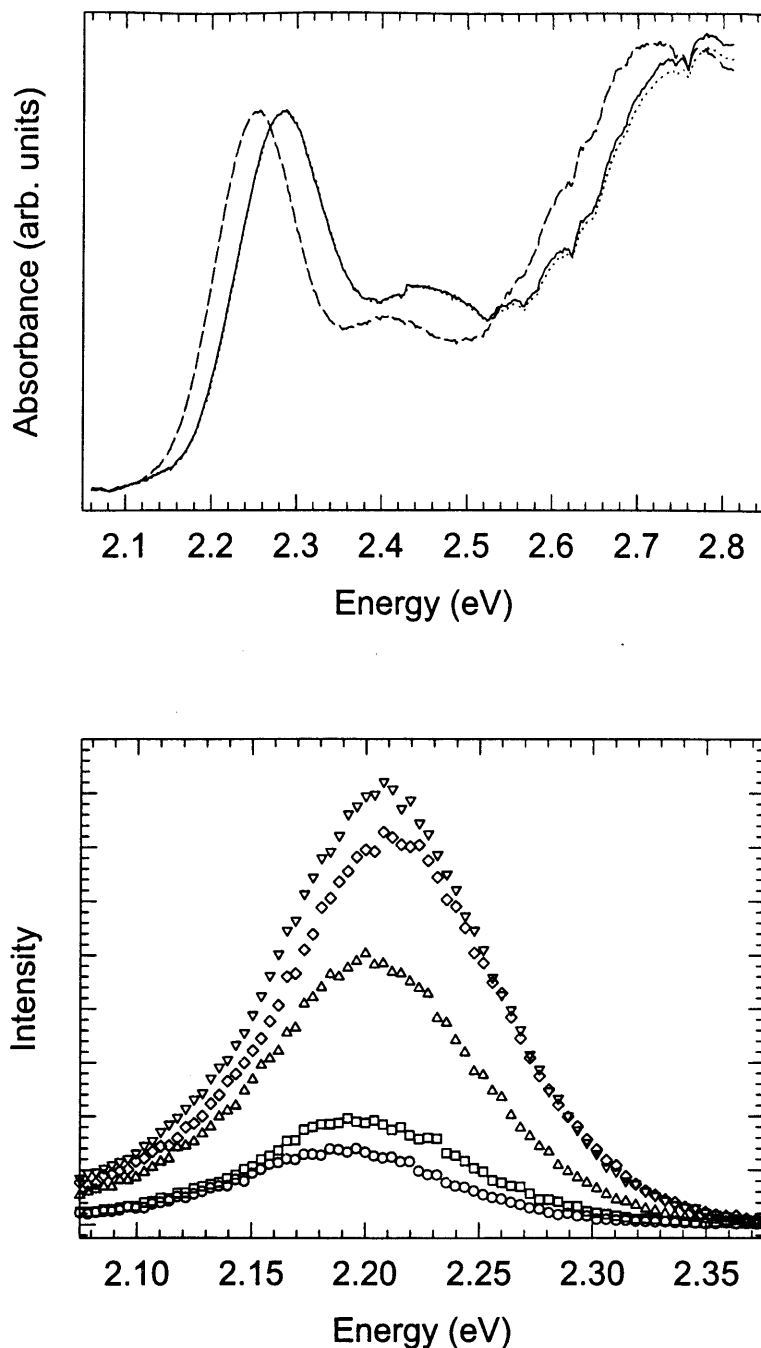


Fig. 2.15 (a) RT absorption spectra prior to (dashed line) and after long term exposure to light (solid line). Dotted line shows there remains no recovery in the absorption spectrum after 15 hours in the dark. (b) RT luminescence spectra for a 38.5 \AA CdSe QD solid prior to (open circles) and after 1.5 (open squares), 3 (open triangles pointed up), and 4.5 hours (open triangles pointed down) of exposure to 2.762 eV (450 nm) light show an increase in the luminescence intensity and a slight shift to the blue. (open diamonds) Luminescence spectra after 15 hours in the dark.

2.4 Conclusion

We present a method to manipulate colloidal, nanometer size semiconductor QDs into close packed QD glasses and crystals. We can control the interaction between dots and therefore the deposition of glassy and ordered QD solids by tailoring the composition of the solvents used to disperse the QDs. HRSEM images the 3D morphology of the QD solids showing the local ordering of the glasses and the long range ordering of both ordered and oriented epitaxial thin films and colloidal crystals. SAXS is used to obtain the average local structure in the QD glasses and the fcc crystal structure of the QD superlattices. The QDs form close packed QD solids in which each dot remains separated from its neighbors by $11 \pm 1 \text{ \AA}$ for the TOP/TOPO capping groups. The combination of electron microscopies and SAXS enables us to establish well-defined structures for both the glassy and ordered QD solids.

Optical spectra for the QD solids show that the size-dependent optical properties of the individual QDs are maintained in the QD solids. While the absorption spectrum remains unchanged, the emission spectrum for the QD solid is red shifted from that for the QD solutions, indicative of interactions between proximal dots in the solid.

Chapter 3

Preliminary Observations of Electronic Energy Transfer in Close Packed CdSe QD Solids*

3.1 Introduction

Close packed quantum dot (QD) solids present opportunities to explore both the collective physical phenomena that develop as proximal QDs interact and the electronic and optical properties of QD solid state materials with potential device applications. Advances in the fabrication of well-defined QD structures by, for example, lithography¹⁴, molecular beam epitaxy¹⁵, and wet chemical methods¹⁶⁻¹⁸ now allow the fundamental interactions in these structures to be uncovered. The QD is the 0D analog of the 2D quantum well (QW), having discrete electronic transitions that shift to higher energy with decreasing dot diameter². Interwell couplings in QW heterostructures continue to be studied for both their fundamental physics and their importance in devices¹⁹. QD solids provide a convenient medium for potential novel optical and electronic devices that exploit both the unique properties of the individual dots and the cooperative effects in the solid. For example, layers of densely packed CdSe QDs incorporated between polymeric electron and hole transport materials electroluminesce with colors characteristic of the QDs³⁷. Semiconductor QDs have generated interest as nonlinear optical materials because their oscillator strengths are concentrated in discrete highly polarizable excitonic states³⁸. Optical nonlinearity should be further enhanced in a QD array as coupling of

* Much of this chapter has appeared in print: C. R. Kagan, C. B. Murray, M. Nirmal, and M. G. Bawendi, *Phys. Rev. Lett.*, **76**, 1517 (1996).

electronic excitations between dots expands the exciton coherence length, enabling it to collect oscillator strength from dots within that larger volume³⁹.

In this chapter we present preliminary observations and analysis of electronic energy transfer in QD solids, arising from dipole-dipole interdot interactions. We spectroscopically probe electronic energy transfer between proximal dots in a close packed solid designed from a mixture of two sizes of CdSe QDs. cw and time resolved photoluminescence (PL) and photoluminescence excitation (PLE) give us independent measures of energy transfer in the mixed QD solid.

3.2 Experimental

Samples of CdSe QDs 38.5 Å (small) and 62 Å (large) in diameter ($\sigma < 4.5\%$) were synthesized according to the method of Murray *et al.*⁵. This synthetic route enabled us to control the dot size and optical properties and to separate the spectral features of the dots in the mixed system. The individual CdSe QDs have been extensively characterized both structurally and optically^{3,5,7-12}. Organic capping groups coordinating the QD surface sterically stabilize the dots in solution. Optically clear (nonscattering), thin solid films were deposited from solutions of small and large dots¹⁸. All measurements were collected for films ~ 0.1 - 0.4 μm thick to minimize reabsorption of emitted photons. The OD of the large dots in the mixed QD solid was < 0.05 at the emission peak of the small dots, making direct reabsorption of the luminescence from the small dots by the large dots negligible.

A conventional Rigaku 300 Rotoflex powder diffractometer equipped with a Cu anode was used to acquire small-angle x-ray scattering (SAXS) data for films deposited on machined silicon wafers. The diffractometer was operated in the Bragg configuration. Small-angle x-ray diffraction patterns were collected for films of close packed QDs and for dispersed QDs in poly(vinyl butyral) [PVB].

The QD solids were deposited onto sapphire flats for optical measurements at cryogenic temperatures. A Teflon spacer was used to separate the QD solids from a second sapphire window positioned to mimic reflection losses in quantum yield measurements relative to

organic dyes. CdSe QD dispersions and dye solutions were loaded into sample holders between two sapphire flats separated by a Teflon spacer. Sample holders were mounted in a helium cryostat for measurements at 10 K and room temperature (RT).

A quartz-tungsten halogen lamp was used to collect optical absorption spectra. A Hg-Xe arc lamp in combination with a monochromator was used as the excitation source for photoluminescence measurements. The transmitted/emitted light was dispersed through a 0.33 m monochromator. The spectra were detected by an Optical Multichannel Analyzer. PL and PLE scans were acquired using a SPEX Fluorolog-2 spectrofluorometer.

3.3 Results

3.3.1 Structural Characterization

Small-angle x-ray scattering (SAXS) was used to characterize the average local structure of the QD solids for the two sizes of QDs in the mixed system¹⁸. We collect SAXS patterns [Fig. 3.1(a,b)] for dots dispersed in poly(vinyl butyral) (PVB) to obtain form factors for the individual dots³¹. We fit each SAXS pattern (solid lines) to determine dot size and sample size distribution using the form factor for a sphere and allowing for a Gaussian distribution in diameter. The ringing of the scattered intensity, previously unresolved, demonstrates the monodispersity of our samples. Our fits yield dot diameters of 38.5 Å [Fig. 3.1(a)] and 62 Å [Fig. 3.1(b)] with standard deviations of 4.5%. Figure 3.1(c,d) compares scattered intensities for the 38.5 Å and 62 Å dots dispersed in PVB (dotted lines) and in densely packed films (solid lines). The diffracted intensities from the QD solids contain interferences arising from local ordering of close packed dots in the glassy solids³¹. We use the experimental form factors for the dots in PVB to extract radial distribution functions for the QD solids [Fig. 3.1(e,f)]³². The first peak defines the nearest neighbor distance and the higher oscillations are replicas of this distance. The QDs are close packed with an ~11 Å spacing from the organic cap. The monodispersity of our QD samples makes it possible to establish a well-defined structural model for the QD solids.

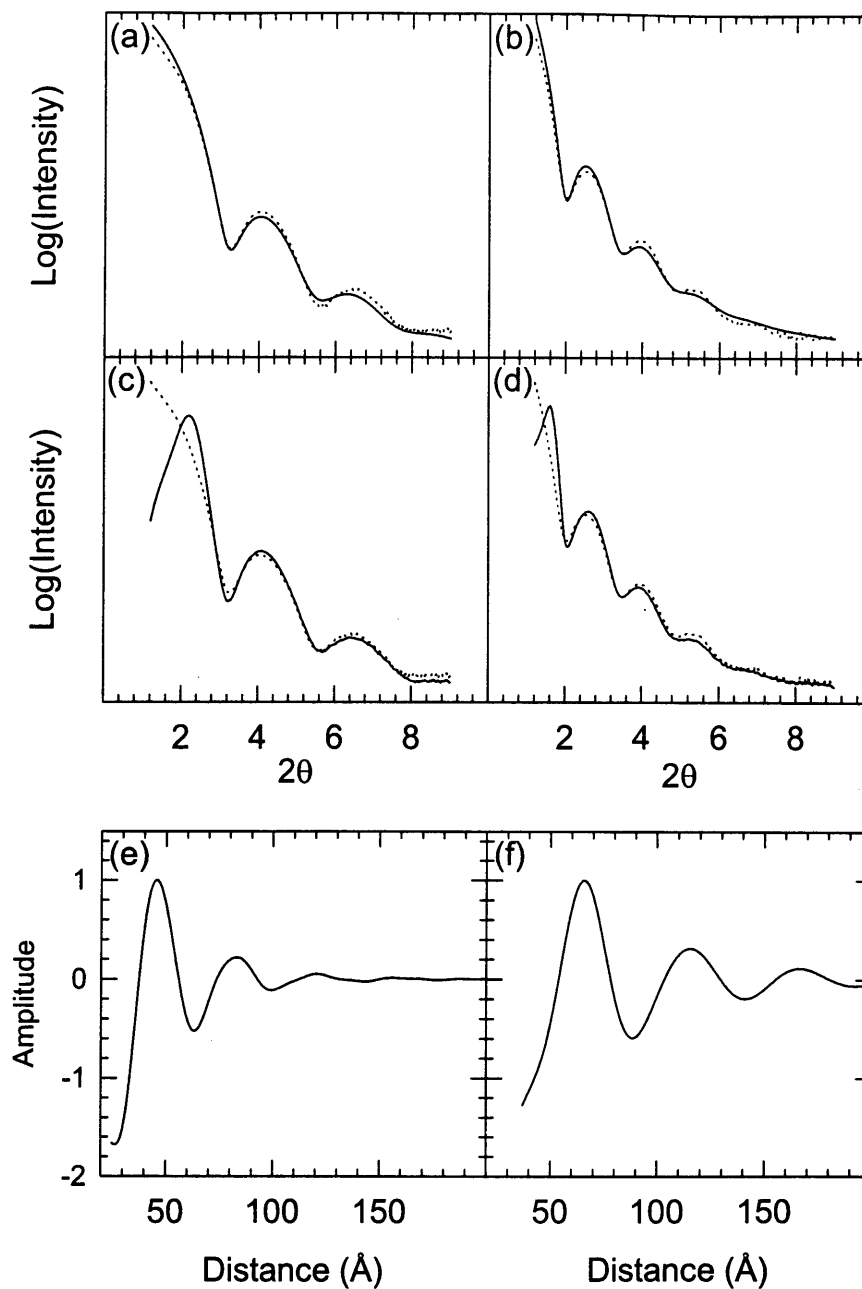


Figure 3.1 SAXS patterns for CdSe QDs dispersed in PVB (dotted lines) fit by form factors for spheres (solid lines) (a) 38.5 Å and (b) 62 Å in diameter each with $\sigma \sim 4.5\%$. Scattered intensities for (c) 38.5 Å and (d) 62 Å dots densely packed in films (solid lines) vs that for dots dispersed in PVB (dotted lines). Radial distribution functions generated for (e) 38.5 Å and (F) 62 Å CdSe QD solids.

3.3.2 Optical Spectroscopy

Figure 3.2(a,b) shows RT and 10 K optical absorption and emission spectra for QD solids prepared from the small and large QDs. The discrete absorption resonances and sharp band-edge emission are characteristic of the size dependent, quantized electronic excitations for these QDs. We study electronic energy transfer between close packed QDs in a mixed system consisting of 18% large dots and 82% small dots.

Optical studies of QDs dispersed in solution probe the photophysics of individual dots. The spectral response of the QD solid is a convolution of the individual properties of the dots and the collective properties of the solid. RT and 10 K PL spectra for the mixed system of dots in solution [Fig. 3.2(c,d)] and in the solid [Fig. 3.2(e,f)] are shown by solid lines. PL measurements reveal an increase in the ratio of large to small dot luminescence quantum yields (QY) in the QD solid versus in solution. Dotted lines in Figure 3.2(e,f) plot the relative QYs for small dots in a pure QD solid and for large dots in the mixed QD solid when excited to the red of the small dot absorption edge*. Excitation to the red of the small dot absorption edge measures the response of the system to photoexcitation of only the large dots. Comparison of QYs reveals quenching of the emission of the small dots accompanied by enhancement of the emission of the large dots in the mixed QD solid when both the small and large dots are excited.

PLE monitoring the fluorescence peak of the large dots resolves the ground state absorptions from which their fluorescence originates. Figure 3.3 shows PLE spectra for a mixed QD solid and solution. Comparison with PLE for a dispersion of pure large dots [Fig. 3.3(c)] confirms that fluorescence from large dots in the mixed solution [Fig. 3.3(b)] arises only from large dot absorptions. Comparison of the PLE for the mixed solid [Fig. 3.3(a)] with the absorption spectrum for the small dots [inset in (a)] reveals that fluorescence from large dots in the mixed solid originates from photoexcitations in both small and large dots.

* The QY for 2.143 eV excitation of 62 Å dots in the mixed film is scaled by the ratio of QYs for 2.762 eV to 2.143 eV excitation of 62 Å dots in solution.

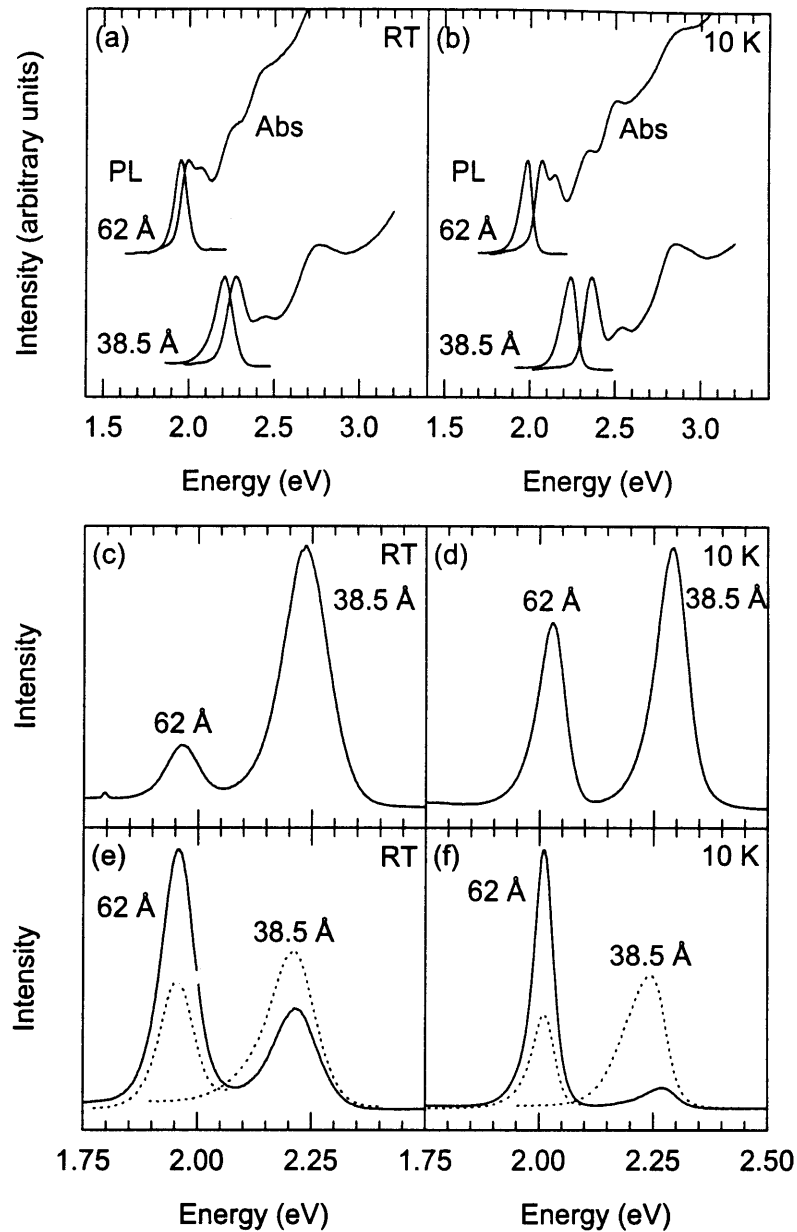


Figure 3.2 Optical absorption and emission spectra for 38.5 Å and 62 Å CdSe QD solids at (a) room temperature (RT) and (b) 10 K. PL spectra for 2.762 eV excitation of the mixed system of 18 62 Å dots in 82% 38.5 Å dots (solid lines) dispersed in solution at (c) RT and (d) 10 K and close packed in the solid at (e) RT and (f) 10 K: Dotted lines plot the relative quantum yields for 38.5 Å dots in a pure film and for 62 Å dots in the mixed film when excited to the red (2.143 eV) of the 38.5 Å dots absorption edge at (e) RT and (f) 10 K.

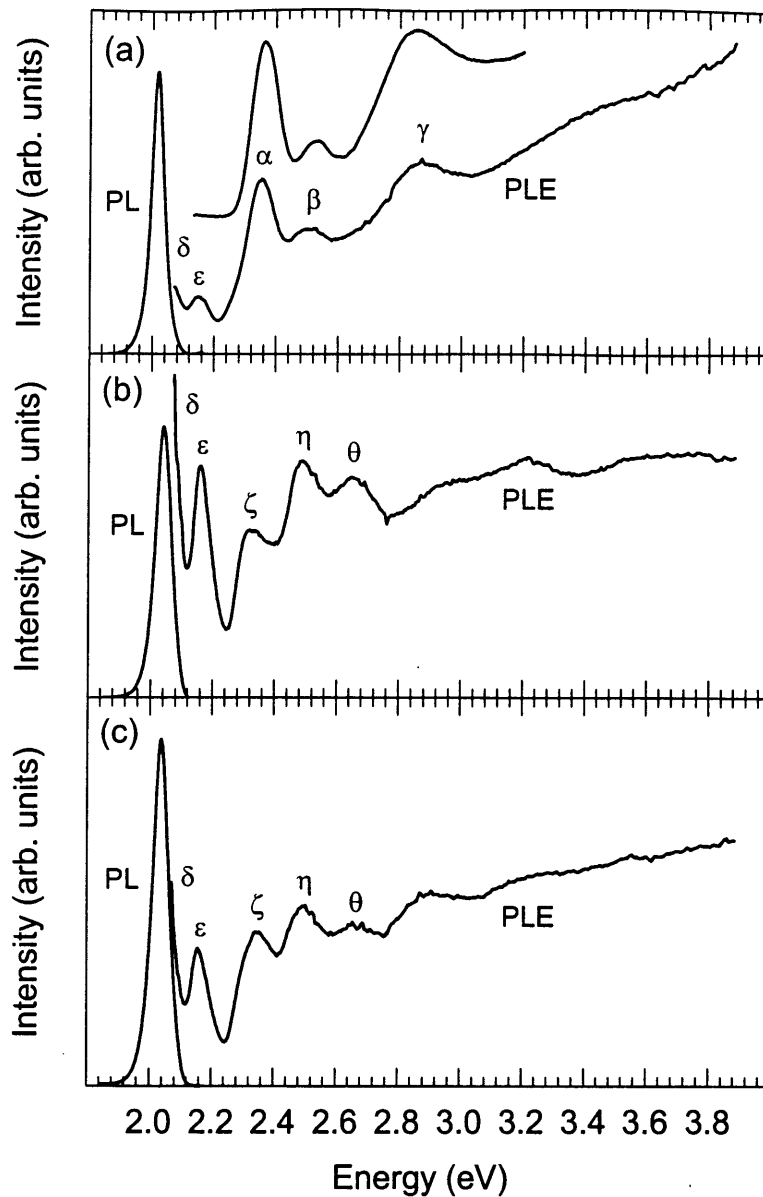


Figure 3.3 PL spectra (10 K) were collected using 2.762 eV excitation. PLE spectra monitoring the peak in the 62 Å dots PL (~1.6 meV bandpass) for the mixed (a) solid and (b) solution. (c) PLE of 62 Å dots in solution. Inset in (a) is the absorption spectrum for a pure 38.5 Å QD solid. The resonances in PLE for the mixed solid are assigned to absorptions of both the 38.5 Å dots, where $\alpha = 1S_{3/2}1S_e$, $\beta = 2S_{3/2}1S_e$, and $\gamma = 1P_{3/2}1P_e/2S_{1/2}1S_e$ transitions, and the 62 Å dots, where $\delta = 1S_{3/2}1S_e$, $\varepsilon = 2S_{3/2}1S_e$, $\zeta = 1P_{3/2}1P_e$, $\eta = 2S_{1/2}1S_e$, and $\theta = 3S_{1/2}1S_e$ transitions⁹.

Time resolved PL was used to measure RT luminescence dynamics for dots in pure and mixed QD solids. Dotted lines in Figure 3.4 show PL decays monitoring the fluorescence peak for small dots in (a) a pure and in (b) the mixed QD solid and for large dots when exciting the mixed QD solid to the (c) blue and (d) red of the small dot absorption edge. The PL lifetime of the small dots is decreased while that of the large dots is increased in the mixed QD solid when both the small and large dots are excited. The observations in Figures 3.2-3.4 are consistent with electronic energy transfer from the small to the large dots.

3.4 Discussion

Measurements of enhanced luminescence have been used to study electronic energy transfer in mixed molecular solids and between dye molecules, chromophores, and phosphors²⁰. Transfer of an excitation requires coupling between the emitting molecule (the donor) and a ground state molecule (the acceptor). At intermolecular separations ≤ 100 Å, long-range resonance transfer (LRRT) of electronic excitation arises from coupling the transition dipoles of the excited donor and a ground state acceptor²⁰⁻²². Enhanced fluorescence requires the acceptor to have both a transition resonant with the donor and a lower energy state in which to trap the excitation²⁰⁻²². In our mixed solid the small dots are the donors and the large dots are the acceptors. We calculate the rate and efficiency of energy transfer from small to large dots in terms of spectroscopic quantities. The time evolution of the PL decays for the small and large dots confirms the LRRT model and the energy transfer characteristics.

Förster theory relates the interaction between transition dipoles of a donor and an acceptor to the spectral overlap of donor emission and acceptor absorption²⁰. We use this theory to calculate the rate (k_{DA}) and critical distance (R_o) for LRRT. R_o defines the distance at which k_{DA} equals the rate of donor de-excitation by competing mechanisms. R_o is then a measure of transfer efficiency where, for randomly oriented dipoles²⁰⁻²²,

$$R_o \propto \left(\frac{\phi_D}{n^4} \int_0^\infty F_D(\tilde{\nu}) \epsilon_A(\tilde{\nu}) \frac{d\tilde{\nu}}{\tilde{\nu}^4} \right)^{1/6}, \quad (3.1)$$

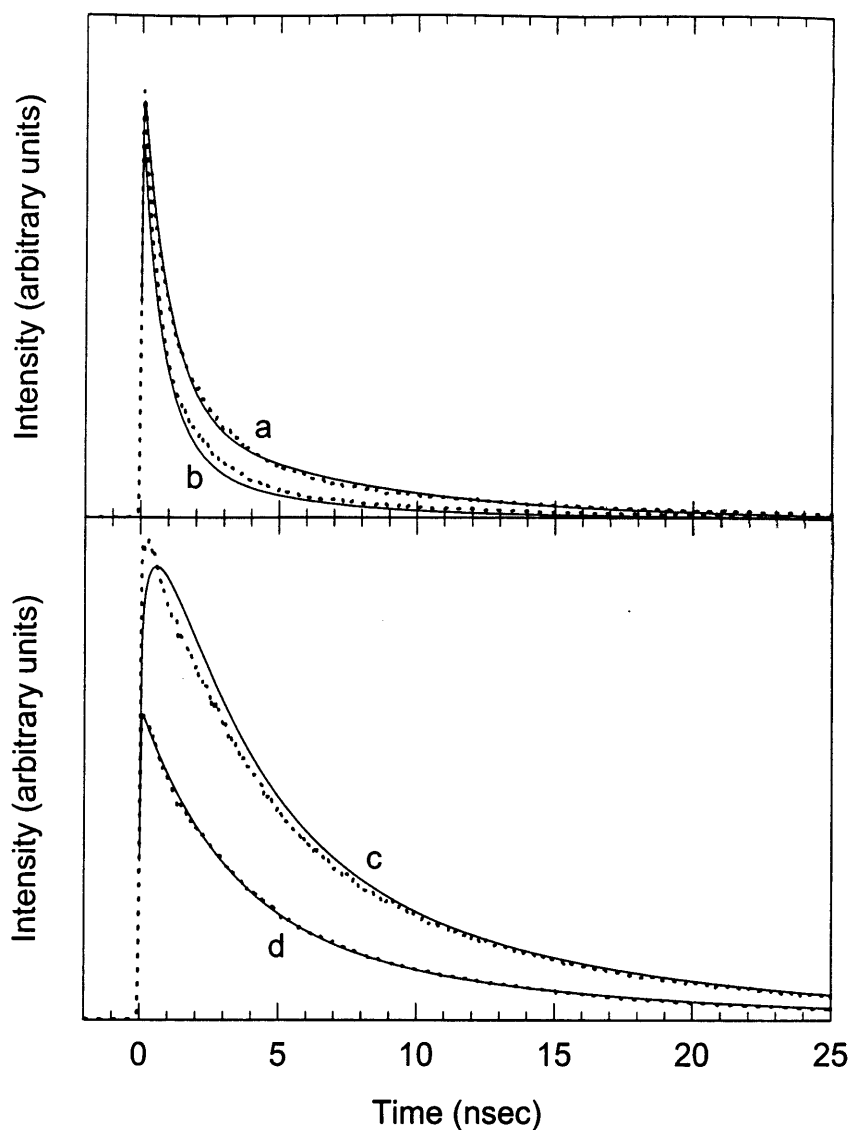


Figure 3.4 PL decays (dotted lines) monitoring the fluorescence peaks for 38.5 Å dots in (a) a pure and in (b) the mixed film and for 62 Å dots in the mixed film when excited to the (c) blue and (d) red of the 38.5 Å dot absorption edge. Decays for the 38.5 Å dots in the pure film (a) and for the 62 Å dots in the mixed film when excited to the red of the 38.5 Å dots absorption edge (d) are fit by biexponentials (solid lines). The decrease in the PL lifetime for the 38.5 Å dots in the mixed film fits Förster's decay law for LRRT [solid line (b)]. The increase in the PL lifetime for the 62 Å dots when exciting the mixed film to the blue of the 38.5 Å dots absorption edge is calculated including LRRT of electronic excitations [solid line (c)]. PL decays were measured using time correlated single photon counting (~ 80 psec resolution) and exciting samples with 2.143 and 2.302 eV pulses. The instrumental response was convoluted in all our fits and calculations.

ϕ_D is the QY of the donor, n is the film refractive index, $F_D(\tilde{\nu})$ is the normalized spectrum for donor emission, and $\epsilon_A(\tilde{\nu})$ is the molar extinction coefficient for acceptor absorption. We assume random orientation of transition dipoles as the transition dipole is defined by the CdSe unit cell² and each dot is randomly oriented in the glassy solid. We take n as the volume weighted average of that for the QDs and the organic cap. Eq. (3.1) yields $R_o=47 \text{ \AA}$ at RT and 67 \AA at 10 K. The temperature dependence of R_o arises from the increase in QY for the small dots with decreasing temperature.

PL decays for the small and large dots [Fig. 3.4] confirm that energy transfer arises from long-range resonant interactions and not from exciton diffusion. LRRT has a rate $\propto t^{-1/2}$ while exciton diffusion has a time independent transfer rate⁴⁰. We fit the nonexponential PL decays (solid lines) for the small (a) and large (d) dots in the absence of energy transfer with biexponentials, representing the distributions of lifetimes. We assume the transfer rate is the same for all the small dots in the mixed solid. The decrease in the PL lifetime for the small dots fits Förster's decay law for LRRT⁴⁰ [solid line (b)]

$$n_{D,MIXED}(t) = n_{D,PURE}(t) \exp \left[-\gamma \left(\frac{\pi t}{\bar{\tau}_D} \right)^{1/2} \right], \quad (3.2)$$

where $\gamma = C \left(\frac{4}{3} \pi R_o^3 \right)$. $n_{D,PURE}(t)$ and $\bar{\tau}_D$ are the biexponential fit (curve a) and the weighted average PL lifetime for the small dots in the pure solid. C is the concentration of large dots in the mixed solid (calculated from their absorbance). The fit yields $R_o=48 \text{ \AA}$, consistent with that obtained above using spectral overlap. Exciting the mixed solid to the blue of the small dot absorption edge increases the PL lifetime of the large dots as excitations are generated both directly by the source and indirectly by resonant transfer from the small dots. The PL decay for the large dots is computed [solid line (c)] combining the decay of photoexcitations, described by the biexponential fit (curve d), with the decay of excitations resonantly transferred from the small dots, described by Förster's decay law (curve b). The excellent agreement between calculated and

experimental curves establishes that LRRT leads to electronic energy transfer from the small to the large dots in the mixed QD solid.

Since we have established the LRRT mechanism from the time dependence, we can also calculate R_o from the quenching of the QY for the small dots in the mixed QD solid relative to that in a pure QD solid [Fig. 3.2 (e,f)]. R_o is expressed in terms of this quenching by integrating Eq. (2) and $n_{D,PURE}(t)$ over time, assuming a weighted average lifetime for the dots, yielding⁴⁰

$$\frac{\phi_{D,MIXED}}{\phi_{D,PURE}} = 1 - \frac{\pi}{2} \gamma \exp\left(\frac{\pi\gamma^2}{4}\right) \operatorname{erfc}\left(\frac{\pi^{1/2}\gamma}{2}\right) \quad (3.3).$$

We obtain $R_o=47 \text{ \AA}$ at RT and 81 \AA at 10 K.

In summary, the spectral overlap of donor emission and acceptor absorption and the quenching of the donor luminescence independently give us $R_o=47$ at RT and $R_o=67$ and 81 \AA , respectively at 10 K. RT quenching of the donor PL lifetime confirms the time dependence for LRRT with $R_o=48 \text{ \AA}$. Comparison of R_o with the distance between donor and acceptor centers ($R_{DA}=61.25 \text{ \AA}$) suggests that coupling between QDs is a nearest

neighbor interaction. The rate of electronic energy transfer is $k_{DA} = \frac{1}{\tau_D} \left(\frac{R_o}{R_{DA}}\right)^6$ where

τ_D is the lifetime of the small dots in the pure QD solid*. We obtain $k_{DA} = 1 \times 10^8 \text{ sec}^{-1}$ at RT and $k_{DA} = 0.6 \times 10^8 \text{ sec}^{-1}$ at 10 K, consistent with characteristic values for LRRT**,¹⁹.

Förster's relationship between dipolar coupling and spectroscopic quantities is valid for donors and acceptors separated by $\geq 20 \text{ \AA}$ ²². Coupling between CdSe QDs is

* τ_D at 10 K is computed using the relative QYs of the donors at RT and 10 K, $\tau_D = \phi_D \tau_r$ assuming τ_r , the radiative lifetime for the dots is temperature independent. This is only true if the same state is the emitting state at both temperatures.

** The temperature dependence of k_{DA} arises from a factor of 2 decrease in the donor/acceptor spectral overlap between RT and 10 K.

expressed as the sum of dipole-dipole interactions between unit cells in donor and acceptor dots. Since the separation between dot surfaces is $\sim 11 \text{ \AA}$, interaction between unit cell transition moments near neighboring dot surfaces may have contributions from higher multipoles. The $\frac{1}{(R^{n+m+1})^2}$ spatial dependence of the energy transfer rate, where

n and m are the orders of the interacting poles, suggests however that higher multipoles are important for only a small number of unit cells near neighboring dot surfaces. Contributions from higher multipoles should be further decreased since interactions are weighted by the spatial overlap of electron and hole wavefunctions which are maximized at the dot centers.

3.5 Conclusion

This chapter presents spectroscopic measurements of electronic energy transfer in QD solids arising from dipolar coupling between proximal QDs. We measured quenching of the luminescence/lifetime of small dots accompanied by enhancement of the luminescence/lifetime of large dots in a mixed CdSe QD solid. Our observations are consistent with long-range resonance transfer of electronic excitations from the small to the large dots. The spectral overlap of donor emission and acceptor absorption, the quenching of the donor luminescence, and the decrease in the donor luminescence lifetime give us three independent and consistent measures of the energy transfer efficiency. The $t^{-\frac{1}{2}}$ energy transfer rate reproduces the time evolution of the small and large dot luminescence decays confirming that LRRT leads to electronic energy transfer between close packed dots.

Chapter 4

Long-Range Resonance Transfer of Electronic Excitations in Close Packed CdSe Quantum Dot Solids*

4.1 Introduction

Nanometer size semiconductor crystallites or quantum dots (QDs), small compared to the bulk exciton Bohr radius, exhibit size dependent electronic and optical properties as electronic excitations are spatially confined to within the volume of the dot. Quantum confinement effects induce quantization of the bulk band structure, concentrating the bulk oscillator strength in discrete electronic transitions that shift to higher energy with decreasing dot diameter². Synthesis of CdSe QD samples monodisperse to within atomic roughness⁵ has made it possible to observe, assign, and monitor the size evolution of a series of excited electronic states^{8,9}. These samples show strong band edge emission with quantum yields (QYs) ranging from 0.1 to 0.9 at 10 K. The size dependent optical absorption and emission spectra of “single” CdSe QDs have been deduced using transient differential absorption⁸, photoluminescence excitation⁹, and fluorescence line narrowing^{10,11} spectroscopies. Agreement between experimental observations and theoretical calculations provides a framework for understanding the size dependent electronic structure of individual CdSe QDs⁶⁻¹¹.

Building close packed solids from semiconductor QDs presents opportunities to investigate both the cooperative physical phenomena that develop as proximal QDs interact and the electronic and optical properties of QD solid state materials. QD solids provide media for potential novel electronic, optical, and optoelectronic applications that

* Much of this chapter will appear in print: C. R. Kagan, C. B. Murray, and M. G. Bawendi, Phys. Rev. B. (in press).

combine the unique properties of individual QDs and the collective properties of coupled QDs. For example, dipole-dipole interdot interactions in close packed QD solids are expected to further enhance the already increased optical nonlinearity of the individual QD³⁸ as electronic excitations collect oscillator strength from multiple dots in the solid³⁹. Dipolar coupling between proximal dots in close packed solids also provides a structure of wireless interconnects mimicking the requirements for complex computations in cellular automata^{14,41}. Coupled QD structures are the basis for designs of high optical gain, low threshold current QD lasers and resonant tunneling QD devices⁴². Recently electroluminescence from densely packed layers of CdSe QDs combined with semiconducting polymers has been demonstrated³⁷. Porous films prepared from nanocrystalline semiconductors have been used to transport charge in photoelectrochemical cells⁴³. Optical and electronic characterization of QD solid state materials is important in understanding the physics of interdot couplings and their role in determining the fate of electronic carriers and excitations generated in QD structures. Tailoring the size of and spacing between the QDs in solids presents opportunities to engineer on the nanometer scale the electronic, optical, and structural properties of these materials.

Recent advances in the fabrication of structurally well-defined two- and three-dimensional close packed QD structures by photolithography¹⁴, molecular beam epitaxy¹⁵, and wet chemical methods¹⁶⁻¹⁸ makes the investigation of interdot couplings possible. Two-dimensional arrays of photolithographically patterned AlGaAs-GaAs QDs show additional absorption resonances in the infrared as neighboring dots become coupled¹⁴. Three-dimensional, close packed CdSe and CdS QD solids have luminescence spectra shifted to the red of spectra for dispersed QDs, indicative of interdot interactions in the solid state^{16-18,24}. In Chapter 3 we studied spectroscopically a close packed QD solids designed from a mixture of small and large CdSe QDs²³. The small and large dots have well-separated spectral features which allowed us to identify changes in their optical spectra. We measured quenching of the luminescence (lifetime) of the small dots accompanied by enhancement of the luminescence (lifetime) of the large dots. Photoluminescence excitation studies revealed that photoexcitations generated in both the

small and large dots contribute to the luminescence of the large dots. We presented preliminary analysis showing that our observations are consistent with long-range resonance transfer of electronic excitations from the small to the large dots in the mixed QD solid. In Chapter 4 we present a more detailed analysis of our observations in the mixed QD solid to further demonstrate that dipolar coupling between proximal dots in close packed QD solids leads to electronic energy transfer. We show spectroscopically that in single size QD samples electronic energy transfer within the sample inhomogeneous distribution accounts for the red shift in the emission for the QD solid relative to that for the QDs dispersed in solution.

4.2 Experimental

Samples of CdSe QDs tunable in size from 17 to 150 Å in diameter with standard deviations <4.5% were synthesized according to Ref. 5. The preparation of these dots involves injecting Cd and Se sources into a hot coordinating solvent and growing nucleated CdSe seeds to the desired dot size. Post-fabrication processing using size selective precipitation further narrows the sample size distribution and isolates the dots from the organic growth medium leaving each CdSe core derivatized by an organic monolayer. These CdSe QD samples have been structurally and optically well-characterized^{3,5,7-12}. The organic capping groups sterically stabilize the dots in solution. Optically thin and transparent (non-scattering), close packed QD solids were deposited from dispersions of these QD samples in mixed alkane¹⁸.

We optically study QD solids and solutions prepared from pure samples of single dots, mixed samples of small and large dots, and a broad sample distribution obtained by mixing 5 QD samples incremented by ~2 Å in dot diameter. The optical density (OD) of the thin QD solids was always <0.3 at the peak of the first excited state to minimize reabsorption of emitted photons. In the mixed solid, the OD of the large dots at the emission peak of the small dots was <0.05 so that absorption of the luminescence from the small dots by the large dots was negligible. The close packed CdSe QD solids were deposited on sapphire flats for optical measurements at cryogenic temperatures. A

Teflon spacer was used to separate the QD solids from a second sapphire window. Solutions of CdSe QDs were prepared by either dispersing the QDs in alkanes or in *n*-butyl benzene, a low temperature glass former. Luminescence QYs for the QD solids and solutions were measured relative to the known luminescence intensities of organic dyes. Dispersions of CdSe QDs and solutions of organic dyes were loaded into sample holders between two sapphire flats separated by either a Viton O-ring or Teflon spacer. Sample holders were mounted in a helium cryostat.

We used either a 300 W Hg-Xe arc lamp or a 100 W quartz-tungsten-halogen lamp to collect optical absorption spectra. The 457.9 nm line from an argon-ion laser or the Hg-Xe lamp in combination with a monochromator was used as the excitation source in cw photoluminescence (PL) measurements. The transmitted or emitted light was dispersed through a 0.33 m monochromator and the colors separated by either a 150 groove/mm or 300 groove/mm grating. The spectra were detected by an optical multichannel analyzer. Some cw PL spectra were collected using a SPEX Fluorolog-2 spectrofluorometer.

PL decays were measured using time correlated single photon counting. The samples were excited by 2.143 eV (580 nm) and 2.302 eV (540 nm) picosecond pulses generated by a cavity dumped dye laser synchronously pumped with the third harmonic of a mode-locked Nd:YAG laser. The setup was operated at a 1 MHz repetition rate with an overall time resolution of ~ 80 psec.

4.3 Structural Characterization

In chapter 2, we used the high resolution scanning electron microscope (HRSEM) to image the QDs building up three-dimensional QD solids. Figure 2.2 shows that the QDs form close packed glassy solids in which each dot remains separated from its neighbors by the organic capping groups. In solids prepared from a mixture of small and large dots, the arrangement of the dots in the solids depends on the composition of solvents used to deposit the QD solid. Figure 2.10(a) shows a QD solid prepared from a mixture of 82% 37.5 Å and 18% 57 Å CdSe QDs in a mixed solvent of octane and octanol. The small

and large dots have phase separated into ordered regions. Figure 2.10(b) shows that in a glassy QD solid, prepared from 82% 38.5 Å and 18% 62 Å CdSe QDs, the small and large dots remain intermixed. We study electronic energy transfer from the small to the large dots in the well-intermixed glassy QD solids.

We also used small-angle x-ray scattering (SAXS) to characterize the average local structure of the QDs in the glassy QD solids. The SAXS patterns for the QDs dispersed in PVB [Figure 2.5(a)] are the form factors for the individual QDs. Fitting the SAXS patterns by the Fourier transform of the form factor for a sphere yields the sample dot diameter. SAXS patterns for the QDs close packed in QD solids [Figure 2.5(b)] are the product of the scattering patterns of the individual QDs and the interference contributions as the positions of the QDs are correlated in the solid. Using the contribution from interferences, we generated pair distribution functions [Figure 2.5(c)] giving us the nearest neighbor distance between QDs in the solid. The diameter of the QDs and the nearest neighbor distance completely define the distances in the QD solids. The QD solids consist of close packed CdSe QDs separated by 11 ± 1 Å maintained by the organic capping groups.

4.4 Optical Spectroscopy

The sizes of the QDs in our samples are smaller than the bulk exciton Bohr radius in CdSe (56 Å)⁶. Excitation of a QD generates an electron-hole pair that is confined to and delocalized over the volume of the dot. The spectroscopic and photophysical properties of the QD are analogous to those of a large molecule. 10 K optical absorption and emission spectra of optically thin and clear (non-scattering), close packed QD solids prepared from samples of CdSe QDs ranging in size from 30.3 to 62.1 Å in diameter are shown in Fig. 4.1. The discrete absorption resonances and sharp band edge emission are characteristic of the size dependent, quantized electronic excitations observed in these same CdSe QD samples dispersed in solution. The electronic and optical properties of the QD solid are similar to those of a molecular solid.

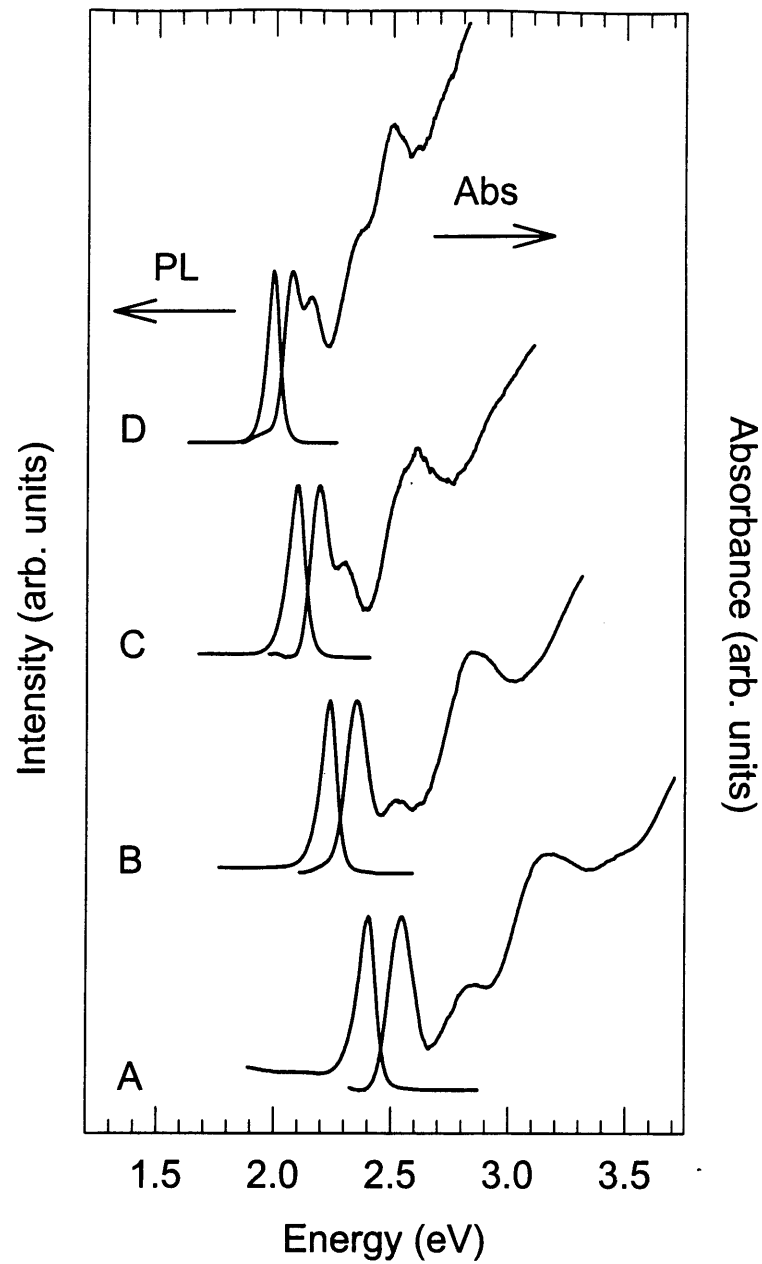


Figure 4.2 10K optical absorption and emission spectra of optically thin and clear, close packed QD solids prepared from samples of CdSe QDs (A) 30.3, (B) 39.4, (C) 48.0, and (D) 62.1 Å in diameter.

Electronic energy transfer between luminescent molecules in organic solids (chromophores) and between impurity centers in inorganic solids (phosphors) has been and remains an active area of research²⁰. Electronic energy transfer encompasses any process by which electronic energy is transferred from an excited molecule or atom (the donor) to a ground state molecule or atom (the acceptor), returning the donor to its ground state and promoting the acceptor to one of its higher excited states. Energy transfer is different from electronic transfer in that there is no net transport of charge, the charge neutral excitation is transferred as an entity from the donor to the acceptor. Radiationless transfer of electronic energy requires direct interaction between the excited donor and ground state acceptor. It is a one-step process in which de-excitation of the donor and excitation of the acceptor occur simultaneously. It is distinct from radiative transfer in which an intermediate photon is first emitted from the donor and then reabsorbed by the acceptor with no direct donor-acceptor interaction.

At intermolecular/interatomic separations of 5 to 100 Å, in the range of the interdot separations in our solids, long-range resonance transfer (LRRT) is the dominant energy transfer mechanism²⁰⁻²². LRRT of electronic excitations is a radiationless transfer process arising from coupling between the electromagnetic fields generated by the transition dipoles of resonant transitions in the excited donor and ground state acceptor. This donor-acceptor coupling is very weak so the rate of electronic energy transfer is slower than the rates of absorption and vibrational relaxation processes in the donor and acceptor. Electronic excitations are completely localized in the donor prior to being transferred to the acceptor. In systems of two dissimilar molecules, one the donor and the other the acceptor, LRRT is measured spectroscopically by the quenching of the luminescence QY or decrease in the luminescence lifetime of the donor or by the enhancement of the luminescence QY or increase in the luminescence lifetime of the acceptor. In order to observe LRRT, the acceptor must have both a transition resonant with the donor emission in which to accept the transferred excitation and a lower energy state in which to trap the excitation²⁰⁻²². Transfer of the excitation back to the donor is inhibited since no donor transition exists at that lower energy.

4.5 Mixed CdSe QD Solid

We use the size dependence of the electronic spectrum of the QDs to create a mixed system of 82% 38.5 Å (small) dots and 18% 62 Å (large) dots in which to optically study electronic energy transfer in QD solids. In the mixed solid, the small dots are the donors and the large dots are the acceptors. Fig. 4.2 is a cartoon representing the electronic transitions of the small and large dots. The large dot has a transition ($|g\rangle \rightarrow |A>_1$) resonant with the emitting energy of the small dot ($|g\rangle \leftarrow |D>$) and a lower energy state ($|A>_2$) in which to trap the excitation. The excitation cannot be transferred back since the small dots are transparent at the lower energy. Figure 4.3(a, b) shows the RT and 10 K donor-acceptor resonance (dotted lines) in the mixed QD solid calculated by overlapping the weighted emission spectrum of the small dots with the absorption spectrum of the large dots.

The absorption and emission features of the small and large dots in the mixed QD solid are spectrally well-separated [Fig. 4.4(a, b)]. RT and 10 K absorption spectra for the mixed QD solid are shown by solid lines in Fig. 4.4(c, d). Subtracting the spectral contributions from the large dots (dotted lines), we regain the spectra for the small dots (dashed lines) in the mixed QD solid. The absorption spectra for the mixed solid are sums of the absorption spectra of its small and large dot components. Electronic excitations are initially localized in individual small and large QDs in the solid.

Comparison of RT and 10 K luminescence spectra for the mixed system of dots dispersed in solution [Fig. 4.5(a, b)] with those for the dots close packed in the solid [solid lines, Fig. 4.5(c, d)] reveals a large increase in the ratio of the large to small dot luminescence QYs in the mixed solid. The samples were excited at 2.762 eV, labeled by arrow 1 in Fig. 4.4(c, d). Dotted lines in Fig. 4.5(c, d) plot the relative QYs for a pure, small QD solid (in the absence of large dots) and for the large dots in the mixed QD solid when excited to the red of the small dot absorptions. Excitation to the red of the small dot absorptions, labeled by arrow 2 in Fig. 4.4(c, d), excites only the large dots in the mixed QD solid. The QYs of the large dots are scaled by the relative QYs for large dots

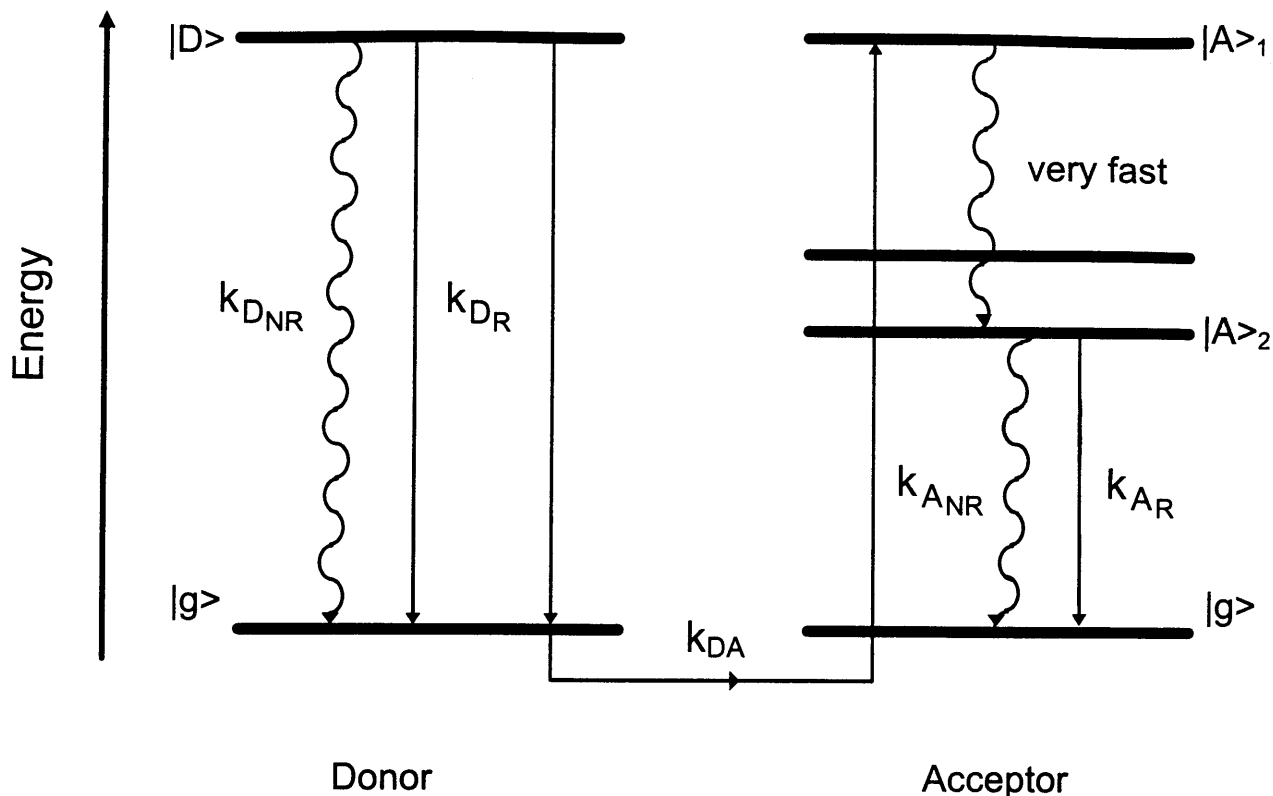


Figure 4.3 Cartoon depicting resonant transfer of electronic excitations from small (donor) to large (acceptor) CdSe QDs in a mixed QD solid. The energy levels shown are characteristic of the electronic spectra for the small 38.5 Å and large 62 Å QDs. $|g\rangle$ represents the ground states of the donor and acceptor, $|D\rangle$ is the lowest excited state of the donor, $|A\rangle_1$ and $|A\rangle_2$ are a higher excited state and the lowest excited state of the acceptor, respectively. The large dot has both a transition resonant with the emission of the small dot and a lower energy state in which to trap transferred excitations. In addition to the radiative and nonradiative pathways for decay of photoexcitations, labeled by k_{DR} and k_{DNR} for the small dots and by k_{AR} and k_{ANR} for the large dots, electronic energy transfer labeled by the rate k_{DA} offers another pathway for de-excitation of the small dots and excitation of the large dots.

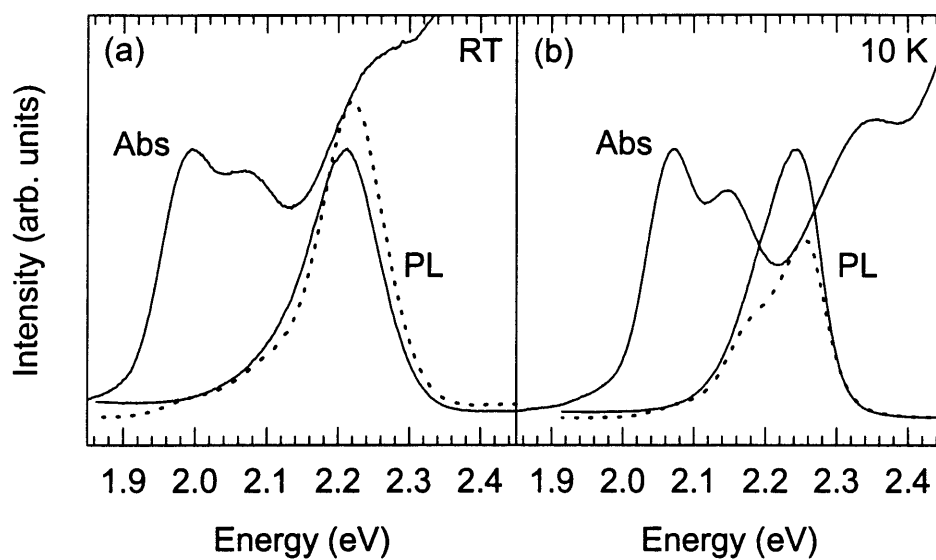


Figure 4.4 The (a) RT and (b) 10 K donor-acceptor resonance are shown by spectral overlap (dotted lines) of the emission from the 38.5 Å dots with the absorption of the 62 Å dots.

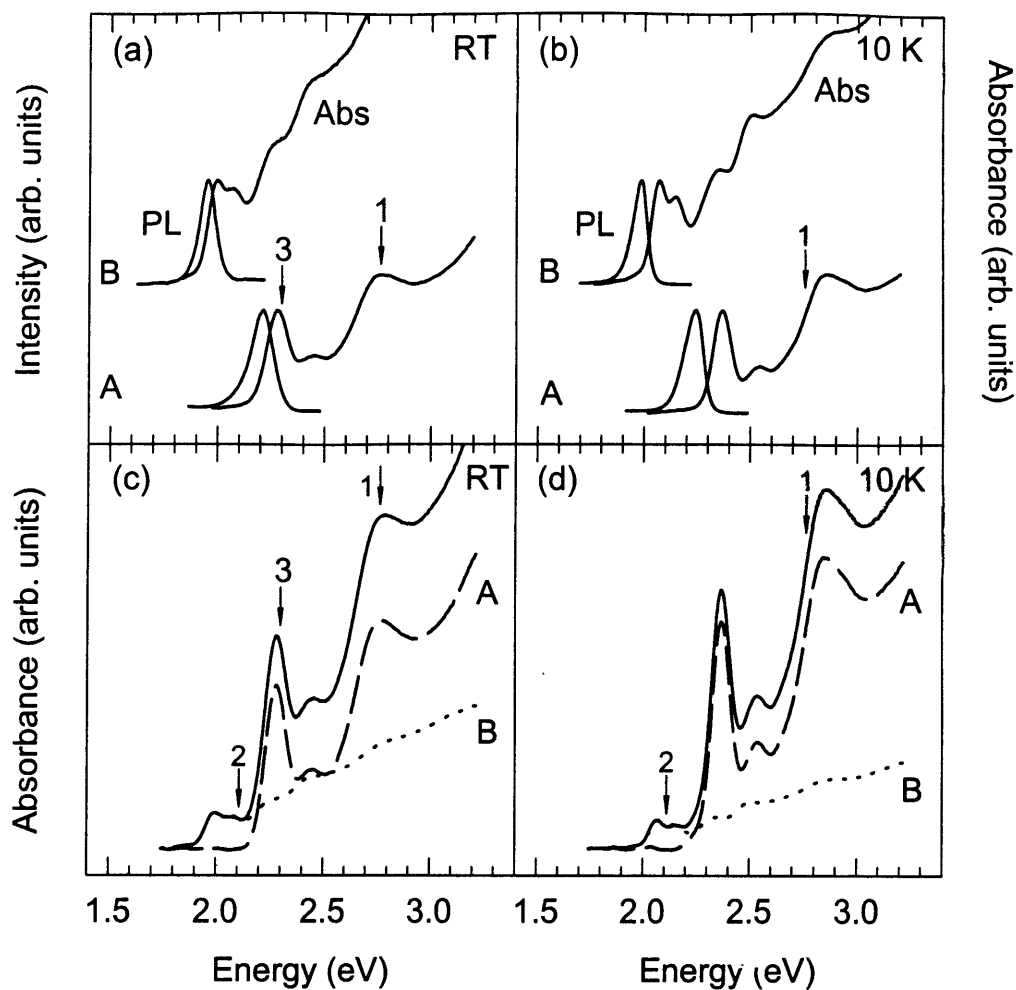


Figure 4.5 Optical absorption and emission spectra for 38.5 Å and 62 Å CdSe QD solids at (a) room temperature (RT) and (b) 10K. Optical absorption spectra for a mixed CdSe QD solid prepared from 82% 38.5 Å dots and 18% 62 Å dots (solid lines) at (c) RT and (d) 10K. The absorption spectra for the mixed QD solid are sums of the absorption spectra of its 38.5 Å (dashed lines) and 62 Å (dotted lines) QD components. Arrows indicate the (1) 2.762 eV (450 nm), (2) 2.143 eV (580 nm), and (3) 2.302 eV (540 nm) excitation energies used in cw and time resolved PL measurements which are to the blue and red of the small dot absorptions.

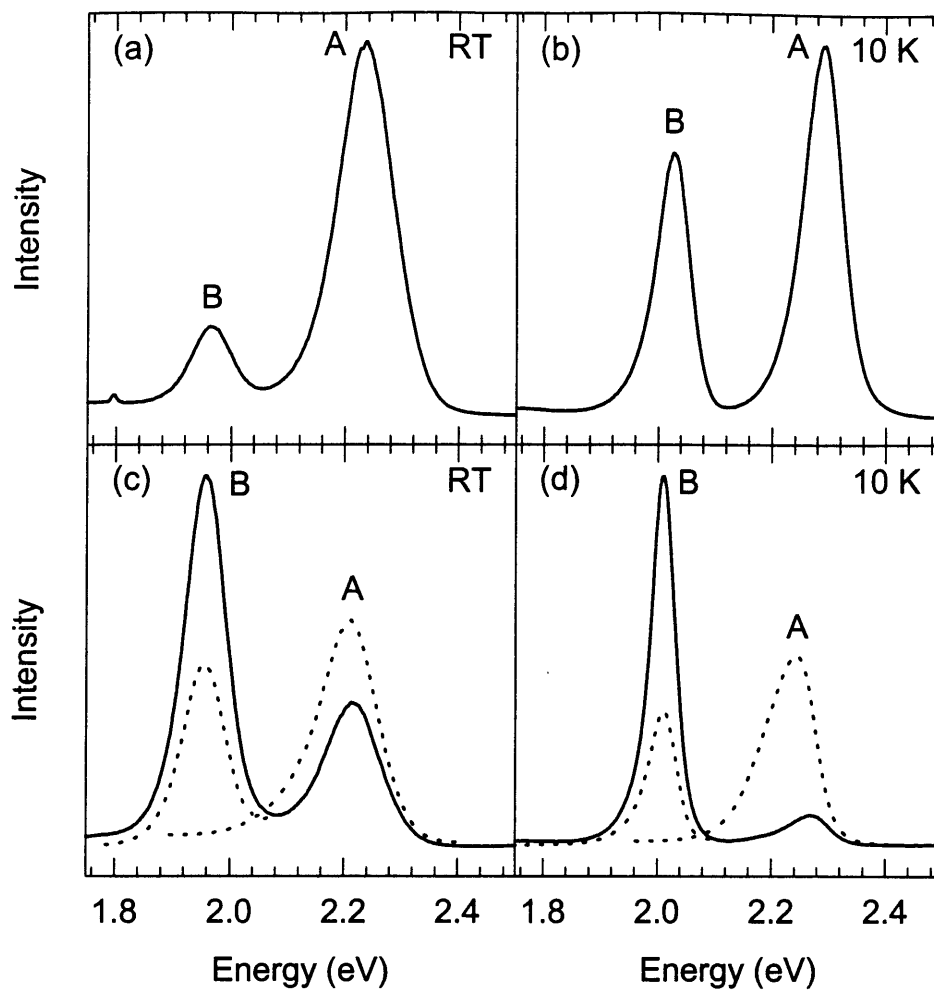


Figure 4.6 Emission spectra for 2.762 eV (arrow 1 in Fig. 4.5(c,d)) excitation of the mixed system of 18% 62 Å dots and 82% 38.5 Å dots (solid lines) dispersed in solution at (a) room temperature (RT) and (b) 10 K and close packed in the solid at (c) RT and (d) 10 K. Dotted lines plot the relative quantum yields for 38.5 Å dots in a pure QD solid and for 62 Å dots exciting the mixed QD solid to the red (2.143 eV, arrow 2 in Fig. 4.5(c,d)) of the 38.5 Å dot absorptions at (c) RT and (d) 10 K.

dispersed in solution when excited at the blue [arrow 1 in Fig. 4.4(a, b)] and red [arrow 2 in Fig. 4.4(a, b)] excitation energies. Scaling the QYs accounts for differences in source intensity and in the inherent QYs of the QDs at the two excitation energies. In luminescence, the spectra for the mixed QD solid are no longer superpositions of the small and large dot luminescence spectra. Exciting both the small and large dots in the mixed QD solid [arrow 1 in Fig. 4.4(c, d)] reveals quenching of the luminescence QY of the small dots accompanied by enhancement of the luminescence QY of the large dots. Our observations are consistent with electronic energy transfer from the small to the large dots in the mixed QD solid. Comparison of RT and 10 K luminescence spectra shows that the magnitude of these effects increases at lower temperatures.

4.5.1 Spectral Overlap of Donor Emission and Acceptor Absorption

We calculate the probability (P_{DA}) and rate (k_{DA}) of electronic energy transfer from donor to acceptor in our QD solids in terms of spectroscopic quantities. Förster theory relates the efficiency of energy transfer due to donor-acceptor dipole-dipole interactions to the spectral overlap of donor emission and acceptor absorption²⁰⁻²². Using the spectral overlap, shown by dotted lines in Fig. 4.3(a, b), we calculate the critical radius (R_o) for LRRT in our QD solids. R_o is the distance between donor and acceptor at which $k_{T...}$ equals the rate of donor de-excitation by competing mechanisms. R_o is a measure of energy transfer efficiency relative to R_{DA} , the physical distance between donor and acceptor in the QD solid. For a random orientation of transition dipoles²⁰⁻²²,

$$R_o \propto \left(\frac{\phi_D}{n^4} \int_0^{\infty} F_D(\tilde{\nu}) \epsilon_A(\tilde{\nu}) \frac{d\tilde{\nu}}{\tilde{\nu}^4} \right)^{1/6}, \quad (4.1)$$

where ϕ_D is the luminescence QY of the donor (0.0185 at RT and 0.2395 at 10 K), n is the refractive index of the QD solid, $F_D(\tilde{\nu})$ is the normalized spectrum for donor emission, and $\epsilon_A(\tilde{\nu})$ is the molar extinction coefficient for acceptor absorption. We assume the transition dipoles are randomly oriented as the transition dipole is defined by the CdSe unit cell and each dot is randomly oriented in the glassy solid. We calculate n

as the volume weighted average of that for the QDs (2.58 at RT and 2.54 at 10 K^{*,35}) and the organic cap (1.47 for trioctylphosphine⁴⁴), assuming a randomly close packed QD solid with the organic cap filling the interstices. The molar extinction coefficient for the small dots is calculated from its absorption spectrum using Beer's law, assuming the molar extinction coefficient at the peak of the first excited state is $1 \times 10^6 / \text{M} \cdot \text{cm}$. Using Eq. (4.1), we obtain $R_o = 47 \text{ \AA}$ at RT and 67 \AA at 10 K. The temperature dependence of R_o originates from the increased QY of the small dots with decreasing temperature.

4.5.2 Time Dependence of Electronic Energy Transfer

The time dependence of the luminescence decays for the small and large dots in the mixed QD solid gives us an independent measure of R_o and confirms the LRRT mechanism. Fig. 4.1 shows that in addition to the radiative (R) and nonradiative (NR) decays in the small and large dots, electronic energy transfer with rate k_{DA} offers another pathway for de-excitation of the small dots and excitation of the large dots. Figure 4.6 (dotted lines) shows RT luminescence decays monitoring the peaks in the PL spectra of Fig. 4.5(c) for the small dots in the pure QD solid (a) and the mixed QD solid (b) and for the large dots exciting the mixed solid to the blue [arrow 3 in Fig. 4.4(a,c)] (c) and red [arrow 2 in Fig. 4.4(c)] (d) of the small dot absorptions. The peaks in the luminescence decays are normalized to compare their time dependence. Electronic energy transfer from the small to the large dots is observed as the decrease in the luminescence lifetime of the small dots and the accompanied increase in the luminescence lifetime of the large dots.

The luminescence decays for the small dots in a pure QD solid (a) and for the large dots in the mixed QD solid excited to the red of the small dot absorptions (d)

* Refractive indices for the CdSe cores are calculated from the Moss rule⁴⁵, $n^4 = \frac{77}{E_g(\text{eV})}$ using the temperature dependent bulk E_g ³⁵.

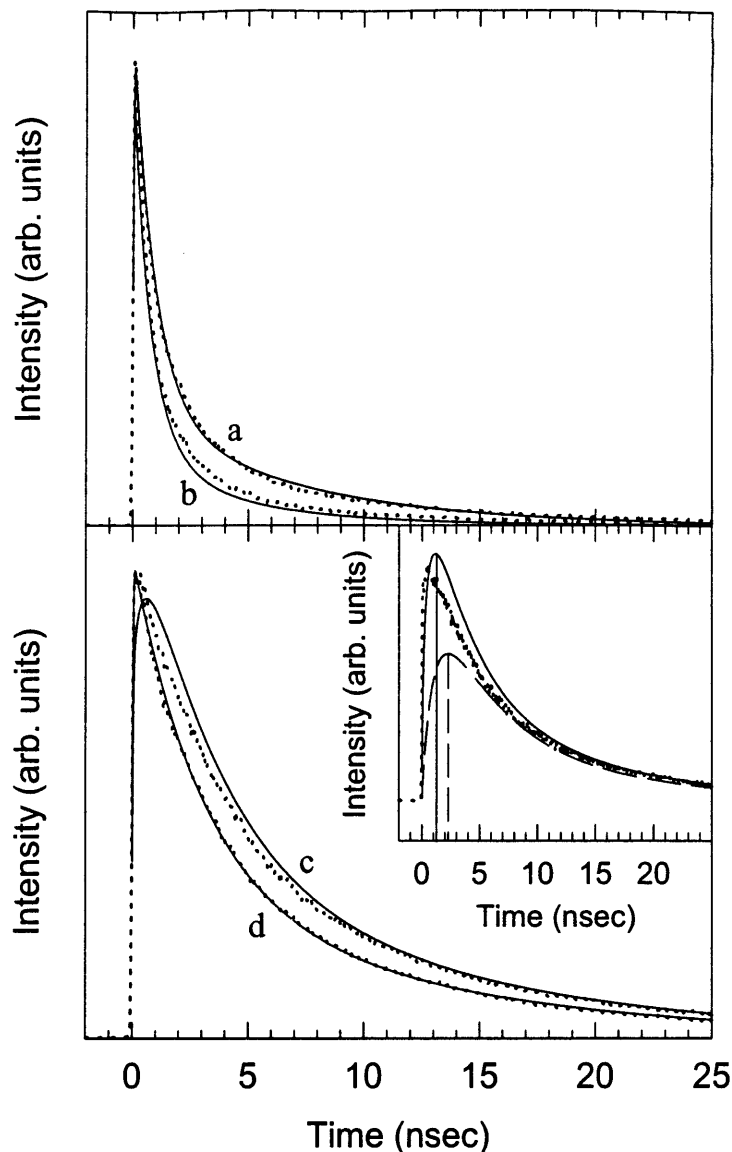


Figure 4.7 Luminescence decays monitoring the emission peak of the 38.5 Å dots in a pure QD solid (a) and in the mixed QD solid (b) and for the 62 Å dots exciting the mixed QD solid to the blue (c) and red (d) of the small dot absorptions. The peaks in the decays are normalized to compare their time dependence. Decays for the 38.5 Å (a) and 62 Å (d) QDs in the absence of energy transfer are fit to biexponentials (solid lines). The decrease in the luminescence lifetime of the 38.5 Å dots in the mixed QD solid is fit by Förster's decay law for LRRT of electronic excitations [solid line (b)]. The increase in the luminescence lifetime for the large dots upon transfer of electronic excitations from the small dots is calculated for LRRT [solid line (c)]. The fit and calculated curves are scaled by their relative QYs to the experimental decays. The inset compared the energy transfer contribution to the decay of the large dots found experimentally (dotted lines) with the LRRT (solid line) and the exciton diffusion (dashed line) mechanisms. The instrumental response was deconvoluted in all our fits and calculations.

correspond to exciton decay times by radiative and nonradiative processes in the absence of energy transfer. We use nonlinear least squares methods to fit these non-exponential luminescence decays by biexponentials [solid lines (a) and (d)], representing distributions of lifetimes for the QDs in the samples*. The excited state populations for the small dots $[n_D(t)]$ and the large dots $[n_A(t)]$ including electronic energy transfer from the small to large dots are described by the rate equations⁴⁰

$$\dot{n}_{D_i}(t) = G_{D_i}(t) - \frac{n_{D_i}(t)}{\tau_{D_i}} - k_{DA}(t)n_{D_i}(t) \quad \text{where} \quad n_D(t) = \sum_{i=1,2} n_{D_i}(t) \quad (4.2)$$

$$\dot{n}_{A_j}(t) = G_{A_j}(t) - \frac{n_{A_j}(t)}{\tau_{A_j}} + k_{DA}(t)n_D(t) \quad \text{where} \quad n_A(t) = \sum_{j=1,2} n_{A_j}(t) \quad (4.3)$$

where $G_{D_i}(t)$ [$G_{A_j}(t)$] represents the donors [acceptors] excited directly by the pulsed source, $n_{D_i}(t)$ [$n_{A_j}(t)$] is the time dependent number of excited donors [acceptors] in the mixed QD solid with lifetime $\tau_{D_i}(t)$ [$\tau_{A_j}(t)$], and D_i [A_j] indexes the donors [acceptors] characterized by short and long lifetimes. We assume that all small dots have the same energy transfer rate, k_{DA} . The time dependence of the luminescence distinguishes the two most common radiationless energy transfer mechanisms in solids, LRRT and exciton diffusion. LRRT has $k_{DA}(t) \propto t^{-1/2}$ while exciton diffusion has a time independent k_{DA} ⁴⁰.

4.5.2.1 Long-Range Resonance Transfer

Solving Eq. (4.2) for LRRT, we fit the decrease in the PL lifetime for the small dots in the mixed solid by Förster's decay law⁴⁰ [solid line (b)]

* We assume that at RT the distribution of decay rates originates from a distribution in nonradiative lifetimes.

$$n_{D,MIXED}(t) = n_{D,PURE}(t) \exp \left[-\gamma \left(\frac{\pi t}{\bar{\tau}_D} \right)^{1/2} \right] \quad (4.4)$$

where $n_{D,PURE}(t)$ is the biexponential fit [solid line (a)] and $\bar{\tau}_D$ is the weighted average lifetime for the small dots in the pure QD solid, and $\gamma = C \left(\frac{4}{3} \pi R_o^3 \right)$. C is the concentration of large dots in the mixed QD solid and is calculated using Beer's law and the film thickness measured by profilometry. R_o is then the only adjustable parameter in the fit which yields $R_o = 48 \text{ \AA}$.

Using Eq. (4.4) to solve Eq. (4.3), we calculate the increase in the luminescence lifetime for the large dots in the mixed solid as⁴⁰

$$n_{A,BLUE}(t) = n_{A,RED}(t) + A_D \sum_{j=1,2} n_{A_j}(0) \int_0^t \exp \left(\frac{s-t}{\tau_{A_j}} \right) n_D(s) k_{DA}(s) ds. \quad (4.5)$$

The first term $n_{A,RED}(t)$ is the biexponential fit [solid line (d)] to the luminescence decay for the large dots in the mixed QD solid when excited to the red of the small dot absorptions. It represents the contribution to the luminescence decay from photoexcitations generated directly in the large dots by the source. The second term describes the decay of large dot excitations that were resonantly transferred from the small dots. The integrand is proportional to the time dependent LRRT rate and the exponent describes the decay of large dot excitations, with rate $\left(\frac{1}{\tau_{A_i}} \right)$, generated at time s upon transfer from the small dots. We sum the contributions from dots characterized by lifetimes τ_{A_j} with weights $n_{A_j}(0)$. A_D represents the relative absorbance of the small to large dots at the blue excitation. The calculated curve for LRRT is shown by the solid line (c). The calculated curve for LRRT reproduces both the time dependence of the experimental decay and the enhancement in the luminescence intensity for the large dots.

4.5.2.2 Exciton Diffusion

Solving Eqs. (4.2) and (4.3) for exciton diffusion, we fit the decrease in the luminescence decay for the small dots and calculate a curve for the increase in the luminescence decay for the large dots. The fit to the decay for the small dots is similar to that found for LRRT and is not shown for clarity. We compare the experimental and modeled energy transfer decays in the inset of Fig. 4.6. The experimental data (dotted lines) are calculated by subtracting experimental curves (c) and (d) when scaled by their relative QYs. Comparison of the calculated curve for LRRT, shown by the solid line, and that for exciton diffusion, shown by the dashed line, shows that for the same average k_{DA} , LRRT leads to a more rapid transfer of energy than does exciton diffusion. The LRRT mechanism reproduces both the time dependence of the decay and the increase in the luminescence intensity for excitations transferred to the large dots, while exciton diffusion does not. This may be expected since exciton diffusion is the dominant energy transfer process for donor-acceptor separations of 2 to 5 Å²¹. The distance of closest approach in our QD solids is ~11 Å, the separation between the surfaces of neighboring dots.

4.5.3 Quenching of the Luminescence Quantum Yield of the Small QDs

We also calculate R_0 for LRRT in our QD solids by the quenching of the luminescence QY for the small dots in the mixed QD solid relative to that for the small dots in a pure QD solid. Integrating $n_{D,PURE}(t)$ and Eq. (4.4), assuming a single weighted average lifetime for the small QDs, yields expressions for the luminescence QYs for the small dots in the pure and mixed solids. The ratio of their luminescence QYs⁴⁰

$$\frac{\Phi_{D,MIXED}}{\Phi_{D,PURE}} = 1 - \frac{\pi}{2} \gamma \exp\left(\frac{\pi\gamma^2}{4}\right) \operatorname{erfc}\left(\frac{\pi^{1/2}\gamma}{2}\right) \quad (4.6)$$

is used to find γ , which yields values for $R_0 = 47$ Å at RT and 81 Å at 10 K.

4.5.4 Summary

The spectral overlap of donor emission and acceptor absorption and the quenching of the luminescence QY of the donor give us independent measures of $R_o = 47 \text{ \AA}$ at RT and 67 \AA and 81 \AA , respectively, at 10 K. Time dependent measurements at RT show that the LRRT mechanism for electronic energy transfer reproduces the luminescence decays for the small and large dots in the mixed QD solid with $R_o = 48 \text{ \AA}$. Comparison of R_o with the distance between donor and acceptor centers ($R_{DA} = 61.25 \text{ \AA}$), measured from SAXS data, reveals that dipolar coupling between QDs is a nearest neighbor interaction. Using the average lifetime of the small dots from the luminescence decays [curve (a), Fig. 6] and R_{DA} from SAXS data, we calculate k_{DA} for LRRT in our QD solids using

$k_{DA} = \frac{1}{\tau_D} \left(\frac{R_o}{R_{DA}} \right)^6$. We obtain $k_{DA} = 1 \times 10^8 \text{ sec}^{-1}$ at RT, consistent with

characteristic rates for LRRT²¹. The relative rates of k_{DA} and $\frac{1}{\tau_D}$ or the relative

distances of R_o and R_{DA} are used to calculate the probability of energy transfer P_{DA} , given by⁴⁶

$$P_{DA} = \frac{k_{DA}}{k_{DA} + \frac{1}{\tau_D}} = \frac{R_o^6}{R_o^6 + R_{DA}^6}. \quad (4.7)$$

Eq. (4.7) yields energy transfer probabilities of 0.17 at RT and 0.63 at 10 K. The increase in P_{DA} also arises from the increase in QY for the small dots at 10 K and explains the increased magnitude of the energy transfer effects seen at low temperature in Fig. 4.5(c, d).

4.6 Single Size CdSe QD Solids

The absorption spectra of the QD solids and their parent solutions are indistinguishable. This suggests that electronic excitations are initially localized in the

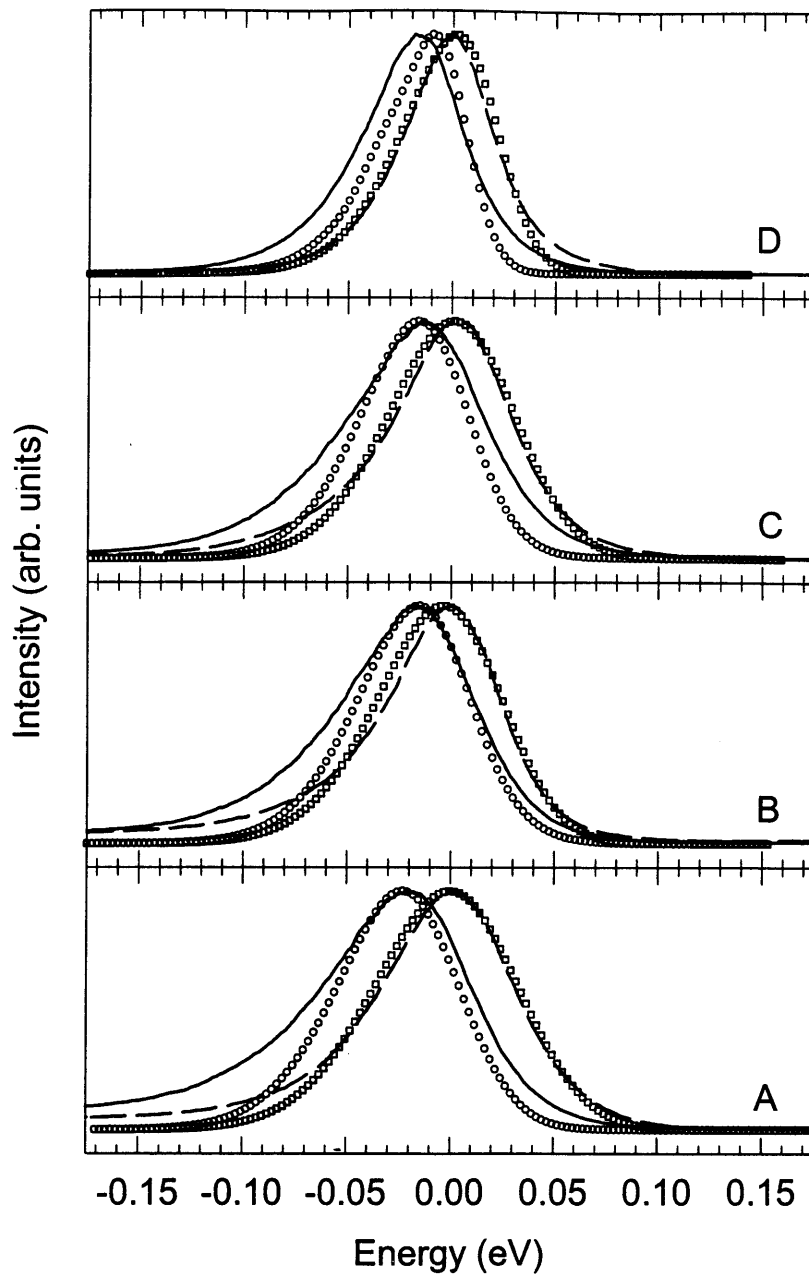


Figure 4.8 Comparison of 10 K luminescence spectra for (A) 30.3, (B) 39.4, (C) 48.0, and (D) 62.1 Å dots dispersed in solution (dashed lines) and close packed in QD solids (solid lines). Absorption spectra for these samples are shown in Fig. 4.2. The luminescence spectra are plotted relative to the luminescence peaks for the solutions. Fits to the solution spectra (open squares) are obtained by convoluting Gaussian inhomogeneous distribution with size-dependent “single dot” luminescence spectra. Simulated emission spectra (open circles) for the QD solids allow for energy transfer within the sample inhomogeneous distributions.

individual QDs. Figure 4.7 plots the 10 K luminescence spectra for the CdSe QD solids (solid lines) shown in Fig. 4.1 relative to those for the dots dispersed in a frozen solution (dashed lines). The emission lineshapes for the QD solids are red shifted and accentuated on the red side of the distributions. The magnitude of the red shifts range from 15 to 35 meV at 10 K, varying from sample to sample, showing no discernible size dependence, and decreasing with increasing temperature. The shifts are reversible upon redispersion of the QD solids. The absorption and luminescence spectra for the QD samples dispersed in matrices varying in polarity and in dielectric constant show no solvent effects.

4.6.1 Sample Inhomogeneous Distribution

In each of our QD samples there still remains an inhomogeneous distribution in the emitting energies of our QDs. The full luminescence spectra for the samples dispersed in solution are each the sum of structured, “single” dot emission spectra. The structured fluorescence of the individual QD is washed out by sample spectral inhomogeneity. The origin of the inhomogeneous distribution is primarily from the size distribution. We use smaller and larger to refer to dots whose spectra are shifted to the blue and red relative to each other. Studies using fluorescence line narrowing spectroscopy optically select a subset of the sample inhomogeneous distribution, revealing the structured fluorescence characteristic of the individual QD^{10,11}. The “single” dot emission spectrum is composed of a narrow band edge emission and its LO-phonon progression, which we model by

$$E(\nu, \nu') = \sum_{n=0}^4 \frac{1}{\sqrt{2\pi}\gamma_n} \frac{(S_e)^n}{n!} \exp\left(-\frac{[\nu - (\nu' - n\omega_{LO})]^2}{2\gamma_n^2}\right) \quad (4.8)$$

where ν' is the position of the zero LO-phonon line in emission and S_e is the strength of the exciton-LO-phonon coupling in emission^{10,11}. The sum is taken over the first 5 LO-phonon replicas which are separated by the LO-phonon frequency for CdSe, ω_{LO} , and have linewidths γ_n . The parameters S_e and γ_n are a function of the size of the dot and are found in Ref. 10. Using the parameters for the average size QD in the sample, we fit the full luminescence spectra using nonlinear least squares methods (open squares, Fig. 4.7) with the convolution integral^{10,11}

$$E_{PL}(\nu) = C \int E(\nu, \nu') D(\nu', \nu_0) d\nu'. \quad (4.9)$$

We assume that the sample inhomogeneous distribution $D(\nu', \nu_0)$ is a Gaussian function centered at ν_0 with standard deviation γ . C is a constant with the appropriate units.

4.6.2 Probability of Electronic Energy Transfer

Our observations (Fig. 4.7) are consistent with electronic energy transfer from the smaller to the larger dots within the sample inhomogeneous distribution⁴⁷. Electronic energy transfer leads to quenching of the blue luminescence accompanied by enhancement of the red luminescence. This manifests itself as a red shift in peak position and an asymmetric and narrowed emission lineshape. This is similar to what has been observed in the photosynthetic bacterium *Rhodospirillum rubrum*, where electronic energy transfer within a spectrally inhomogeneous distribution leads to a red shift in emission and an asymmetric lineshape⁴⁸.

We calculate an average R_0 for LRRT in each of our QD solids from spectral overlap, using Eq. (4.1). Now, $F_D(\tilde{\nu})$ is the normalized emission spectrum for the QD sample, given by the emission spectrum for the QDs dispersed in solution; $\epsilon_A(\tilde{\nu})$ is the molar extinction coefficient for the QDs, obtained from the absorption spectrum of the QD solid; and ϕ_D is the luminescence QY of the QD solid. Luminescence quantum yields (QYs) for the solids measured at 10 K [RT] range from ~ 0.01 to 0.2 [~ 0.001 - 0.01], a factor of ~ 10 lower than QYs measured for the dots in solution. Reduction in the QYs of the solids may arise in part from charge separation and transport between the dots, decreasing the probability of both the electron and hole residing in the same dot. Energy transfer to non-luminescing dots probably also contributes to quenching of the QY. We obtain values of $R_0 = 37.9, 35.4, 47.3,$ and 53.9 \AA for samples A, B, C, and D, respectively. The values for R_0 show an increase with the increased spectral overlap in samples of larger size QDs, but vary more significantly with the QY for the QD solid. This is seen for sample B whose QY is lower than for the other three samples. Comparison of R_0 with $R_{DA} = 41.3, 50.4, 59.1,$ and 73.1 \AA for samples A, B, C, and D,

obtained from SAXS data, shows energy transfer in QD solids prepared from single size dots also arises from only nearest neighbor inderdot interactions. Using Eq. (4.7), we calculate $P_{DA} = 0.38, 0.11, 0.21,$ and 0.14 for each of the solids, A, B, C, and D. In general, values for P_{DA} show a decrease with increasing dot size as R_{DA} increases faster than R_o . Again P_{DA} varies with the QY of the solid, seen by the lower probability for sample B.

4.6.3 Simulation of Energy Transfer within the Sample Inhomogeneous Distribution

Starting with the luminescence profile for the inhomogeneous distribution of QDs dispersed in solution, we simulate energy transfer between each dot and its shell of nearest neighbors in a three-dimensional close packed QD solid. The number of acceptors in the nearest neighbor shell for a potential donor with excitation energy ν_{em_i}

$$N_A(\nu_{em_i}) = \frac{12}{\sqrt{2\pi\gamma}} \int_{-\infty}^{\nu_{em_i}} \exp\left[-\frac{(\nu - \nu_o)^2}{2\gamma^2}\right] d\nu \quad (4.10)$$

is represented by the probability that the 12 proximal dots are larger in size, having lower energy states ($\nu \leq \nu_{em_i}$). Again, transfer of energy from larger to smaller dots is not possible since the smaller dots are transparent to the lower energy excitations in the larger dots.

The probability that dots within the sample inhomogeneous distribution are not quenched by energy transfer to larger dots and emit their energy is given by

$$D(\nu_{em_f} = \nu_{em_i}) = \frac{1}{\sqrt{2\pi\gamma}} \exp\left[-\frac{(\nu_{em_i} - \nu_o)^2}{2\gamma^2}\right] (1 - P_{DA})^{N_A(\nu_{em_i})} \quad (4.11)$$

where $(\nu_{em_f} = \nu_{em_i})$ indicates that the energy of the photons emitted are equivalent to the initial energy in the dots. As the concentration of neighboring acceptors increases for the smaller dots in the distribution, the probability that they are quenched by larger dots

increases. The probability that dots with energy ν_{em_i} are quenched and their energy transferred to and emitted from acceptors at $\nu_{em_f} \leq \nu_{em_i}$ is described by the integral

$$A(\nu_{em_f}) = \int_{\nu_{em_f}}^{\infty} \frac{\frac{12}{2\pi\gamma^2} \exp\left[-\frac{(\nu_{em_f} - \nu_0)^2}{2\gamma^2}\right] \exp\left[-\frac{(\nu_{em_i} - \nu_0)^2}{2\gamma^2}\right] \left[1 - (1 - P_{DA})^{N_A(\nu_{em_i})}\right]}{N_A(\nu_{em_i})} d\nu_{em_i} \quad (4.12)$$

We assume that transfer to and emission from any of the acceptors is equally probable. The emission spectrum for the QD solid is then a sum of the emission from dots which were not quenched, $D(\nu_{em_f} = \nu_{em_i})$, plus the emission from acceptors which were enhanced, $A(\nu_{em_f})$, upon energy transfer from a donor with energy $\nu_{em_i} \geq \nu_{em_f}$. The luminescence spectra calculated for each of the QD solids are shown by open circles in Fig. 4.7. The simulated spectra that allow for energy transfer within the sample inhomogeneous distributions reproduce the experimentally observed red shift. The quality of the simulated spectra relies on our ability to initially fit the sample inhomogeneous distribution. The inability of a Gaussian distribution to reproduce the red tail in the luminescence of dots dispersed in solution becomes magnified in the solids as energy transfer from the small to the large dots enhances the red tail of the luminescence.

4.6.4 Effects of Sample Inhomogeneous Distribution

Figure 4.8(a) compares the 10 K absorption and luminescence spectra for QD solids and dispersions prepared from samples averaging 39 Å in diameter with a narrow ~4.5% (sample A) and a broad ~12% (sample B) inhomogeneous distribution. The states resolved in the absorption spectrum of sample A are obscured in B by the increased polydispersity. The linewidth in luminescence is also broadened by the increased inhomogeneous distribution of B. Comparison of the luminescence spectra for the narrow and broad samples dispersed in solutions (dashed lines) and close packed in solids (solid lines) reveals an increase in the magnitude of the red shift for the solid with increased inhomogeneous distribution. The magnitude of the red shift for sample A is

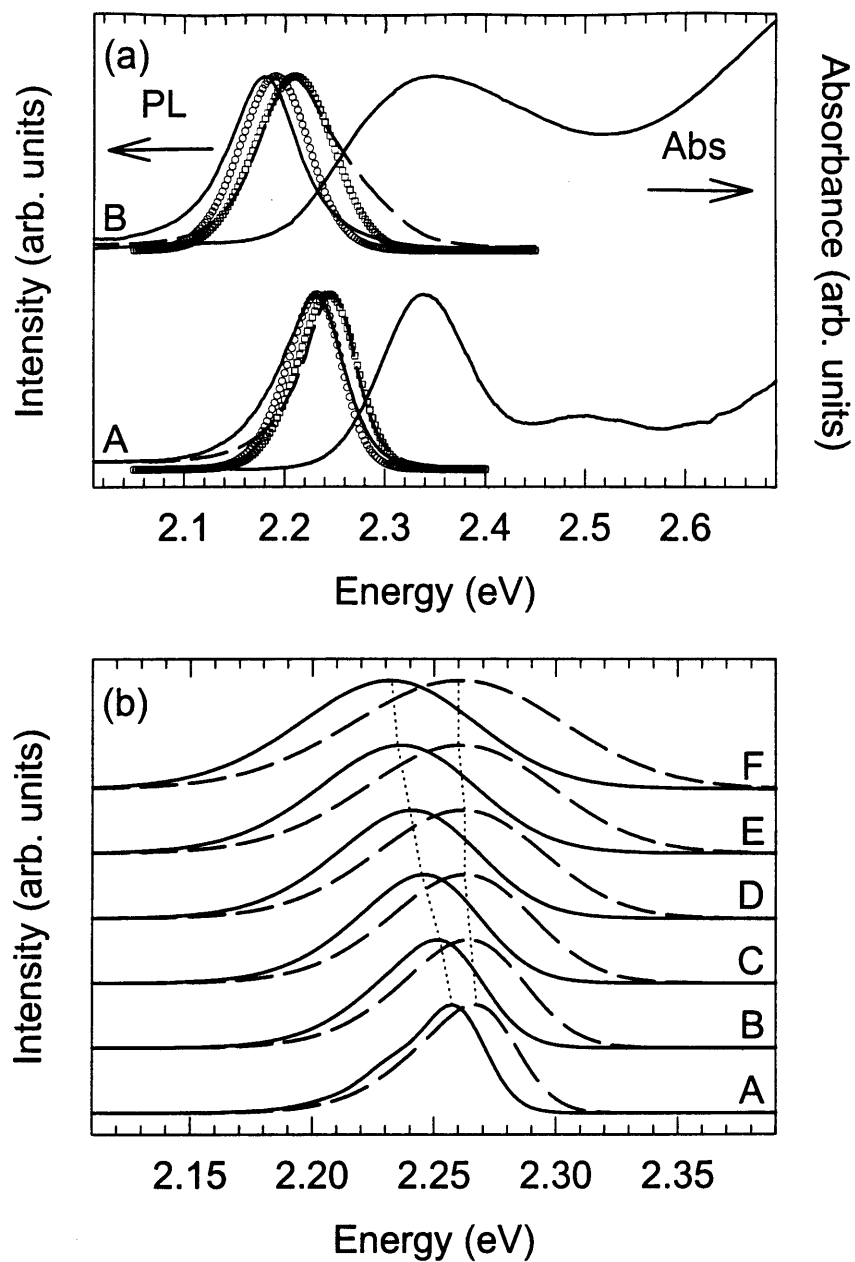


Figure 4.9 (a) 10 K absorption and luminescence spectra for samples with (A) narrow and (B) broad sample inhomogeneous distributions dispersed in solution (dashed lines) and close packed in QD solids (solid lines). Simulated luminescence spectra (open squares) fit to the solution spectra and calculated spectra (open circles) allowing for energy transfer within each of the sample inhomogeneous distributions. (b) (Dashed lines) Calculated emission spectra for 39 Å CdSe QD samples with (A) 1.5%, (B) 2%, (C) 2.5%, (D) 3%, (E) 3.5%, and (F) 4% sample inhomogeneous distributions. (Solid lines) Simulated emission spectra allowing for energy transfer within the sample inhomogeneous distributions.

14.6 meV while that for sample B is 29.6 meV. Close inspection reveals a small narrowing of the emission lineshape for the QD solid for sample A [difference between solution and solid of 11.2 meV full width at half maximum (FWHM)] and a noticeable, larger narrowing of the emission lineshape for the QD solid for sample B [difference between solution and solid of 22.9 meV FWHM]. The increased magnitude of the red shift and the narrowing of the emission lineshape with increasing inhomogeneous distribution are observed both at RT and 10 K.

We again fit the luminescence of the solutions (open squares) and simulate the expected luminescence of the solid, assuming energy transfer within the distribution (open circles). The simulated spectra show that energy transfer within the sample inhomogeneous distribution accounts for both the increased red shift and narrowing of the emission lineshape with the larger distribution of sample B.

Figure 4.8(b) illustrates the expected dependence of the red shift on size distribution. Fig. 4.8(b) shows simulated emission spectra for six 39 Å dot samples with increasing inhomogeneous distributions if dispersed in solution (dashed lines) and close packed in QD solids (solid lines). P_{DA} for LRRT in each of the six simulated QD solids is kept constant at 0.25. The dotted lines are used to follow the peaks of spectra. Increasing the sample inhomogeneous distribution for the QDs dispersed in solution broadens and slightly red shifts the simulated emission lineshape. The spectra for the solids show that the magnitude of the red shift and the narrowing of the emission lineshape becomes more prominent with increased spectral inhomogeneity. The magnitude of the red shift in the luminescence of the solids is not a simple measure of energy transfer efficiency. The red shift reflects both the efficiency of energy transfer and the spectral inhomogeneity of the QD sample.

4.6.5 Concentration Dependence of Electronic Energy Transfer

Fig. 4.9 shows the PL spectra for 62 Å CdSe QDs dispersed in solution (open circles) and close packed in QD solids (filled circles). To further understand the observed red shift and modified emission lineshape for the QD solids, we dispersed

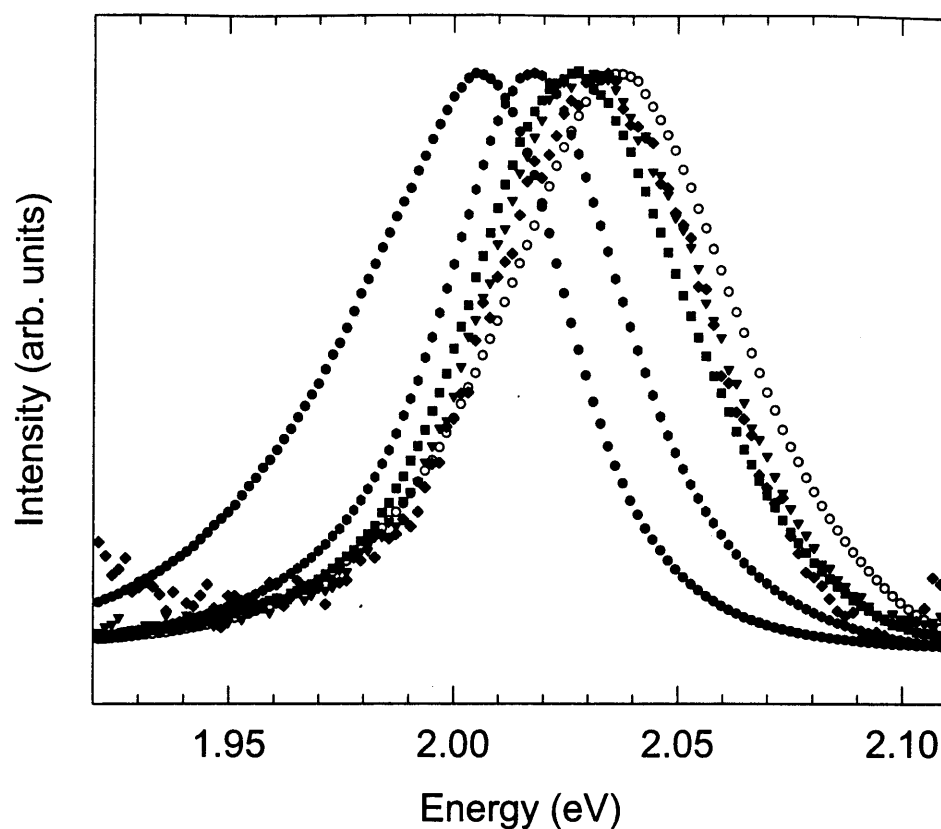


Figure 4.10 10 K luminescence spectra for 62 Å CdSe QDs close packed in a solid (filled circles) and dispersed in solution (open circles). Luminescence spectra for 62 Å QDs dispersed in matrices of 38.5 Å QDs shift blue with decreasing concentrations of the 62 Å QDs [18% (filled hexagons), 6.2% (filled squares), 3.2% (filled triangles pointed down), and 2.1% (filled diamonds)] approaching the luminescence of the dots dispersed in solution.

varying concentrations of the 62 Å QDs in matrices of smaller 38.5 Å QDs, producing glassy solids. Decreasing the concentration of the 62 Å dots increases their average separation and the probability that two large dots will be nearest neighbors. As the concentration of the 62 Å dots is decreased, the PL spectra of the 62 Å dots shifts blue approaching the solution luminescence at the lowest concentration. The emission lineshape for the dots also regains its “Gaussian” appearance as the dots are diluted in the matrix of smaller dots.

4.7 Conclusion

The physics of interdot interactions between proximal QDs is important in understanding the fate of electronic carriers and excitations generated in QD structures. In this chapter, we present spectroscopic evidence of electronic energy transfer in close packed CdSe QD solids arising from dipole-dipole interdot interactions between proximal dots. In a mixed system designed from small and large dots, electronic energy transfer from the small to the large dots is observed as luminescence quenching of the small dots and luminescence enhancement of the large dots. Using Förster’s theory for LRRT, we obtain independent and consistent measures of the energy transfer efficiency from spectral overlap considerations and from the quenching of the luminescence of the small dots in the mixed QD solid. The decrease in the luminescence decay for the small dots and the increase in the luminescence decay for the large dots is reproduced by the LRRT model with the same energy transfer efficiency. In QD samples of single size dots, electronic energy transfer within the sample inhomogeneous distribution reproduces the observed red shift and narrowing of the emission lineshape in close packed QD solids. These effects of energy transfer on the emission lineshape for the QD solid become more prominent as the inhomogeneous distribution of the sample increases. Comparison of R_0 with the distance between neighboring QDs reveals that electronic energy transfer in QD solids arises from nearest neighbor dipole-dipole interactions.

Chapter 5

Photoconductivity in Close Packed CdSe Quantum Dot Solids

5.1 Introduction

Building solids from nanometer size semiconductor quantum dots (QDs) presents opportunities to engineer the electronic and optical properties of materials on the nanometer scale. Individual semiconductor QD building blocks have size dependent electronic and optical properties. Three-dimensional quantum confinement effects collapse the bulk density of states into discrete electronic states that shift to higher energy as the diameter of the QD decreases². Close packing the QDs gives rise to physically interesting collective physical phenomena as proximal QDs interact and to new solid state materials with potentially useful electronic, optical, and optoelectronic properties. Understanding the interactions between QDs is the first step in designing materials and devices with tailored electronic and optical properties. Engineering the length and electronic structure of the spacer between the QDs may be used to tune the interdot couplings and therefore the properties of QD solids.

Recent advances in the fabrication of QD solids by lithography¹⁴, molecular beam epitaxy¹⁵, and wet chemical methods¹⁶⁻¹⁸ makes the study of interdot interactions possible. Optical studies of two- and three-dimensional close packed semiconductor and metal QD solids reveal optical properties distinct to the solid state as neighboring QDs interact. Aggregates of metal clusters show a red shift in the plasma resonance from that of individual clusters as the electronic wavefunctions extend over many clusters⁴⁹. Three-dimensional CdS and CdSe QD solids show red shifts in their luminescence spectra from that for dispersed QDs^{16-18,24}. In chapters 3 and 4 we showed

spectroscopically that in close packed CdSe QD solids interaction between the transition dipoles of neighboring QDs leads to electronic energy transfer between the QDs in the solids^{23,24}. Energy transfer within the inhomogeneous distribution of QDs in a sample accounts for the observed differences in the emission spectra for close packed QD solids from that for dispersed QDs.

Close packed QD solids are also of great interest for their potentially novel electronic and optoelectronic properties. The discrete nature of the QD's density of states has generated a lot of interest in resonant tunneling of single carriers and in Coulomb blockade effects in junctions containing a single metal or semiconductor QD⁴. Most electrical measurements on single QDs have studied QDs that are either electrostatically defined by many electrodes or prepared by lithographic techniques. Recently, the Coulomb staircase was also observed in colloidal metal and semiconductor QDs^{50,51}. Building arrays of QDs which demonstrate these novel conduction properties has raised interest in understanding carrier transport through coupled QDs and in their potential application in computational and memory devices^{41,52}. Taking advantage of the unique optical properties of semiconductor QDs presents opportunities for QD solids as optoelectronic materials. Close packed layers of CdSe QDs sandwiched between polymeric electron and hole transport layers electroluminescence with energies characteristic of the QDs³⁷. Previously, it was shown that dispersing semiconductor QDs in polymer matrices sensitizes the photoconductive properties of a host polymer⁵³. Sintered nanocrystalline particles of TiO₂, ZnO, and CdSe, have also been used to transport charge in photoelectrochemical cells⁴³.

In this chapter, we study the size dependent, electronic transport properties of close packed QD solids by investigating their photoconductive properties. We present observations and analysis of photoconduction in close packed solids prepared from CdSe QDs ranging in size from ~30 to 50 Å in diameter ($\sigma < 4.5\%$). In the dark, the QD solids are highly insulating since the effective bandgap of the QDs is large, leading to a small number of intrinsic carriers. Photoexcitation of the QDs in the solids creates a source of excess charge carriers. We measure the photocurrents generated in the QD solids as a

function of voltage, excitation energy, excitation intensity, and temperature to elucidate the mechanisms of charge generation, separation, and transport.

5.2 Experimental

CdSe QD samples tunable in size from 17 to 150 Å in diameter with standard deviations <4.5% were prepared by wet chemical synthesis⁵. The surface of the QDs are coordinated by a monolayer of trioctylphosphine chalcogenide moieties which sterically stabilize the QDs in solutions. Optically thin and clear, close packed QD solids were deposited from solutions of these QD samples¹⁸. The individual QDs^{3,5,7-12} and the close packed QD solids^{16,18,23,24} have been structurally and optically well-characterized. The QD solids are composed of close packed CdSe QDs with an interdot separation of 11 ± 1 Å maintained by the organic capping groups¹⁸. Optical absorption and emission spectra for the QD solids exhibit the discrete absorption resonances and sharp band edge emission characteristic of the size dependent, quantized electronic transitions of these same CdSe QD samples dispersed in solution^{18,23,24}. In chapter 4 we showed that while no differences are observed in absorption, the emission spectra for the QD solids are red shifted from that for the QD solutions as dipolar coupling between proximal QDs in the solids leads to electronic energy transfer within the sample inhomogeneous distributions²⁴.

Sapphire optical flats were photolithographically patterned using Shipley 1813 photoresist. 2000 Å gold was deposited on top of a 100 Å chromium adhesion layer. We used acetone to lift-off the remaining photoresist defining the electrode patterns of lines, dots, and arrows shown in Fig. 5.1(a). We also patterned the flats using a mask of interdigitated fingers. Figure 5.1(b) shows, on the left, an example of the electrode pattern of interdigitated fingers consisting of 51.5 μm wide Au/Cr fingers separated by 5 μm. The layout of the mask, shown on the right, contains patterns for the same 51.5 μm fingers with separations of 5, 10, and 20 μm. We used NR8 photoresist and lift-off with acetone to achieve a well-defined 5 μm feature size.

We also patterned a thermally oxidized, degenerately doped silicon wafer to image a QD solid deposited on a patterned oxide surface. A JEOL JSM 6320FV high

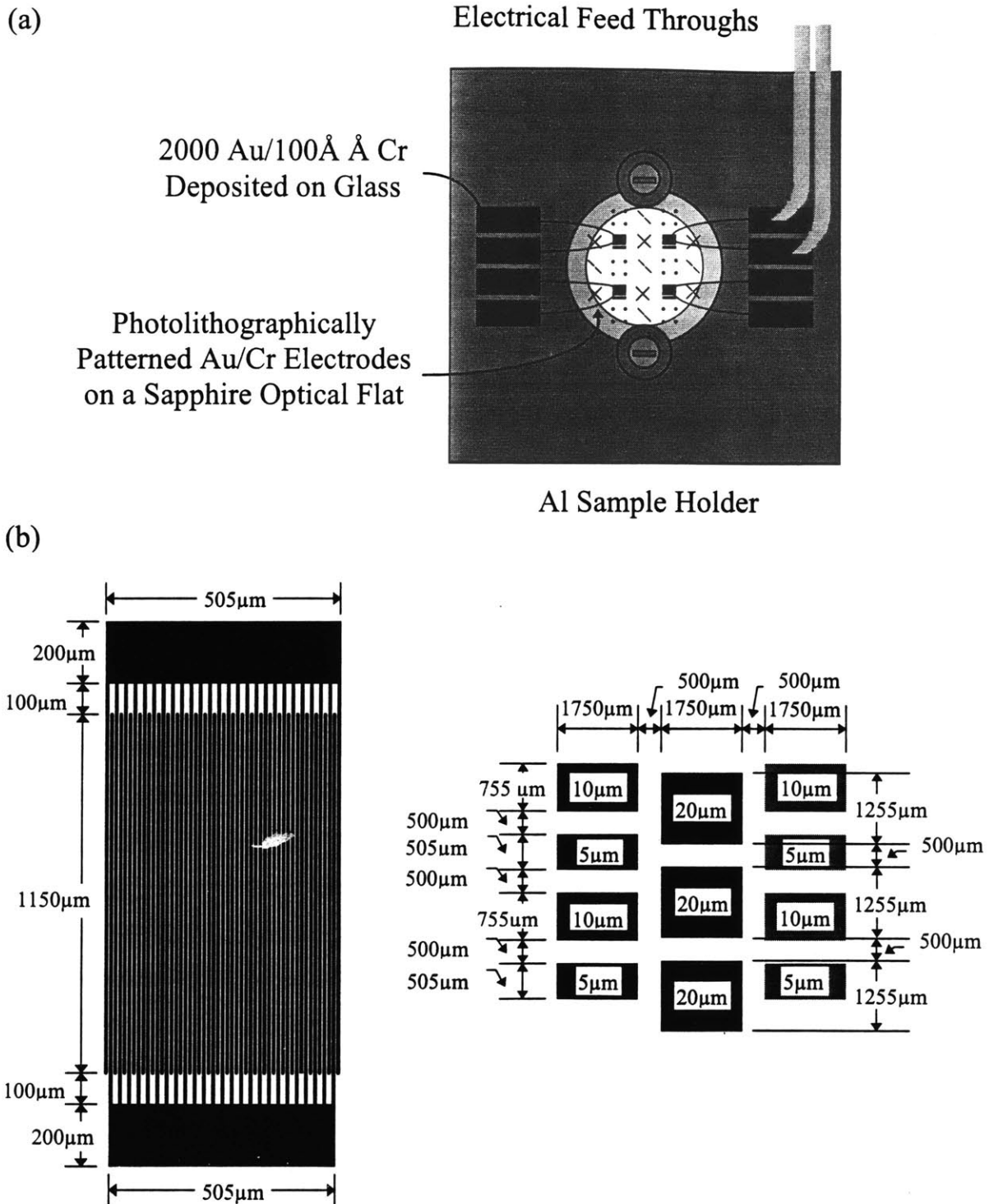


Figure 5.1 (a) Sample design for photoconductive measurements of CdSe QD solids. A sapphire optical flat was photolithographically patterned with bars, dots, and arrows; seated into an Al sample holder; and mounted on cryostat cold finger. The electrodes were wired to pads for electrical connection external to the cryostat. (b) Interdigitated electrodes with 51 $5 \mu\text{m}$ fingers separated by $5 \mu\text{m}$ (left). Mask layout (right) with sets of interdigitated electrodes as shown on left, but with 5, 10, and 20 μm spacings.

resolution scanning electron microscope (HRSEM) operated at 30 kV was used to detect secondary electron emission from the CdSe QD solid.

To make photoconductive measurements, the patterned optical flats were seated into aluminum sample holders and held in place by two sets of screws and washers [Fig. 5.1(a)]. A small amount of cryogenic epoxy was applied around the edges of the sapphire flats to ensure good thermal conductivity between the sample holders and the sapphire flats. In all of our photoconductive measurements we used the two bar electrodes 200 μm in width by 800 μm in length separated by 20 μm . A gold ball bonder was used to electrically connect the patterned electrodes to sets of pads prepared by depositing 2000 \AA gold/100 \AA chromium on pieces of glass. The pads were stuck to the sample holder using thick layers of cryogenic epoxy. The samples were mounted in a helium cryostat. Electrical feed throughs were soldered to a set of the pads to make electrical connection between the sample and vacuum BNC connections on the outside head of the cryostat. The electrical feed throughs were striped, copper braided BNC cables which minimize noise from static charge generation and electrostatic coupling. The QD solids were deposited on the patterned sapphire flats after all the electrical connections were made and the sample was mounted onto the cryostat cold finger to limit damage to the QD solid by exposure to air and to excess heat when making electrical connections.

A Keithley 6517 electrometer was electrically connected to the two BNC connections on the cryostat. The electrometer both sourced voltage and measured current. The electrical connections are shown in Fig. 5.2. The electrometer and the cryostat were both connected to common ground. All electrical cables were electrostatically shielded in braided copper. The electrometer was controlled by a computer to collect I-V curves.

We used two different configurations to photoexcite our samples. The laser setup in Fig. 5.3 was used to control the area of the spot illuminating the samples and to vary the intensity of illumination. A 6W cw Argon ion laser pumped a dye laser to produce a tunable excitation source. A neutral density wheel linearly graded from a neutral density of 0 to 2 was used to control the intensity of the excitation beam over two orders of

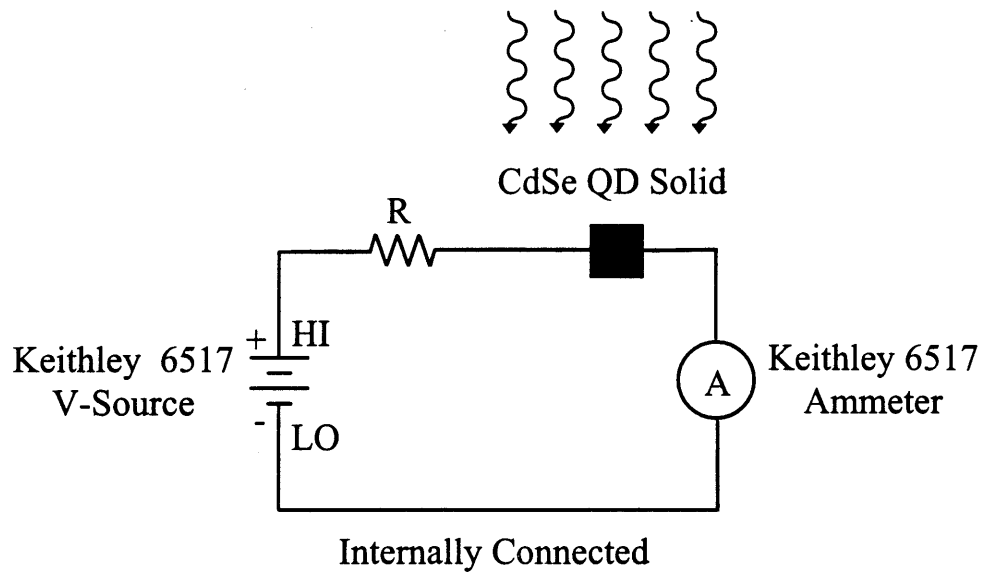
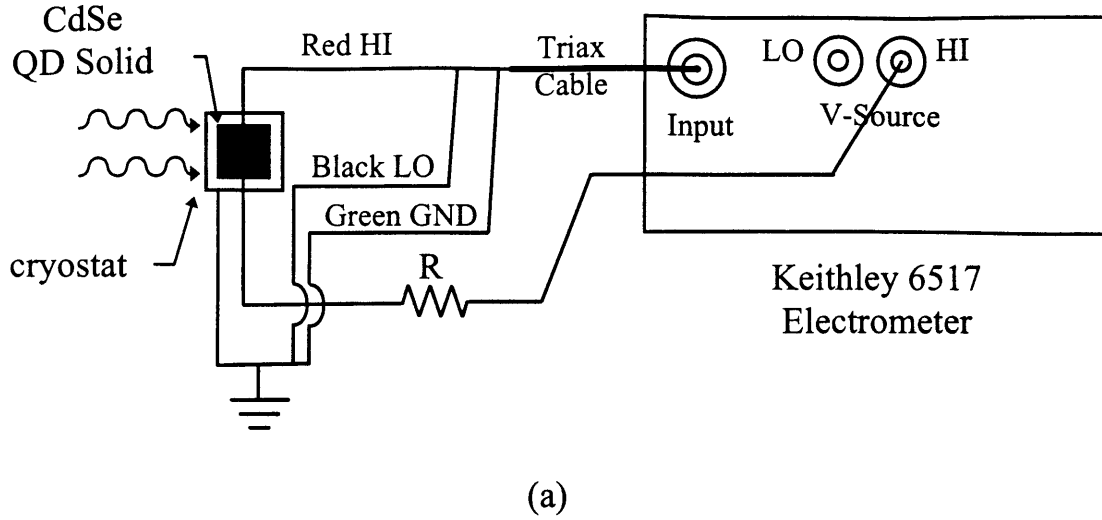


Figure 5.2 (a) Electrical connections between the CdSe QD solid under test and the Keithley 6517 electrometer. The electrometer both sources voltage and measures current to generate I-V curves for the CdSe QD solid which is illuminated. (b) Equivalent circuit diagram for the electrical connections made. Note that the Ammeter low is connected to the V-Source low internally in the electrometer.

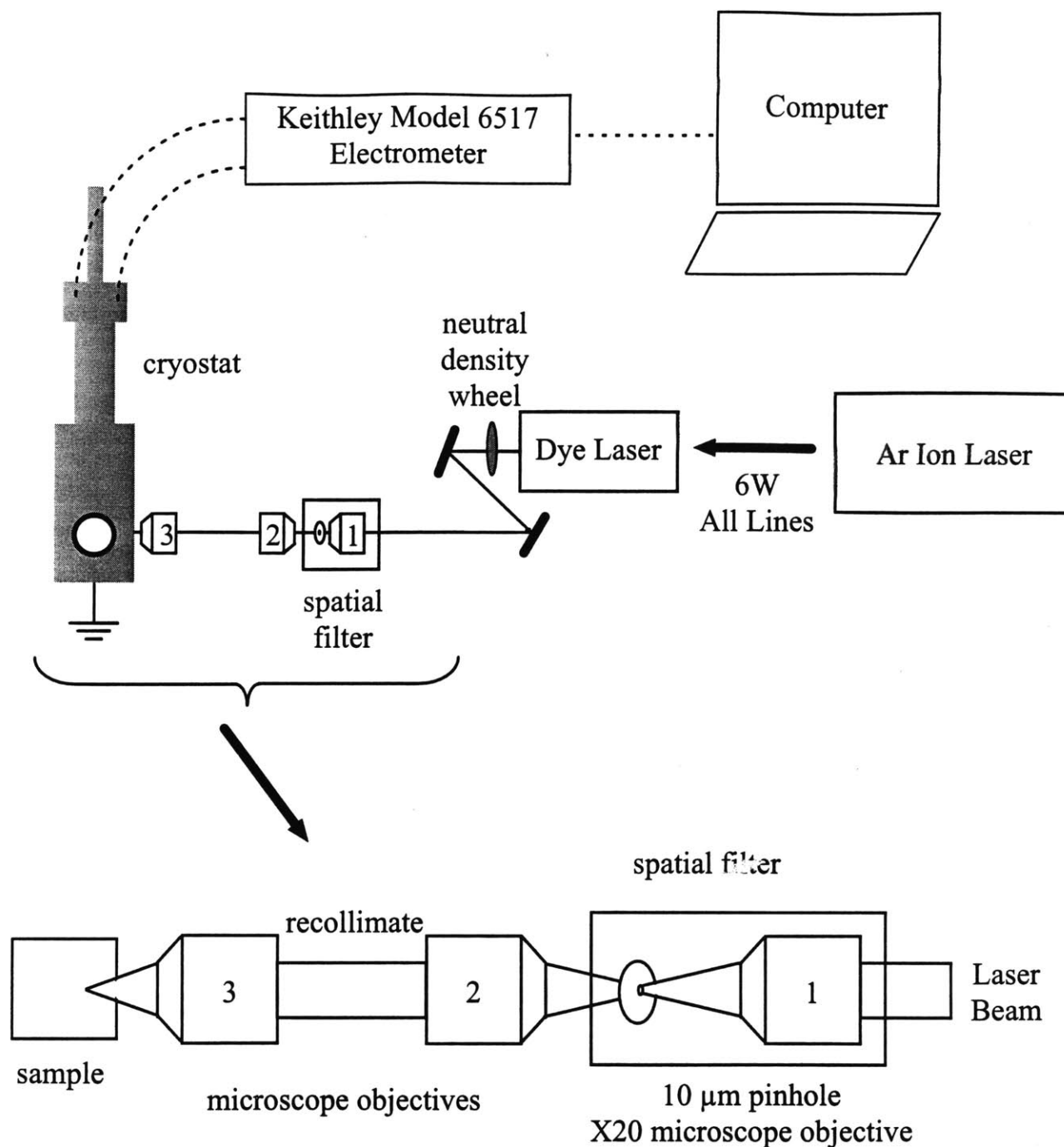


Figure 5.3 Laser setup used to measure photoconductivity in close packed CdSe QD solids. The cw Ar-ion/dye laser is used to tune the excitation energy in order to measure the spectral response of the photocurrent. System of microscope objectives enables the spatially filtered beam to be focused to a minimum spot size of $\sim 10 \mu\text{m}$. The computer controlled electrometer is used to both source voltage and measure current generating the I-V characteristics of the sample.

magnitude. A 20X microscope objective, labeled 1, in combination with a 10 μm pinhole was used to spatially filter the beam. The second microscope objective recollimated the beam and the third microscope objective focused the beam onto the sample. The system of microscope objectives was chosen to obtain a focused spot of ~ 10 μm diameter on the sample. Laser powers of ~ 25 mW could be focused onto the sample. Monitoring the transmission of the beam from behind the cryostat we positioned the cryostat so the spot illuminated the sample between the two gold electrodes. This was done to eliminate any effects of charge injection from the electrodes into the QD solid, especially in the red tail of the first exciton where the QDs weakly absorb light. The micrometer on the dye laser was calibrated for each batch of dye to the lasing energy of the dye over its range of tunability. The energy of the beam was measured by scattering it off a scatterer, dispersing it through a 0.33 m monochromator, and separating its colors using a 150 groove/mm grating. The spectra were detected by an optical multichannel analyzer. The energy dependence of the light intensity was measured using a calibrated high speed silicon photodiode connected to a digital oscilloscope.

We also used the SPEX Fluorolog-2 spectrofluorometer as our excitation source. The spectrofluorometer has a 450W Hg-Xe arc lamp and 0.22 m double excitation monochromator enabling us to measure the spectral response of the QD solids over a wide range of excitation energies. The energy dependence of the lamp intensity was measured by a reference current from a photomultiplier tube generated by emission from a concentrated dye solution. We used a Rhodamine 610 reference to correct the spectral responses for I-V curves collected for excitation energies to the blue of 2.072 eV (600 nm) and Rhodamine 640 for excitation energies to the blue of 1.973 eV (630 nm). The spectral response was further corrected by creating excitation correction factors for each of the dyes to account for the $\sim 10\%$ error resulting from the difference in optical path from the positions of the reference dye cell and the sample. The area of photoexcitation, defined by the slit in the excitation monochromator, was 1 mm wide by 1 cm in height, illuminating both the active region of the sample and the electrodes. The sample was positioned in the focal plane of the light by maximizing the measured photocurrent. The incident intensity was controlled by entrance and exit slits on the excitation

monochromator. The illumination intensity was recorded and correlated to the slits micrometers and the measured reference current for 6 different wavelengths using a calibrated power meter. Slits of ~ 2.5 mm (~ 16.5 meV bandwidth) giving a photon flux of $\sim 10^{16} \frac{\text{photons}}{\text{cm}^2 \cdot \text{sec}}$ produced photocurrents on the order of 10's of pA, sufficiently larger than the ~ 1 pA noise level seen by the electrometer.

The SPEX Fluorolog-2 spectrofluorometer was also used to measure PL spectra with and without a field applied to the QD solid. We masked the slit in the excitation monochromator to photoexcite an area just larger than a set of interdigitated electrodes patterned on an optical flat. We used the set of interdigitated electrodes defined by the mask in Figure 5.1(b) that had 20 μm separations between fingers to maximize the fraction of the QDs affected by the field.

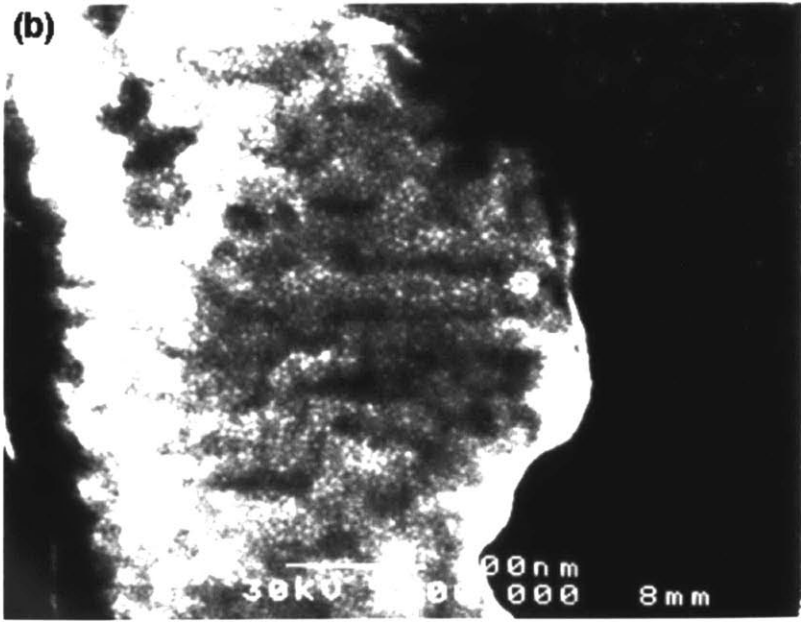
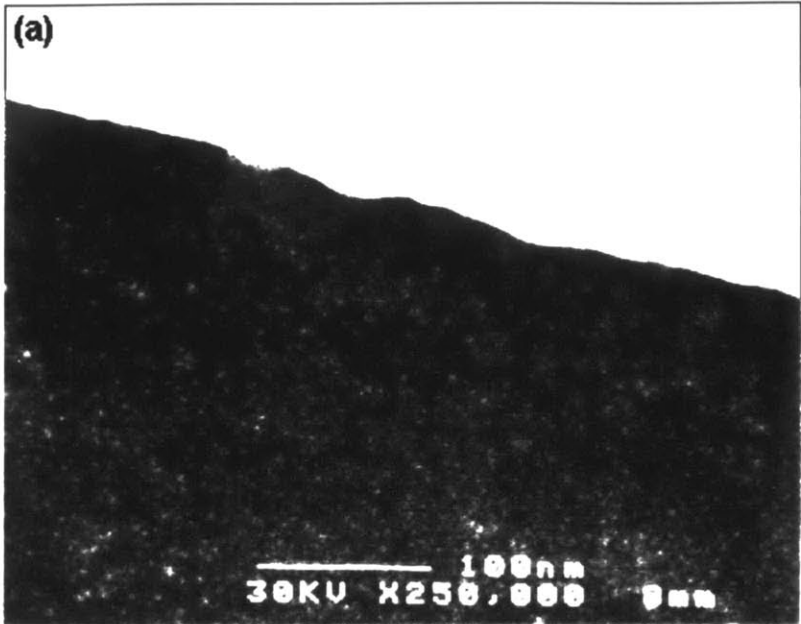
Optical absorption spectra were collected using either a 300W Hg-Xe arc lamp or a 100 W quartz-tungsten-halogen lamp. The Hg-Xe lamp in combination with a monochromator was used as the excitation source in cw photoluminescence (PL) measurements. The transmitted or emitted light was dispersed through a 0.33 m monochromator and the colors separated by a 150 groove/mm grating. The spectra were detected by an optical multichannel analyzer.

5.3 Results

5.3.1 Structural Characterization of the QD Solid/Electrodes

We use the HRSEM to image a 57 \AA CdSe QD solid deposited on a photolithographically patterned, thermally oxidized, degenerately doped silicon wafer. Figure 5.4(a) shows the QDs form a close packed solid on the oxide surface up to the oxide/metal interface. Focusing on top of the electrodes, Figure 5.4(b) shows the QDs also form a close packed solid on the surface of the gold electrodes. The QDs form a continuous, close packed solid across the surfaces of the metal electrodes and the oxide substrate. We also see the lift-off process using the Shipley 1813 photoresist causes the

Figure 5.4 57 Å CdSe QD solid deposited on a thermally oxidized, degenerately doped silicon wafer photolithographically patterned with 2000 Å Au/100 Å Cr electrodes. (a) The close packed QD solid deposited on the oxide surface remains continuous up to the metal/oxide interface. (b) The QDs form a close packed solid on the surface fo the Au electrodes. The effects of the lift-off process are seen to cause the Au electrodes to fold over on themselves.



edges of the gold electrodes to fold over on itself. To achieve the smaller feature size for the interdigitated electrodes, we used the NR8 photoresist which reduced the variation in the edges of the electrodes to $<0.5 \mu\text{m}$.

5.3.2 Voltage Dependence of Photocurrent

Figure 5.5(a) shows the I-V characteristics at 10 K for a 42 \AA CdSe QD solid illuminated by 2.272 eV (547 nm) light. The dashed line shows the I-V curve for a spot size of $\sim 10 \mu\text{m}$ illuminating the QD solid between the two gold electrodes. Defocusing the spot so the beam illuminates a region of $\sim 100 \mu\text{m}$ containing a portion of the electrodes, shows similar I-V characteristics. Further defocusing the beam results in a similar I-V curve only decreased in the measured photocurrent as the reduced photon flux decreases the number of photoexcitations generated in the active region of the QD solid. All of our measurements show nonlinear I-V characteristics, independent of excitation energy, temperature, and excitation intensity. The I-V curves are symmetric with respect to the polarity of the applied voltage since the pair of Au electrodes are indistinguishable. Collecting I-V curves by sourcing the voltage from negative to positive polarities and vis-versa showed no differences in the collected I-V curves (no signs of hysteresis). Tuning the excitation energy to the red of the QD absorptions showed no generated photocurrents, eliminating any significant carrier injection from the electrodes into the QD solids. Once we established that optically exciting the electrodes did not lead to carrier photoinjection from the electrodes into the QD solids, all measurements were collected by illuminating larger areas including both the active area of the QD solids and the electrodes.

5.3.3 Spectral Response of Photocurrent

Figures 5.6(a), 5.7(a), and 5.8(a) show 3D plots of the I-V curves collected at 10K as a function of excitation energy for QD solids prepared from CdSe QDs 30.3, 41.4, and 49.5 \AA in diameter, respectively. Figures 5.6(b), 5.7(b), and 5.8(b) plot the measured

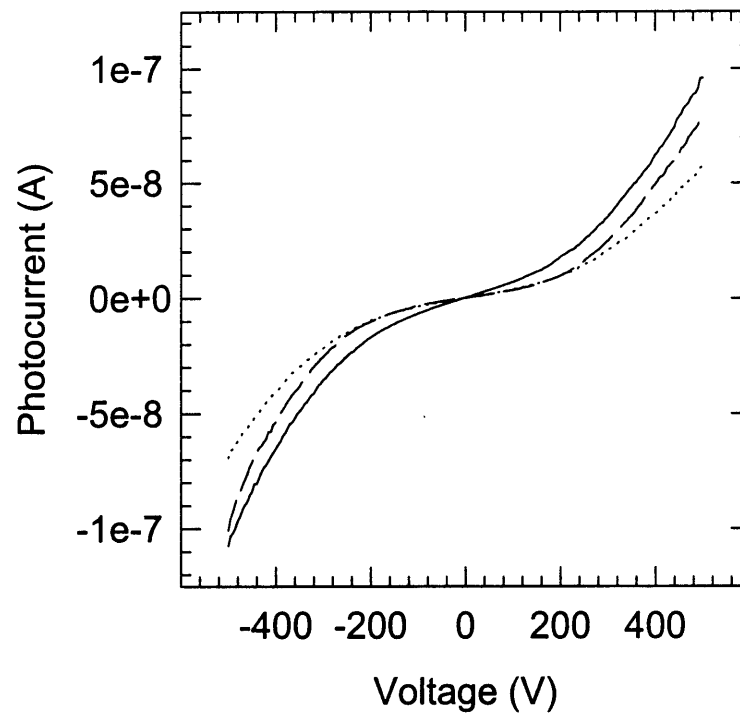


Figure 5.5 Comparison of the I-V curves for a beam spot focused to $\sim 10 \mu\text{m}$ on a 42 \AA CdSe QD solid between the Au electrodes (dashed line) with that for the beam defocused to $\sim 100 \mu\text{m}$ illuminating both the electrodes and the QD solid. Both I-V curves reveal the nonlinear behavior of the current characteristic of all the I-V curves measured for any QD solid. Further defocusing the beam just reduces the measured photocurrent as the photon flux is reduced (dotted line).

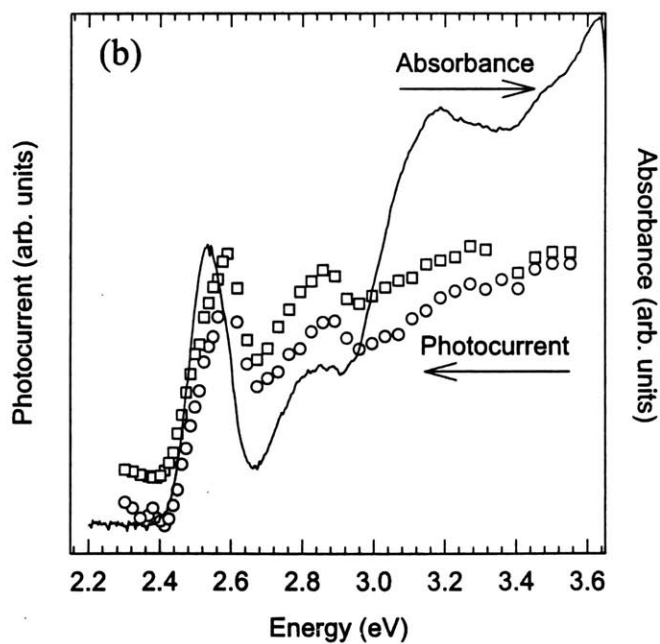
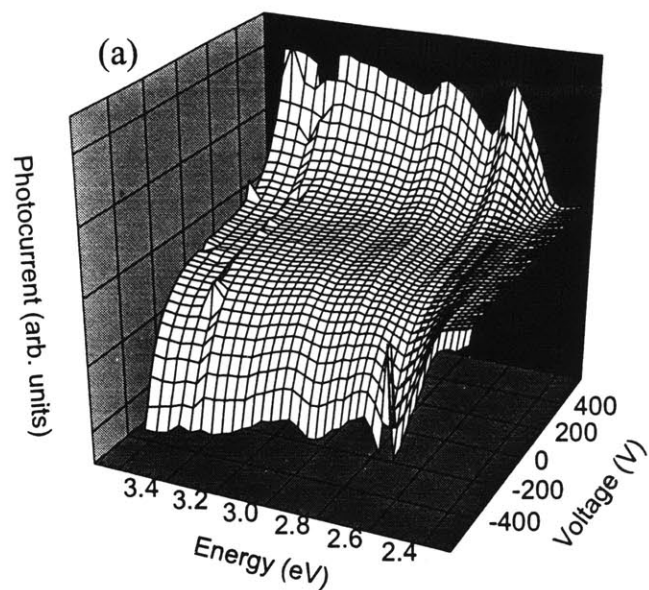


Figure 5.6 (a) I-V curves collected as a function of excitation energy for a 30.3 Å diameter CdSe QD solid. (b) Spectral response of photoconductivity plotting the photocurrents at applied voltages of -500V (circle) and +500V (square).

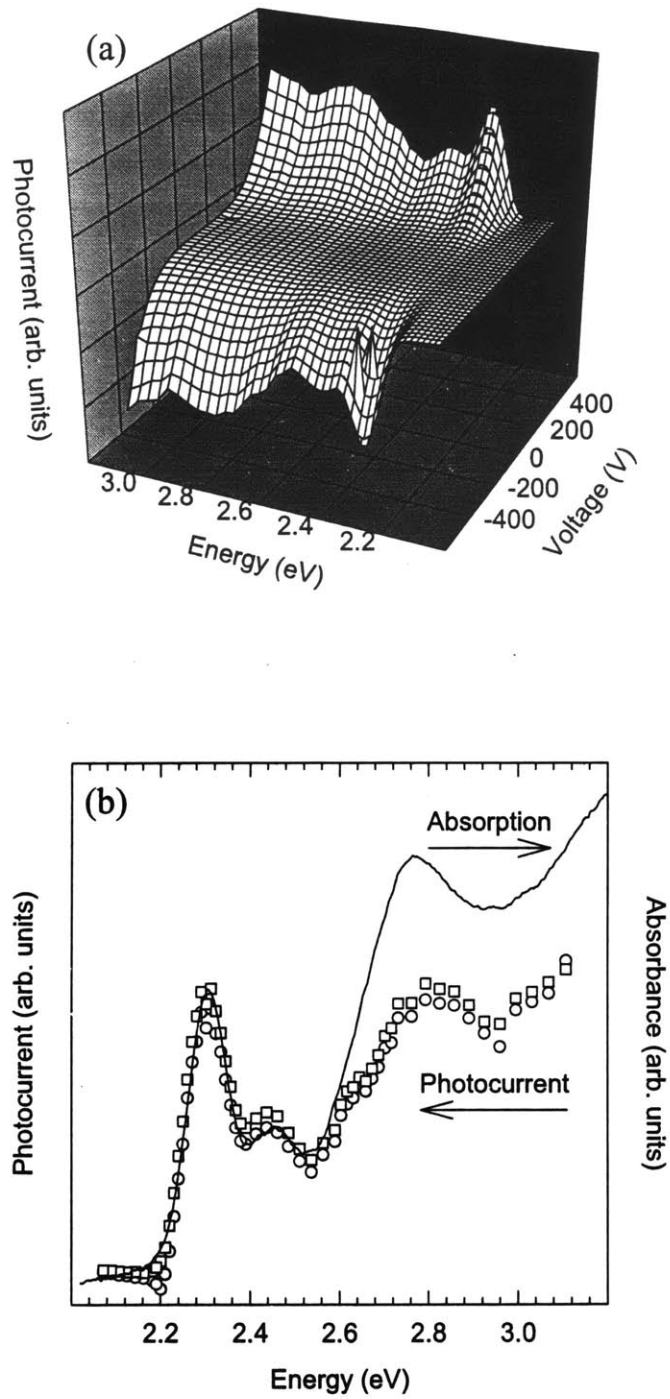


Figure 5.7 (a) I-V curves collected as a function of excitation energy for a 41.4 Å diameter CdSe QD solid. (b) Spectral response of photoconductivity plotting the photocurrents at applied voltages of -500V (circle) and +500V (square).

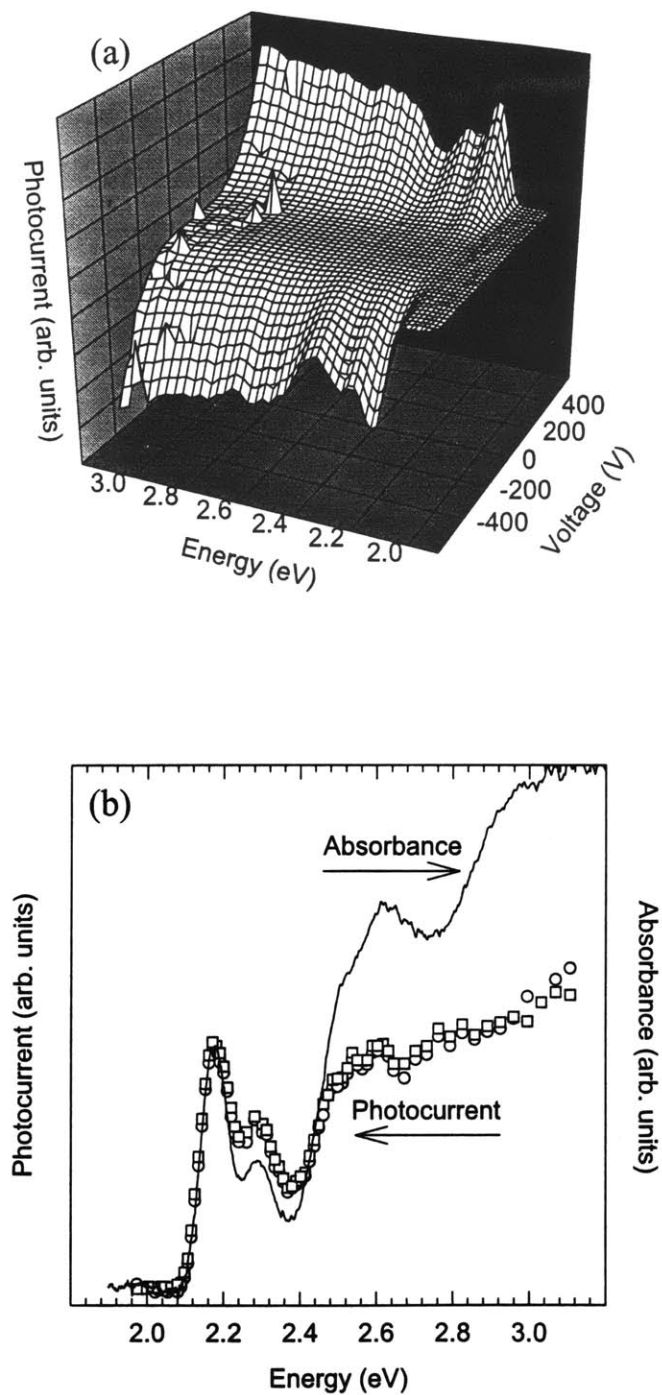


Figure 5.8 (a) I-V curves collected as a function of excitation energy for a 49.5 Å diameter CdSe QD solid. (b) Spectral response of photoconductivity plotting the photocurrents at applied volages of -500V (circle) and +500V (square).

photocurrents at -500 V (open circles) and +500 V (open squares) in comparison with the 10 K absorption spectra (solid lines) for each of the QD solids. The absorption spectra were collected from regions of the sample to the side of the electrodes used for photoconductive measurements and between the other sets of electrodes on the flats. The spectral response of the photocurrent follows the structure of discrete electronic transitions measured in absorption for the QD solids. In the blue, the photocurrent for each of the QD solids shows a decrease in magnitude relative to the redder excitation energies. We arbitrarily chose to plot the spectral response at applied voltages of +/-500 V, but in general the spectral response is independent of the applied voltage.

The spectral response of the photocurrent for the 30.3 Å CdSe QD solid does show a blue shift in the peak position of the photocurrent relative to its absorption spectrum. It also shows a larger difference in the photocurrents measured at positive and negative polarities after the first three points taken at the bluest excitation energies. It is possible that the film deteriorated in the presence of light and the applied electric field as the smallest QDs in general have the greatest instabilities.

5.3.4 Intensity Dependence of Photocurrent

I-V curves collected at 10 K as a function of incident intensity (I_0) for a 42 Å CdSe QD solid [Fig. 5.9(a)] show that the generated photocurrent increases with increasing photon flux. Scaling these I-V curves, inset in Figure 5.9(a), shows that the nonlinear shape of the I-V characteristics is independent of incident intensity. Plotting the I-V curves in 3D as a function of the relative intensity of the incident beam [Fig. 5.9(b)] shows that the photocurrent is linear in incident intensity for all non-zero applied voltages. Fitting the intensity dependence for applied voltages between -500 V and 500 V in steps of 100 V by $I \propto I_0^n$ yielded a value for n of 1.05 ± 0.02 . In the dark, we cannot measure any current for the QD solids above the noise level (~ 1 pA) seen by the electrometer. The I-V curve is shown by the flat line along the current axis in Fig. 5.9(a). This sets a lower bound for the resistivity of the QD solid in the dark at $40 \text{ G}\Omega \text{ cm}^{-1}$.

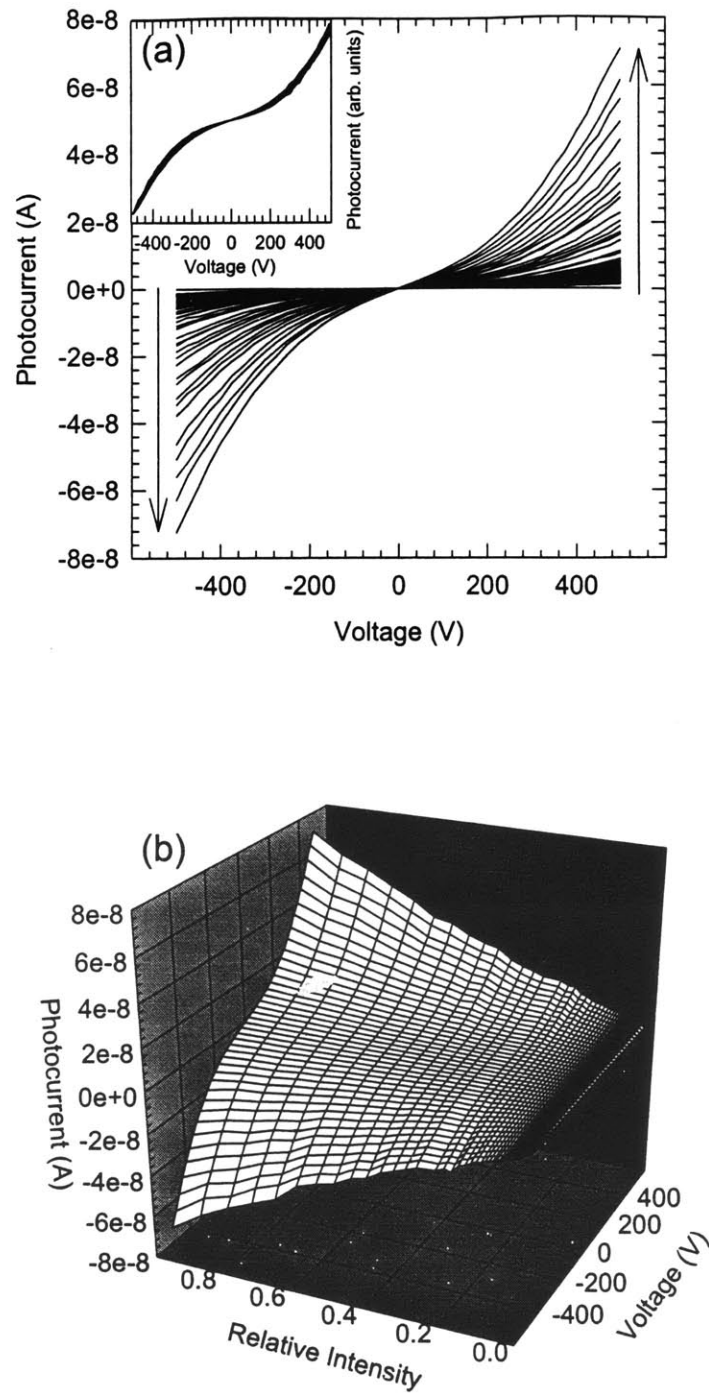


Figure 5.9 (a) I-V curves taken as a function of incident intensity to demonstrate the increase in generated photocurrent with increasing intensity. The inset shows the I-V curves have the same shape and are simply scaled by the relative intensity of the incident beam. (b) Plotting the I-V curves versus relative intensity reveals that the generated photocurrent is linearly proportional to the incident intensity for each applied voltage.

5.3.5 Temperature Dependence of Photocurrent

Figure 5.10(a) plots the temperature dependence of the I-V characteristics from 10 K to 200 K for the 41.4 Å CdSe QD solid shown in Figure 5.7. The QD solid was photoexcited with an energy of 2.302 eV (540 nm), the energy of the peak of the first exciton at 10 K. The photocurrent first increases up to 75 K and then decreases with increasing temperature. The I-V curve also changes shape at a temperature of 100 K [Fig. 5.10(b)] where the photocurrent begins decreasing. In Figure 5.11 we map the photocurrent at voltages of (A) +/-500 V, (B) +/-400 V, (C) +/-300 V, and (D) +/-200 V where the filled circles (squares) plot the negative (positive) polarity in applied voltage. Below applied voltages of +/-200 V the photocurrents are too small relative to the noise level of the electrometer to see any trends with temperature. The maximum photocurrent shifts from 50 K at +/-500 V, to 75 K at +/-400 V and +/-300 V, and to 100 K at +/-200 V.

In Figure 5.12(a) we also plot the temperature dependence of the I-V curves for the 49.5 Å CdSe QD solid shown in Figure 5.8. We collected the I-V curves for temperature cycles up from 10 K to 150 K and back from 150 K to 10 K, over the temperature range in which we observe the maximum in photocurrent. Figure 5.12(b) shows that the I-V curves are reproducible with temperature cycling and the I-V curve again changes shape at 100 K where the photocurrent begins to decrease. We plot in Figure 5.13 the photocurrent at voltages of (A) +/-500 V, (B) +/-400 V, (C) +/-300 V, and (D) +/-200 V where the filled circles (squares) plot the negative (positive) polarity in applied voltages with the temperature cycle up filled in black and the temperature cycle down filled in gray. The I-V curves again show a voltage dependent maximum in the temperature dependence of the photocurrent from 75K at +/-500 V to +/-300 V to 100 K at +/-200 K.

In Figure 5.14(a, b) we show the temperature dependence of the I-V curves for the 30.3 Å CdSe QD solid photoexcited at 2.590 eV (480 nm). The photocurrent shows a simple increase with increasing temperature, but as we saw in the spectral response of the photocurrent some damage to the QD solid may have occurred while collecting the I-V

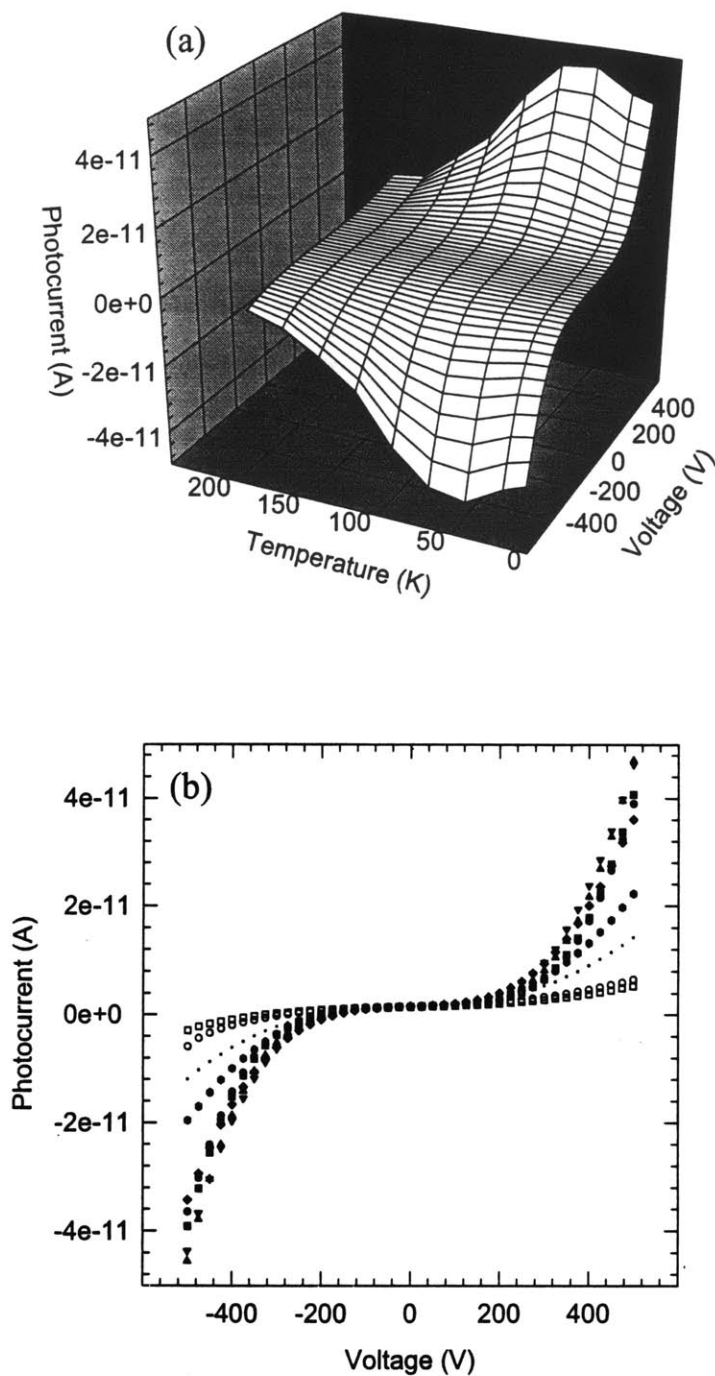


Figure 5.10 (a) I-V curves collected as a function of temperature for a 41.4 \AA CdSe QD solid. (b) The shape of the I-V curves changes with increasing temperature most notably at 100 K. The I-V curves are shown at temperatures of 10 K (filled circles), 25 K (filled squares), 50 K (triangles pointed up), 75 K (triangles pointed down), 100 K (diamonds), 125 K (hexagons), 150 K (dots), 175 K (open circles), and 200 K (open squares).

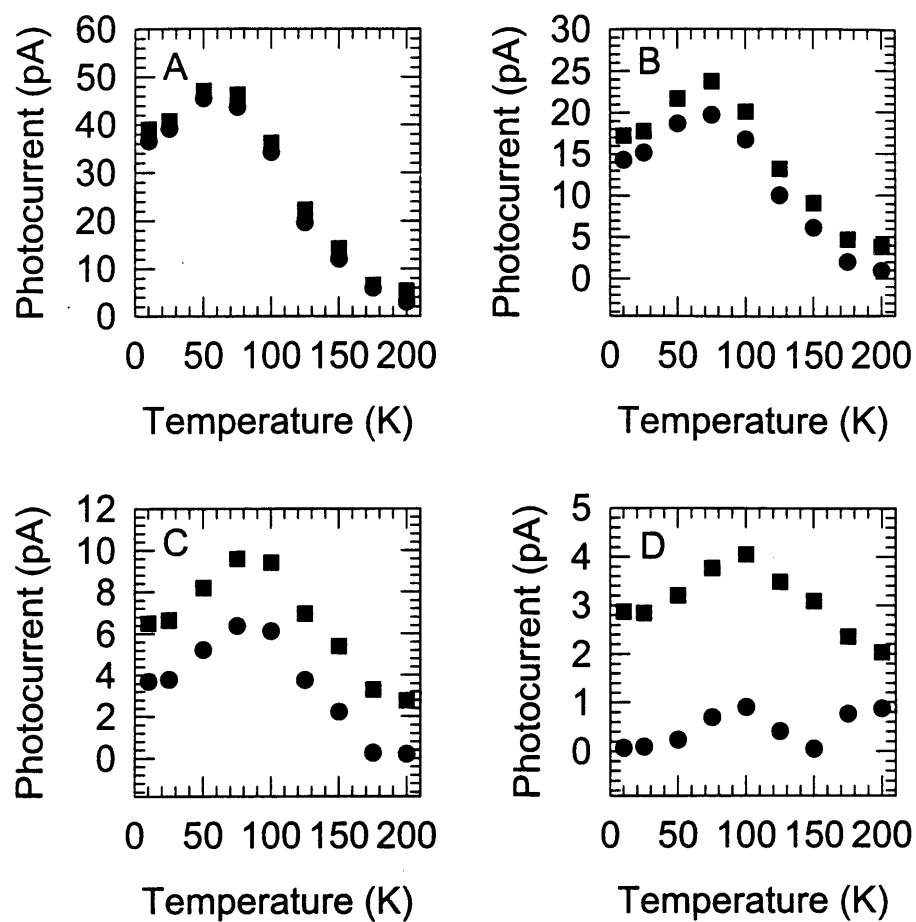


Figure 5.11 Plotting the photocurrents measured as a function of temperature for applied voltages of (A) $\pm 500\text{V}$, (B) $\pm 400\text{V}$, (C) $\pm 300\text{V}$, and (D) $\pm 200\text{V}$. As the applied voltage decreases, the maximum photocurrent shifts to higher temperatures consistent with a thermally activated process. Photocurrents for (circle) negative and (square) positive polarities in applied voltage.

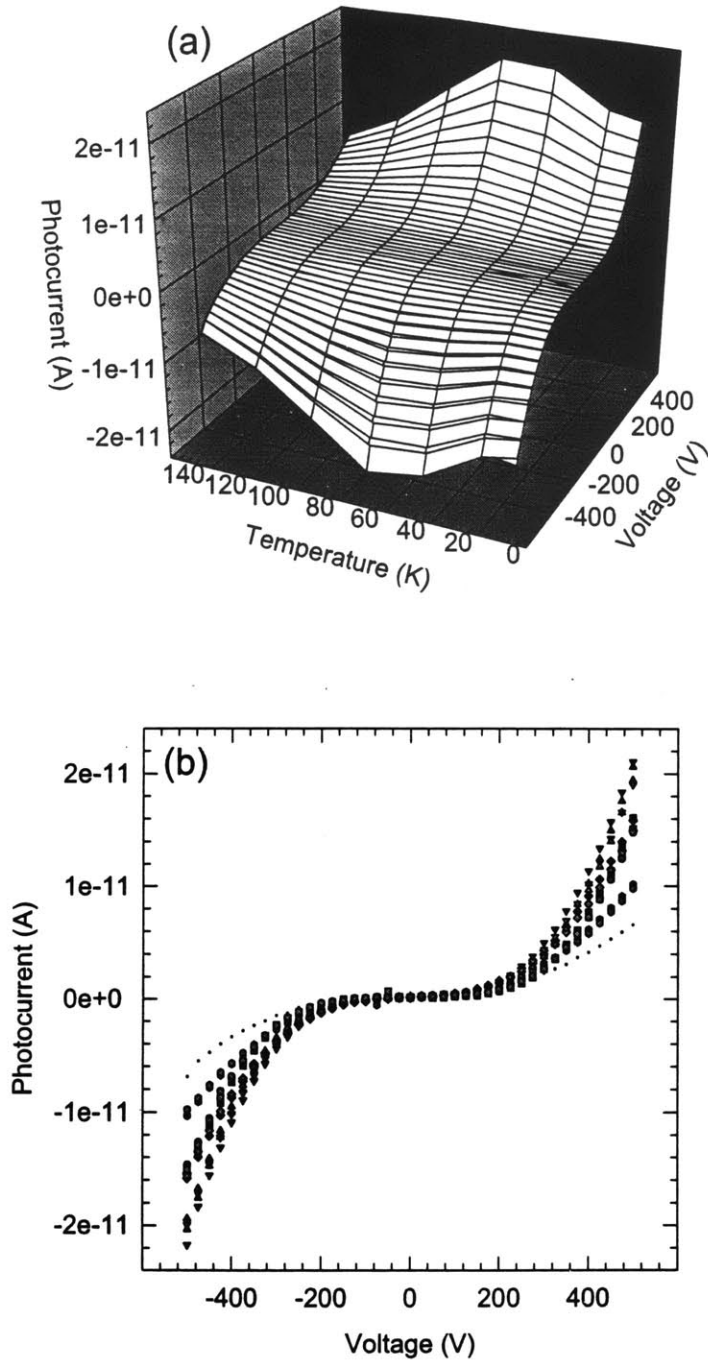


Figure 5.12 (a) I-V curves collected as a function of temperature for a 49.5 Å CdSe QD solid. (b) The shape of the I-V curves changes with increasing temperature most notably at 100 K. The I-V curves are shown at temperatures of 10 K (circles), 25 K (squares), 50 K (triangles pointed up), 75 K (triangles pointed down), 100 K (diamonds), 125 K (hexagons), and 150 K (dots). Cycling the temperature up from 10 K to 150 K (symbols filled black) and down from 150 K to 10 K (symbols filled grey) shows the changes in the I-V curves are reproducible.

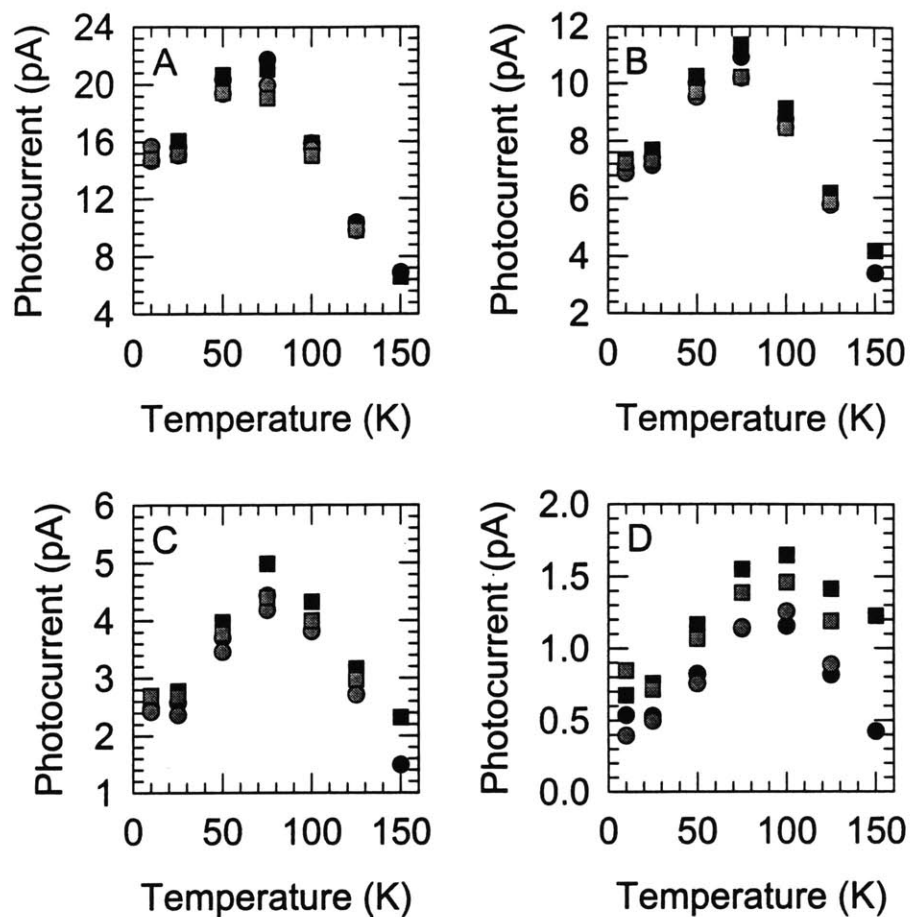


Figure 5.13 Plotting the photocurrents measured as a function of temperature for applied voltages of (A) ± 500 V, (B) ± 400 V, (C) ± 300 V, and (D) ± 200 V. As the applied voltage decreases, the maximum photocurrent shifts to higher temperatures consistent with a thermally activated process. Photocurrents for (circle) negative and (square) positive polarities in applied voltage. Cycling the temperature up from 10 K to 150 K (black) and down from 150 K to 10 K (grey).

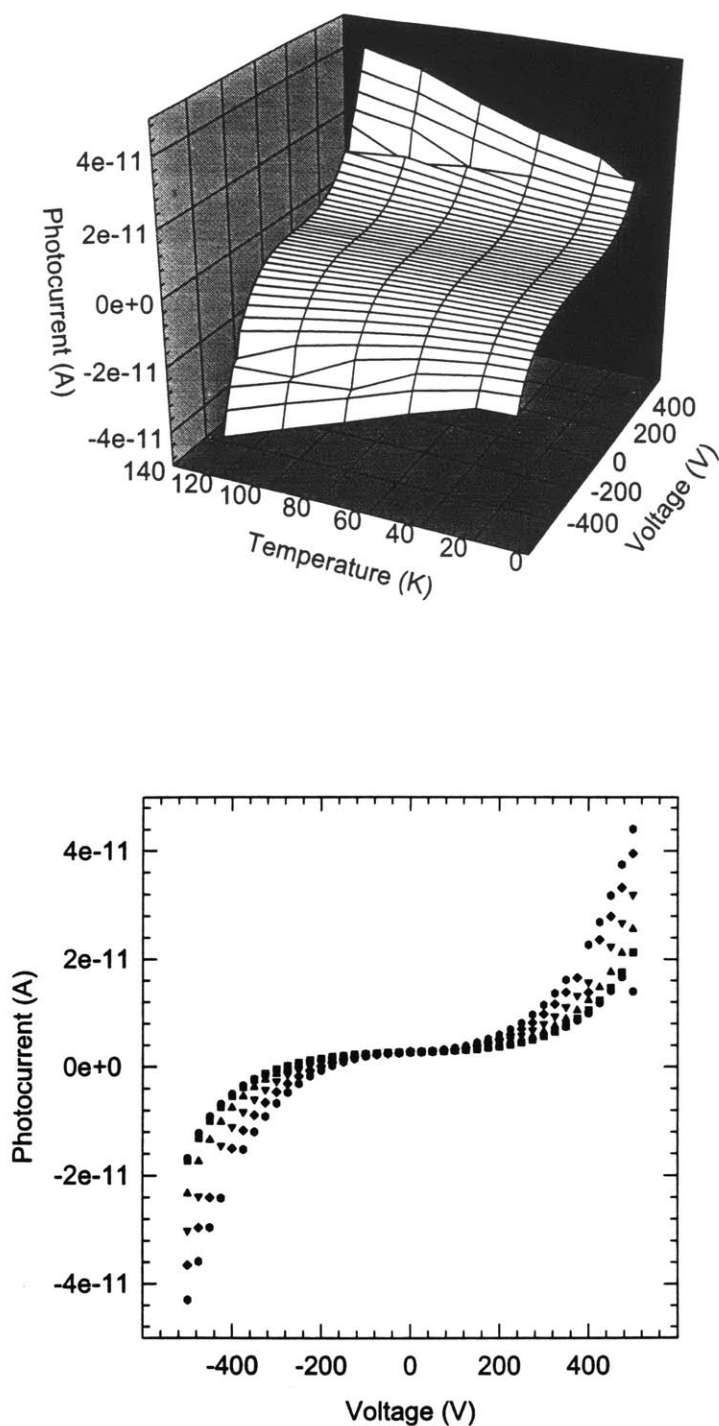


Figure 5.14 (a) I-V curves collected as a function of temperature for a 30.3 \AA CdSe QD solid. (b) The shape of the I-V curves remain unchanged as a function of temperature. The I-V curves are shown at temperatures of 10 K (filled circles), 25 K (filled squares), 50 K (triangles pointed up), 75 K (triangles pointed down), 100 K (diamonds), and 125 K (hexagons).

curves leading to the observed difference in the temperature dependence for this QD solid.

Above 200 K we could not measure I-V curves for any of the QD solids, the current would runaway irreversibly, damaging the QD solid. Previously we observed some photochemistry in QD solids at room temperature after exposure to light for about 1.5 hours. We show the room temperature effects of long term photoexcitation of the QD solid in Chapter 2. It is possible that at these higher temperatures and under the applied field degradation of the QD solid is accelerated.

5.3.6 Effects of the Electric Field on the Photoluminescence of the QD Solid

In Figure 5.15 we plot the PL spectrum for the QD solid as a function of applied field for excitation energies of (A) 2.762 eV (450 nm), (B) 2.486 eV (500 nm), (C) 2.166 eV (574 nm), and (D) 2.072 eV (600 nm). In Figures 5.15 (A-C), for excitation energies greater than or equal to the peak of the first exciton, the PL quantum yield for the QD solid decreases with applied field. In Figure 5.15(D), exciting the solid in the red tail of its absorption spectrum spectrally selects a subset of the sample inhomogeneous distribution revealing a line narrowed fluorescence spectrum showing the phonon progression characteristic of emission from individual QDs. Little change is observed in the measured quantum yield for the solid with the field applied when exciting into the red tail in absorption.

5.4 Discussion

5.4.1 Charge Generation and Separation

In Figures 5.6-5.8 we saw that for each of the QD solids the spectral response of the photocurrent has the same structure as the absorption spectrum for the QDs. This demonstrates that the QDs are responsible for carrier generation in the QD solids. The relative decrease in the magnitude of the photocurrent for bluer relative to redder

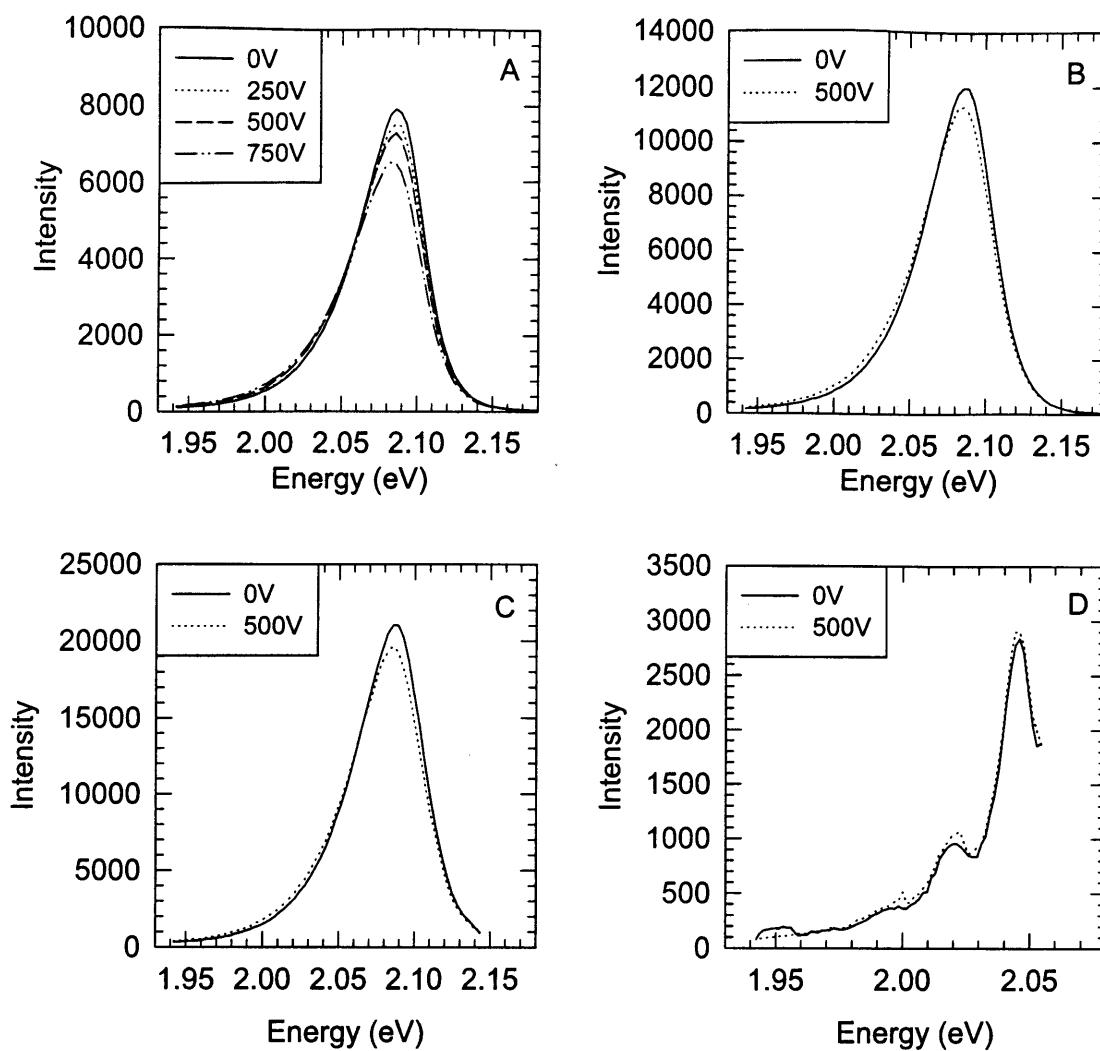


Figure 5.15 Electric field dependence of photoluminescence intensity for (A) 2.762 eV, (B) 2.486 eV, (C) 2.166 eV, and (D) 2.072 eV excitation of a 49.5 Å CdSe QD solid deposited on a set of interdigitated electrodes shown in Fig. 5.2. The effects of the applied electric field on the intensity of the photoluminescence are the same trends seen in Stark luminescence studies.

excitation energies is consistent with a measured decrease in the PL quantum yield for QDs when using bluer relative to redder excitation energies⁵⁴. This observed decrease in intensity at the bluer excitation energies is also observed across the spectrum in PLE measurements of the QDs⁸. Exciting the QDs far to the blue of the first exciton is believed to enhance the coupling of excitations into nonradiative pathways in the QDs.

The spectral responses for the QD solids also suggest that photoexcited carriers thermalize to the lowest excited state of the QDs before being separated. One would expect to see increases in the magnitude of the photocurrent as the excitation energy was tuned to the blue if hot carriers were separated before being thermalized. Similarly, PL measurements for the QDs also show no signs of hot carrier emission (i.e. no phonon bottleneck), only emission from the band edge as carriers rapidly relax from higher excited states in the QDs with times of $\sim 10^{-12}$ sec¹¹.

Photon fluxes of $10^{16} \frac{\text{photons}}{\text{cm}^2 \cdot \text{sec}}$ impinge $\sim 10^{12}$ photons/sec on the active area of the

QD solids, generating photocurrents of ~ 30 pA at applied voltages of ± 500 V. Our QD solids have thickness on the order of the penetration distance of the light. Therefore photoexcitations are created through the thickness of the QD solids. For an optical density of 0.1, the external carrier generation efficiency for the QD solids is $\sim 5 \times 10^{-4}$.

Photoexcitation of a QD generates an electron-hole pair which is confined to and delocalized over the volume of the QD. The exciton must be dissociated, separating the electron and hole, so the free carriers can be transported through the QD solid. Geminate recombination of electron-hole pairs prior to carrier separation has been shown to govern the efficiency of photocarrier generation in low mobility solids such as photoconductive polymers⁵⁵, molecular solids²⁶, intrinsic solids of C_{60}/C_{70} ⁵⁶, and some inorganic solids⁵⁷. The QD solids are similar to molecular solids in that the QDs behave like large molecules and the QD solids are weak van der Waals solids. The properties of the individual QDs are preserved in the QD solid as are molecules in many molecular solids. We show in Chapter 2 that the absorption spectra for QD solids are identical to those for QDs dispersed in solution, indicating that the interactions between QDs in the solids are weak. Excitations are localized in the individual QDs in the solids upon photoexcitation.

5.4.2 Onsager Model of Field-Assisted Charge Separation

Onsager theory for geminate recombination of ions⁵⁸, although strictly solved for classical particles, has successfully described field-assisted charge separation of electron-hole pairs in photoconductive solids. It assumes that the only forces seen by the charged pair are its mutual Coulomb attraction and the externally applied field. The Onsager radius r_c defined by

$$eV = \frac{e^2}{\epsilon r_c} = kT \Rightarrow r_c = \frac{e^2}{\epsilon kT} \quad (5.1)$$

describes the separation at which the charged pair achieves a potential energy equivalent to kT . The dimensionless parameter

$$\eta = \frac{r_c}{r_0} \quad (5.2)$$

describes r_c relative to r_0 , the initial separation of the charged pair. r_0 is also a measure of the low-field charge generation efficiency. The theory is also expressed in terms of another dimensionless parameter ζ given by

$$\zeta = \frac{eEr_0}{2kT} \quad (5.3)$$

which describes the relative strength of the applied field to kT . The probability of charge generation for a given r_0 and field strength E can be calculated from

$$P = \frac{\phi(r_0, E)}{\phi_0} = 1 - (2\zeta)^{-1} \sum_{k=0}^{\infty} A_k(\eta) A_k(2\zeta) \quad (5.4)$$

$$\text{where } A_{k+1}(\eta) = A_k(\eta) - \frac{\eta^{k+1} e^{-\eta}}{(k+1)!} \text{ and } A_0 = 1 - e^{-\eta}. \quad (5.5)$$

ϕ_0 is the quantum yield with which absorption of a photon creates a bound electron-hole pair and represents the maximum achievable charge generation efficiency approached at high fields. The field dependence of the probability of charge generation is an S-shaped curve which shifts to lower fields with increasing values of r_0 .

It is possible that the nonlinear behavior of the I-V curves is a measure of the field-dependent charge separation of photogenerated electron-hole pairs in the QDs. The Onsager model has been applied to explain carrier generation in poly(vinyl carbazole)

sensitized with 16 Å CdS QDs⁵³. The measured photocurrents are the product of the efficiency of charge separation and carrier transport through the solid, assuming no effects due to the contacts. Figure 5.16(a) is a cartoon depicting the band diagram for a CdSe QD and a Au electrode using the electron affinity ($\chi = 4.4 \text{ eV}^{59}$) and band gap ($E_g = 2.2 \text{ eV}$) measured by Lee for the QD and the work function ($\phi = 5.2 \text{ eV}^{60}$) for Au. The electrodes should not inject charge into the QD solid and from a simple bulk picture ($\phi_{\text{Au}} < \phi_{\text{CdSe}}$), assuming the QD is intrinsic, the electrode should make an ohmic contact to the QDs. Applying a voltage across the QD solid between two Au electrodes leads to a voltage drop across each of the QDs [Fig. 5.16(b, c)]. An electron (hole) generated in a QD may be simply swept by the field, hopping down (up) a staircase of QDs to the gold electrodes. So it is possible that the hard step is charge separation and the nonlinear behavior of our I-V curves may represent the field dependence of charge separation.

In Figure 5.17 we plot the measured photocurrent for the 49.5 Å CdSe QD solid at 10 K (solid line) versus the applied field $E = \frac{V}{\epsilon_{\text{avg}} d}$ where ϵ_{avg} is the volume weighted average of that for the organic cap ($\epsilon \sim 3$) and the CdSe QD ($\epsilon = 10$) and d is the 20 μm electrode spacing across which the voltage V is applied. Calculating the probability of charge generation for $r_0 = 62 \text{ \AA}$ reproduces the nonlinear shape of the photocurrent versus field over the range of fields applied to the QD solid. Going to higher fields leads to breakdown of the QD solid, eliminating the opportunity to see any saturation in the carrier generation efficiency at higher fields. Also shown is the photocurrent versus applied field for the 41.4 Å CdSe QD solid at 10 K and the Onsager model for $r_0 = 57 \text{ \AA}$. It may be expected that r_0 will increase with QD size and the nearest neighbor distance in the solids. Increasing the size of the QD decreases the overlap of the electron and hole wavefunctions, potentially making charge separation easier. This is seen as the upturn in the I-V curves shifts to lower voltages as does the Onsager model for larger values of r_0 . The charge generation efficiency at a given applied voltage increases as the size of the QD in the solid increases.

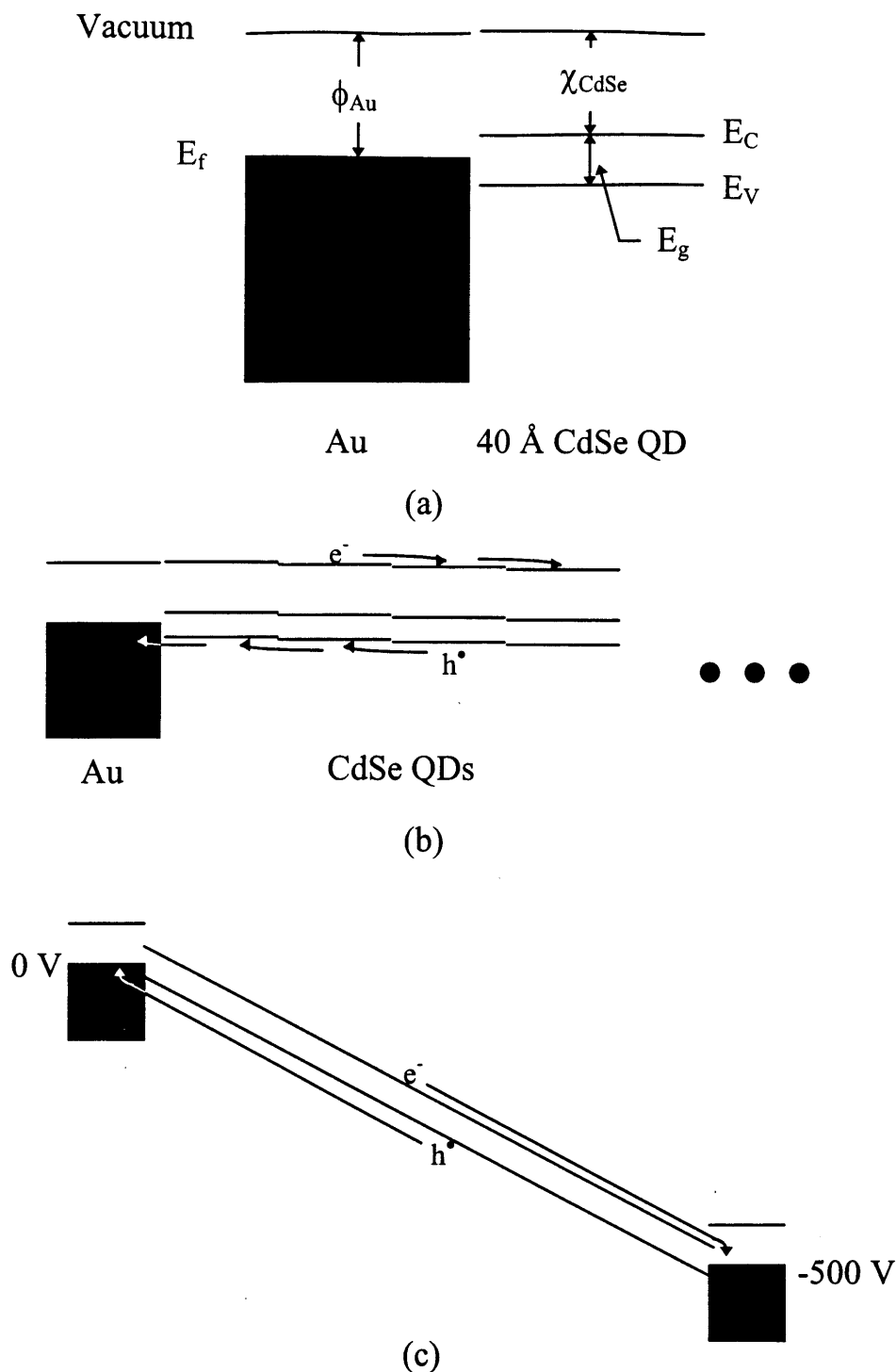


Figure 5.16 (a) Band lineup for Au electrode with a work function $\phi_{Au} = 5.2$ eV and for a 40 Å CdSe QD with an effective energy gap $E_g = 2.2$ eV and an electron affinity $\chi_{CdSe} = 4.4$ eV. (b) Staircase of QDs under an applied electric field. (c) Zooming out so the staircase of QDs appears as a slope for its conduction and valence bands since there are ~ 4000 40 Å QDs, allowing for a 10 Å organic spacer, between electrodes separated by 20 μm .

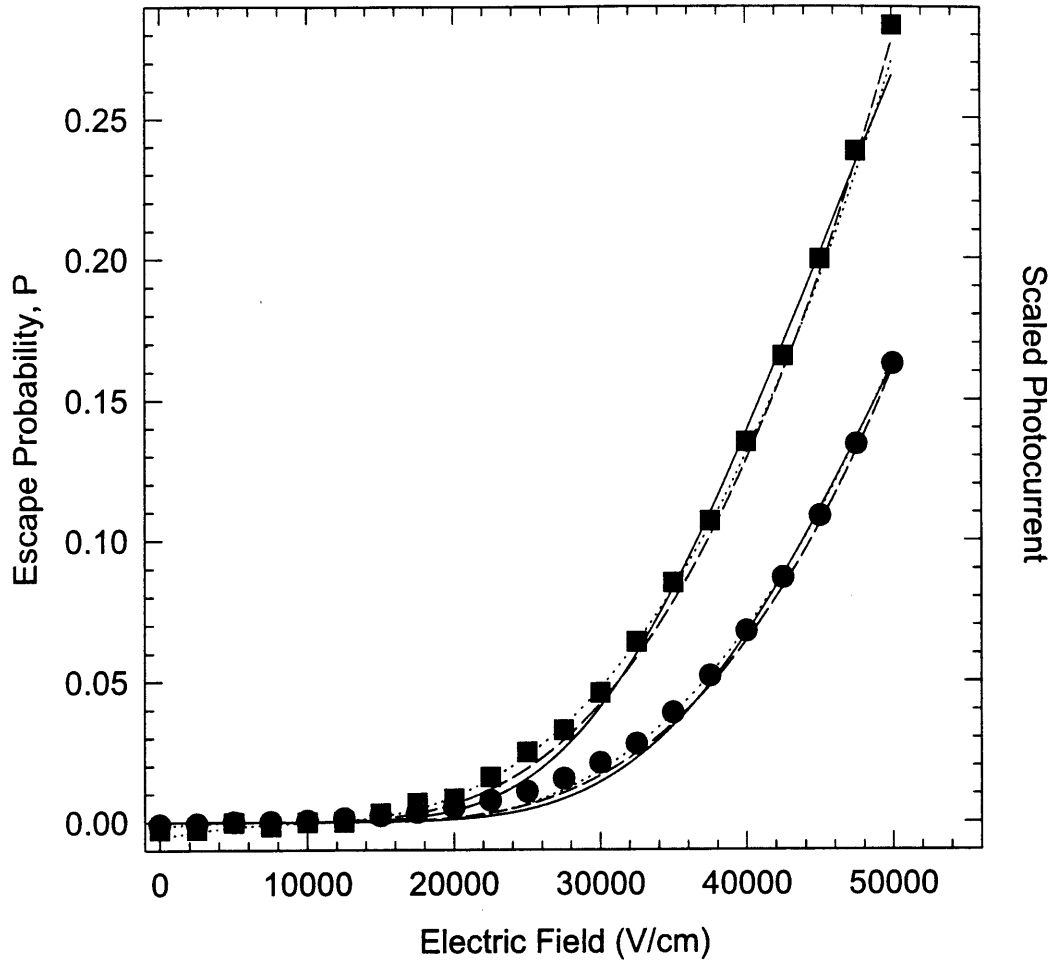


Figure 5.17 Electric field dependence of the photocurrent for the 41.4 Å (circles) and 49.5 Å (squares) CdSe QD solids. Solid lines plot the Onsager model escape probability as a function of electric field for values of r_0 equal to 57 Å (along circles) and 62 Å (along squares). Dotted lines plot the scaling law for an exponent ζ of 2.6 with voltage thresholds of 150 V (along circles) and 90 V (along squares). The scaling law and measured photocurrent is scaled to and expressed in terms of the electric field for comparison to the Onsager model. Dashed lines plot the Fowler-Nordheim tunneling current for values of β equal to $9.5 \times 10^6 \text{ cm/V}$ (along circles) and $6.5 \times 10^6 \text{ cm/V}$ (along squares).

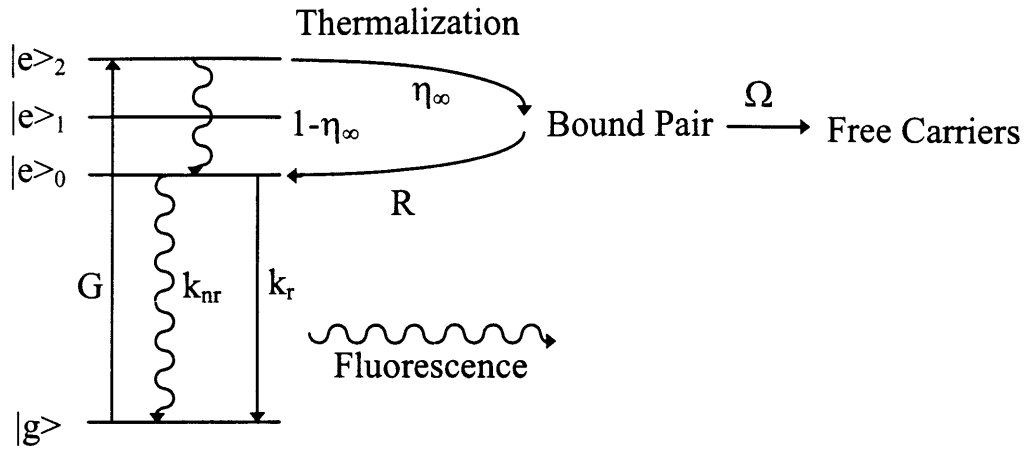
The Onsager model [Fig. 5.18(a)] for the initial recombination of a charged pair describes the escape of a carrier from the excited state to which the carrier was photoexcited. The excess energy of the carrier is assumed to be lost upon collisions with the medium, after which the carrier has traveled a thermalization length from its oppositely charged carrier and can be separated and transported through the medium. The Onsager model describes an energy-dependent charge generation efficiency where higher energy photoexcitation leads to larger values of r_0 .

For organic photoconductors, the charge generation efficiency is independent of the energy of photoexcitation. Internal conversion from higher excited states to the lowest excited state is very rapid (in $\sim 10^{-12}$ - 10^{-13} sec). The Onsager model is therefore physically unrealistic and also generates unrealistically large values of r_0 . Hong and Noolandi and Braun⁶¹ modified Onsager's theory to depict charge generation in organic photoconductors [Fig. 5.18(b)]. The model allows for the rapid relaxation of a photogenerated excitation to its lowest excited state during which it losing its excess energy. The lowest excited state of the molecule is assumed to have a long lifetime ≥ 1 nsec. Carrier separation from the lowest excited state is now an additional de-excitation pathway in addition to the radiative and nonradiative decays of the molecule. The modified Onsager theory leads to smaller values for r_0 and accounts for the energy-independent charge generation efficiency. The electric field dependence of the charge generation efficiency for the modified Onsager model has a similar shape to the original model. The modified model may do a better job fitting the experimentally higher photocurrents at lower fields and the more rapid increase of the photocurrent at higher fields.

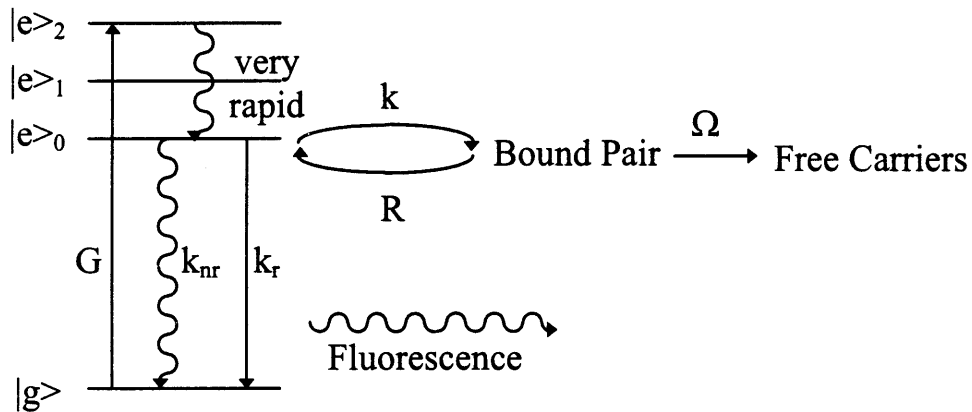
The charge generation efficiency

$$\eta(E) = \frac{\bar{k}(E)}{\bar{k}(E) + k_{nr} + k_r} \quad (5.6)$$

where $\bar{k}(E)$ is the average, field-dependent charge generation rate and k_r and k_{nr} are the radiative and nonradiative decay rates (assumed to be weakly field dependent). The fluorescence intensity for the molecule is described by



(a)



(b)

Figure 5.18 (a) Onsager model for charge carrier generation where carriers are generated from their photoexcited state and lose excess energy by collisions with the medium. (b) Modified Onsager model for charge carrier generation where carriers rapidly thermalize to their lowest excited state before carrier separation. $|g\rangle$ represents the ground state and the $|e\rangle_i$'s the excited states of a molecule. G is the generation rate of photoexcitations, k_r and k_{nr} are the radiative and nonradiative decay rates, respectively. η_∞ is the fraction of carriers escaping the excited molecule in (a) and k is the rate at which carriers escape to neighboring molecules in (b). Ω is the probability of generating free carriers and $R = 1 - \Omega$ is the probability of carrier recombination due to their Coulomb attraction.

$$I(E) = \frac{k_r}{k_r + k_{nr}} [1 - \eta(E)]G \quad (5.7)$$

where G is the rate of photoexcitation. The PL quantum yield for the molecule is quenched by the applied field as

$$\frac{\Delta I}{I(0)} = \frac{I(0) - I(E)}{I(0)} = \frac{\eta(E) - \eta(0)}{1 - \eta(0)}. \quad (5.8)$$

The modified Onsager model is consistent with the physics of our QD samples and our photoconductivity measurements. As we discussed above, our QDs show that photogenerated excitations rapidly relax from the higher excited states to the lowest excited state in the QDs in a time of $\sim 10^{-12}$ sec¹¹. The lifetime of the lowest excited state in the QDs is > 1 nsec, increasing with decreasing temperature and decreasing QD size¹¹. The photoconductivity spectral response for the QD solids reveals a carrier generation efficiency independent of the energy of photoexcitation. Higher energy excitations generated in the QDs rapidly thermalize to the lowest excited state, showing no signs of hot carrier effects. The possible dominance of field-assisted charge separation in our QD solids is also consistent with the linear dependence of the photocurrent with incident intensity. For a given charge generation efficiency, increasing the incident photon flux increases the generation rate of photoexcitations which are then separated into free carriers with the efficiency of carrier generation.

The anomalous temperature dependence of the photocurrent may also be explained by the modified Onsager model. An increase in photocurrent with increasing temperature is commonly observed in photoconductive materials as thermal energy overcomes the activation barrier to carrier generation. A general functional form for either the photocurrent or carrier efficiency without an external field is^{25,28}

$$\phi(0) = \phi_0 \exp\left(-\frac{E_a}{kT}\right) \quad (5.9)$$

where for the modified Onsager model $E_a = \frac{e^2}{\epsilon r_0}$ ⁶¹. This suggest that E_a should increase with r_0 and therefore the diameter of the QD. The external field acts to reduce the barrier

for photoconductivity, in a simple approximation from Eq. (5.3)-(5.6) as $\exp\left(\frac{E}{kT}\right)$. So a larger applied field will be needed at lower temperatures to overcome the activation barrier. This is seen experimentally as the temperature of maximum photocurrent increases with decreasing voltage.

The anomaly in the temperature dependence of the photocurrent is its decrease at higher temperatures. Eq. (5.6) shows that the efficiency of charge generation is inversely proportional to the radiative and nonradiative decay rates. Figures 5.19 and 5.20 show the temperature dependence of the absorption and emission spectra for the 41.4 Å and 49.5 Å CdSe QD solids. The absorption spectra for the QDs shift to lower energy as does bulk CdSe [see Chapter 2] and the lines become thermally broadened with increasing temperature. In emission these same trends are also true, but most notably the luminescence intensity decreases dramatically with increasing temperature. Calculating the temperature dependence of the PL quantum yield for each of the QD solids, inset in Figures 5.19(b) and 5.20(b), reveals an exponential decrease with increasing temperature as the nonradiative rate of decay increases. The radiative rate may also change as a function of temperature. The radiative rate is proportional to the oscillator strength of the emitting state⁶². Luminescence studies of our QDs are consistent with theoretical models of fine structure in the first excitonic state¹¹. The first exciton is split into five states with the lowest energy state being optically dark and separated from an optically bright state by a size-dependent energy splitting, ranging from ~2-12 meV over the complete size range of QDs (17 to 150 Å in diameter). As the temperature increases the radiative rate may also increase as the optically allowed state, which carries larger oscillator strength, is thermally repopulated. Therefore as the radiative and nonradiative rates increase with temperature, the charge generation rate will decrease consistent with the observed decrease in photocurrent with increasing temperature. The anomalous temperature dependence is consistent with a thermally activated process which leads to an initial increase in carrier generation with increasing temperature which is overcome at higher temperatures by the decrease in lifetime (equivalent lifetime of radiative and nonradiative processes) of the excitation, resulting in a decrease in carrier generation.

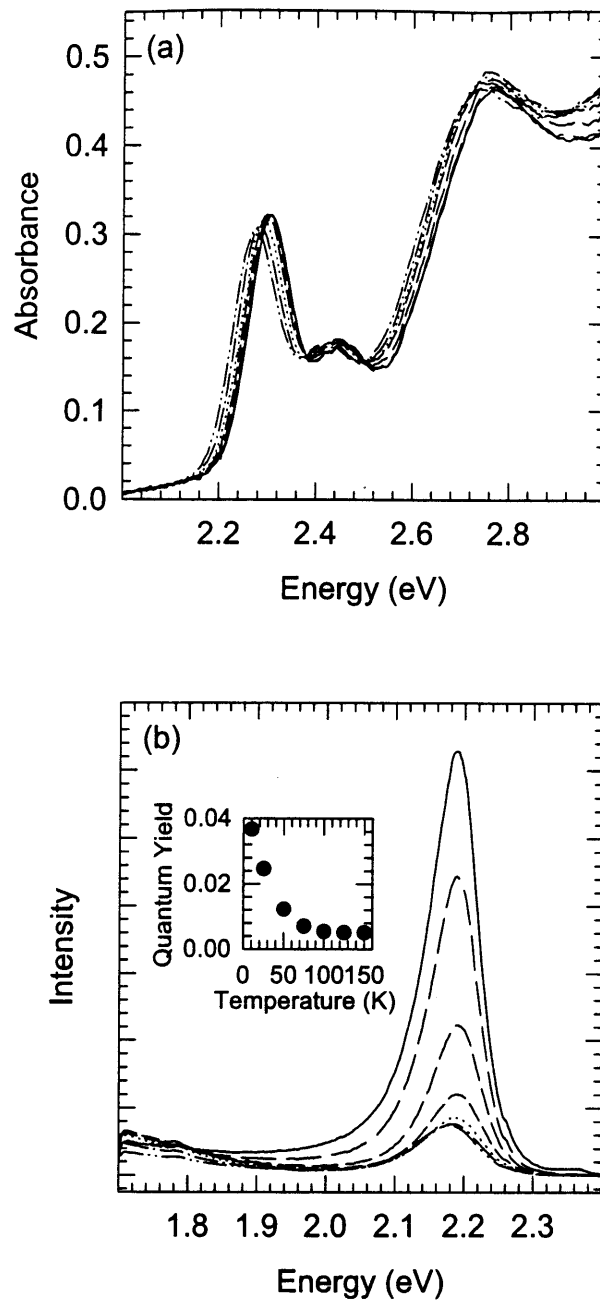


Figure 5.19. Temperature dependence of the (a) absorption and (b) emission spectra for a 41.4 Å CdSe QD solid. The spectra were taken at 10 K (solid line), 25 K (long dashes), 50 K (medium dashes), 75 K (short dashes), 100 K (dotted line), 125 K (dash-dot line), and 150 K (dash-two dots line). The inset in (b) shows the exponentially decreasing PL quantum yield for the QD solid with increasing temperature.

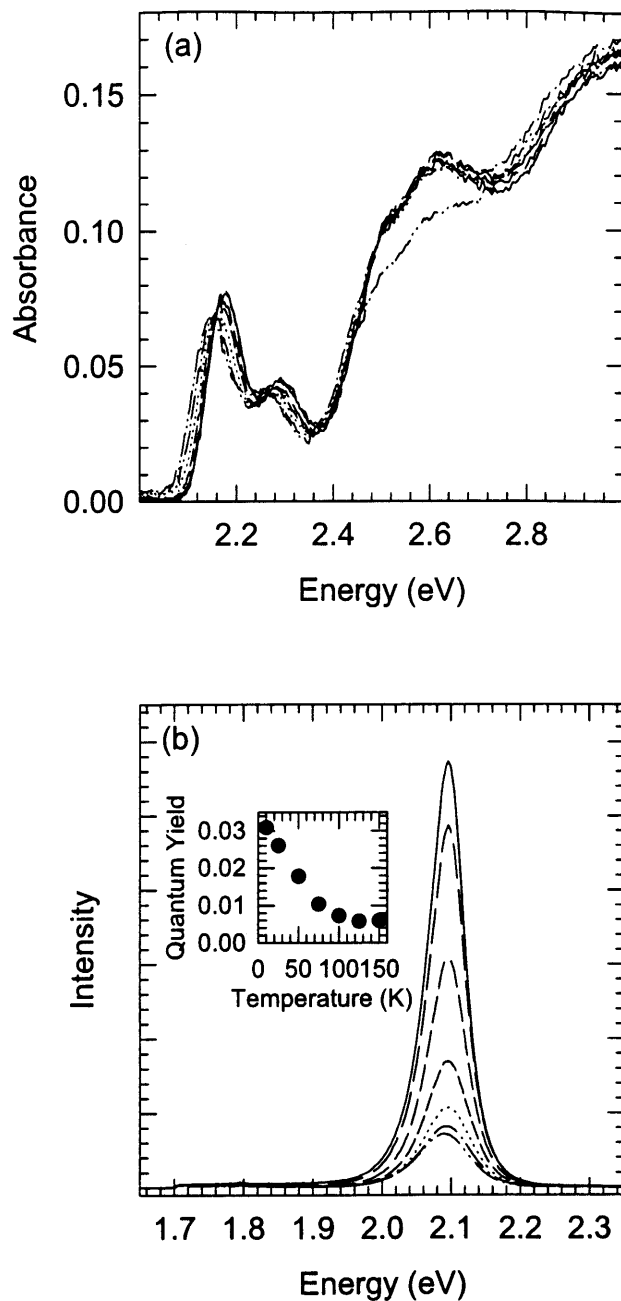


Figure 5.20 Temperature dependence of the (a) absorption and (b) emission spectra for a 49.5 Å CdSe QD solid. The spectra were taken at 10 K (solid line), 25 K (long dashes), 50 K (medium dashes), 75 K (short dashes), 100 K (dotted line), 125 K (dash-dot line), and 150 K (dash-two dots line). The inset in (b) shows the exponentially decreasing PL quantum yield for the QD solid with increasing temperature.

Figure 5.15 shows that the electric field acts to quench the PL quantum yield of the QD solid for excitation to the blue of the first exciton and is ineffective for excitation in the red tail of the absorption spectrum. Sacra has seen the same trends in Stark luminescence measurements for the QDs dispersed in poly(vinyl butyral)⁶³. One hypothesis is that the PL quantum yield is quenched by field-assisted trapping of carriers in the polymer matrix. This is consistent with the picture of field-assisted carrier separation here where now the carriers may be transported through the QD solid and collected at the Au electrodes. Although only a fraction (~40%) of the QDs are affected by the field, the decrease in the PL quantum yield for the QD solid is not dramatic suggesting that carrier separation may be very difficult. Photoexcitation in the red tail of the absorption spectrum excites only the largest QDs, a small fraction of the QDs in the solid. This is similar to having the QDs dilute in the polymer matrix which also shows that the electric field does not effect the PL quantum yield. Carrier separation and transport may also be “turned off” since carriers cannot tunnel into dots with higher energy states. In general, independent of mechanism, carrier separation will decrease the PL quantum yield as the electron and hole will no longer reside in the same QD to recombine radiatively.

In summary, the Onsager model for carrier separation is consistent with the nonlinear I-V characteristics, the energy-independent carrier generation efficiency from the spectral response, the linear dependence of current with incident intensity, the anomalous temperature dependence of the photocurrent, and the quenching of the PL quantum yield with applied field.

5.4.3 The Scaling Law for Collective Transport of Carriers

Single electron tunneling effects in junctions containing single metal or semiconductor QDs have generated a lot of interest⁴. At low temperatures, Coulomb blockade effects exist. In order to observe the Coulomb blockade both thermal fluctuations and quantum fluctuations in the system must be small enough. The

temperature of the junction must be low enough so that $kT < E_C = \frac{e^2}{2C}$, the charging energy associated with tunneling of a single electron⁴. C is the capacitance of the junction. The tunnel resistance of the junction, R_T , must also be large enough so $R_T \gg R_Q = \frac{h}{e^2}$, the resistance quantum. A voltage V such that $eV > E_C$ must be applied to overcome the charging energy of the electron and enable single electron tunneling. The I-V characteristics for the junction shows a Coulomb staircase associated with the tunneling of single electrons. At each step, the voltage applied must overcome the charging energy associated with tunneling of another electron. This voltage is known as the Coulomb gap, $V = \frac{e}{2C}$. The Coulomb staircase has been observed in junctions containing a metal or semiconductor QD^{50,51}. For a CdSe QD coordinated by trioctylphosphine chalcogenides, the Coulomb staircase has been observed up to liquid nitrogen temperatures. At 4 K, a Coulomb gap ranging from 110 to 200 mV has been measured⁵¹.

Under the same constraints required to see the Coulomb blockade in single QDs, nonlinear I-V characteristics have recently been theoretically predicted and experimentally realized in one- and two-dimensional arrays of metal QDs^{52,64,65}. The I-V curves show a conduction gap below which little current flows. The threshold to conduction is proportional to the size of the QD array⁶⁶. Above this threshold, the I-V characteristics are shown to follow the scaling law

$$I \propto \left(\frac{V}{V_T} - 1 \right)^\zeta \quad (5.10)$$

where V_T is the threshold voltage. In one- and two-dimensional arrays of Al QDs, the exponent ζ is found to be 1.36 ± 0.01 in 1D and 1.80 ± 0.16 in 2D⁶⁴. The one- and two-dimensional arrays have 440 dots and 38×38 dots respectively. Theoretical predications for arrays of finite size set ζ at 1 and 2, for 1D and 2D arrays respectively⁶⁶. For infinite arrays, the value of ζ is found to be 1 and $5/3$ for the 1D and 2D cases⁶⁶.

We calculated the scaling law for our QD solids using the nonlinear I-V curves at 10 K for each of the QD solids. Figure 5.17 plots the scaling law for each of the QD solids in dotted lines. The curves are found using a value of $\zeta = 2.6$ and changing the threshold voltages. A threshold voltage of 150 V was found for the 41.4 Å QD solid and 90 V for the 49.5 Å QD solid. The curves are scaled and expressed in terms of the electric field to give comparison to the Onsager model. The scaling law does a very good job at reproducing the nonlinear behavior of the experimental I-V curves. The value for ζ is consistent with the trend of increasing ζ with increasing dimension. No experimental or theoretical predictions of I-V characteristics in three-dimensional QD solids are available for comparison.

The threshold voltage is predicted to scale linearly with the size of the array. The decrease in threshold voltage with increasing dot diameter is consistent with the decrease in the number of QDs spanning the electrodes. This assumes that conduction takes place in the plane of the film across which the voltage is applied and that there is little conduction perpendicular to the applied field.

5.4.4 Tunneling

In our QD solids each of the dots represents a potential well for carriers that is bound at the surface by the organic capping groups. In Chapter 4, we observe that in luminescence the spectra are inhomogeneously broadened as the QDs in the samples have a distribution in emitting energies. If we assume that the inhomogeneous distribution in emitting energies represents the distribution of lowest electronic states for the QDs in the samples, we can represent the energies of the lowest electronic states by Gaussian distributions with standard deviations $\lesssim 30$ meV. In the QD solid, the energy of the electronic states in the dots will have a distribution in energy, similar to localized states in amorphous and organic solids^{67,68}. With the voltage applied, the voltage drop across each dot is $\sim \frac{1}{8}$ eV. The energy of the lowest electronic level in the dots will decrease monotonically from one electrode to the other as the voltage drop across each dot is larger than the variation in the energy of the lowest electronic state for the QDs in a

sample. This is pictured in Figure 5.16. A carrier in a QD may resonantly tunnel to a state in a neighboring QD. This state in the neighboring dot may be a higher electronic or vibrational excited state. The carrier may emit LO- and/or acoustic phonons to thermalize to the lowest electronic and vibrational state of the QD. The organic cap coordinating the QD surface represents a potential barrier with a height of ~ 1.5 eV with a width of 11 Å.

I-V curves collected for CdSe/SeTe and CdSe/Se multilayers show similar behavior as those for the QD solids⁶⁸. At sufficiently high fields, the current increases rapidly as carriers tunnel through the multilayers. The I-V curves for the multilayers follow the Fowler-Nordheim equation⁶⁸⁻⁷⁰

$$I \propto E^2 * \exp\left(-\frac{\beta}{E}\right) \quad (5.11)$$

where $\beta = \frac{4(2m^*)^{1/2}(2\phi_b)^{3/2}}{3e\hbar E}$, m^* is the effective mass of the electron (hole), E is the electric field, and ϕ_b is the height of the barrier. The Fowler-Nordheim equation describes field emission, the quantum mechanical tunneling of electrons through a potential barrier from a metal to a semiconductor or an insulator^{69,70}. Field emission is particularly important at low temperatures where thermal excitation of the carriers is less probable. In Figure 5.17 the dashed lines show the Fowler-Nordheim curves fit to the 10 K I-V curves for both the 41.4 Å and 49.5 Å CdSe QD solid. The shape of the Fowler-Nordheim curve reproduces the nonlinear behavior of the I-V curves for the QD solids, but with value of ϕ_b for electrons of ~ 14 eV and 18 eV at $E = 50000$ V/cm. The shape of the potential barrier used to calculate Eq. 5.11 is triangular, representing the slope in an insulator or a semiconductor at a metal interface. Calculating the current generated by tunneling through a square potential may reproduce the physical height and thickness of the potential representing the organic cap.

5.4.5 Exciton Interaction with Electrodes

Excitons may interact with a metal electrode and dissociate^{69,71}. In Fig. 5.5 we showed that focusing the beam between the two electrodes yields a photocurrent similar in magnitude to that when we illuminate the active region of the QD solid and the electrodes. In molecular solids, energy transfer by exciton diffusion transfers excitations through the solid to the solid/electrode interface where the exciton may interact with the electrode and dissociate^{69,71}. The free carrier may then tunnel from the molecular solid into the electrode, generating a photocurrent. In Chapters 3 and 4, we showed that energy transfer between QDs proceeded by long-range resonance transfer and is only a nearest neighbor interaction. The efficiency of energy transfer in the QD solids is not sufficient to transport the excitation through the QD solid to the interface with the Au electrodes.

5.4.6 Two Quantum Processes

Free carriers can also be generated by exciton-exciton, photon-photon, and exciton-photon interactions⁶⁹. In our experiments, the intensity of the excitation is weak. Depending on the temperature and therefore the lifetime of the excitation in the QD, the density of QDs excited at a given time in the QD solid is on the order of 10^{-5} to 10^{-6} , making two quantum processes unlikely. Recent measurements on the statistics of the emission from a single QD suggest autoionization of an exciton by interaction between a photon and an exciton occurs with an efficiency of 10^{-6} ⁷². This efficiency is two orders of magnitude smaller than the extrinsic efficiency of photocarrier generation.

5.4.7 Multiple Trapping Model

Nonlinear I-V curves observed in photocurrent measurements of molecular and inorganic solids have also been explained by a multiple trapping model^{25,26}. Multiple

trapping has also been used explain the nonlinear behavior of I-V characteristics collected in the dark^{25,69,73}. It is applied to insulating materials containing bulk trapping sites that have single carrier transport and injecting electrical contacts. Below the threshold voltage, it is assumed that bulk trapping sites are filled by thermally generated carriers in the bulk of the material at low voltages and that space charge limited currents cause carrier injection from the electrodes at higher applied voltages. At the threshold voltage, known as the trapped filled limit, the traps in the bulk of the material are filled and the current rises steeply. The trapped filled limit has been correlated to the density of trap sites in the bulk of the material.

The dark current for the QD solids is within the noise of the electrometer. It is not possible to observe the behavior of the I-V curve and therefore the effects of the electrodes on the measured I-V characteristics. It seems unlikely that if injection of carriers from the electrodes is large enough to fill the traps, that is not possible to measure any current even at high voltages. If carrier separation is easy and photocarriers initially fill traps, the threshold voltage in the I-V curves should shift to lower voltages with increasing photon fluxes. In Figure 5.9 we see a single I-V curve that is scaled by the photon flux.

5.4.8 Polarization

Depletion regions within a photoconductor can be created if there is a difference in mobility of photogenerated electrons and holes. The current generated by the more mobile carrier will cease when the applied field is counterbalanced by the field created by the relatively immobile oppositely charged carrier⁷⁴. In our QD solids we do not observe a decrease in current over time. The I-V curves taken over as much as half an hour are symmetric, indicating that the photocurrent does not decrease over time. The photocurrent has also been monitored at constant applied voltage and incident intensity over many minutes with no signs of decrease. The photoluminescence QY of QDs has been shown to decrease when the QDs are charged. In Figure 5.15 we see that the photoluminescence QY for the QD solids with a field applied shows only a small

decrease relative to the QY without an applied field. If one of the carriers is significantly more immobile, the photoluminescence QY for the QD solid would decrease significantly.

5.5 Conclusion

We demonstrate photoconductivity in close packed CdSe QD solids. The spectral response of the photocurrent maps out the absorption spectrum for the QDs, revealing that the QDs are responsible for carrier generation in the QD solids. The energy-independent carrier generation efficiency indicates photoexcitations created in higher excited states rapidly thermalize to the lowest excited state in each QD prior to carrier separation. The linear dependence of the photocurrent with incident intensity is consistent with a photocurrent that is the product of the carrier generation efficiency and the photon flux. For a photon flux of $10^{16} \frac{\text{photons}}{\text{cm}^2 \cdot \text{sec}}$ exciting a QD solid with an optical density of 0.1 and an active area of $1.6 \times 10^{-4} \text{ cm}^2$, we measure a charge generation efficiency of $\sim 5 \times 10^{-4}$. The photocurrent exhibits an anomalous temperature dependence, exhibiting a maximum photocurrent at $\sim 75 \text{ K}$. The temperature dependence is consistent with a thermally activated process, leading to an initial increase in photocurrent with increasing temperature, which is overcome at higher temperatures by the decrease in the exciton lifetime, decreasing the efficiency of carrier generation. Using a modified Onsager model, we show that the physics of the QDs and the dependence of the photocurrent on excitation energy, applied voltage, excitation intensity, and temperature is consistent with field-assisted charge separation in the QD solids. We also found that the nonlinear behavior of the I-V curves could be reproduced using the Scaling law for collective transport and the Fowler-Nordheim equation for carrier tunneling. The Scaling law accounts for a threshold voltage below which carrier tunneling is prohibited, requiring a large enough voltage to be applied to overcome the charging energy of the QDs in the solids. The shift in the threshold voltage increases as the number of QDs between the electrodes increases with decreasing dot diameter. The

Fowler-Nordheim equation describes tunneling of carriers by field emission. In the QD solids, the field ensures that a carrier may resonantly tunnel from one dot to a neighboring dot since the electronic levels in the neighboring dot are shifted to lower energy. The question remains whether the energy to separate the carriers, the energy to charge the QDs (accounting for the fact that photoexcitation promoted an electron into the conduction band and a hole into the valence band), or the probability of tunneling through the barrier is dominant.

Bibliography

1. C. Weisbush and B. Vinter, *Quantum Semiconductor Structures*, (Academic Press, Boston, 1991).
2. Al. L. Efros and A. L. Efros, *Fiz. Tekh. Poluprovodn.* **16**, 1209 (1982) [*Sov. Phys. Semicond.* **16**, 772 (1982)]; L. E. Brus, *J. Chem. Phys.* **80**, 4402 (1984).
3. D. J. Norris, A. Sacra, C. B. Murray, and M. G. Bawendi, *Phys. Rev. Lett.* **72**, 2612 (1994); D. J. Norris, Ph.D. Thesis, Massachusetts Institute of Technology, 1995.
4. M. A. Kastner, *Physics Today*, **46(1)**, 24 (1993).
5. C. B. Murray, D. J. Norris, and M. G. Bawendi, *J. Am. Chem. Soc.* **115**, 8706 (1993).
6. A. I. Ekimov, F. Hache, M. C. Schanne-Klein, D. Ricard, C. Flytzanis, I. A. Kudryavtsev, T. V. Yazeva, A. V. Rodina, and Al. L. Efros, *J. Opt. Soc. Am. B*, **10**, 100 (1993).
7. J. E. Bowen Katari, V. L. Colvin, and A. P. Alivisatos, *J. Phys. Chem.* **98**, 4109 (1994); L. R. Becerra, C. B. Murray, R. G. Griffin, and M. G. Bawendi, *J. Chem. Phys.* **100**, 3297 (1994).
8. D. J. Norris and M. G. Bawendi, *J. Chem. Phys.* **103**, 5260 (1995).
9. D. J. Norris and M. G. Bawendi, *Phys. Rev. B*, **53**, 16338 (1996).
10. D. J. Norris, Al. L. Efros, M. Rosen, and M. G. Bawendi, *Phys. Rev. B.*, **53**, 16347 (1996).
11. Al. L. Efros, M. Rosen, M. Kuno, M. Nirmal, D. J. Norris, and M. G. Bawendi, *Phys. Rev. B*, **54**, 1 (1996); M. Nirmal, D. J. Norris, M. Kuno, M. G. Bawendi, Al. L. Efros, and M. Rosen, *Phys. Rev. Lett.*, **75**, 3728 (1995); M. Nirmal, C. B. Murray, and M. G. Bawendi, *Phys. Rev. B* **50**, 2293 (1994); M. G. Bawendi, P. J. Carroll, W. L. Wilson, and L. E. Brus, *J. Chem. Phys.*, **96**, 946 (1992).
12. S. A. Empedocles, D. J. Norris, and M. G. Bawendi (submitted).
13. L. W. Banyai and S. W. Koch, *Semiconductor Quantum Dots*, (World Scientific Series on Atomic, Molecular, and Optical Physics, New Jersey, 1993), p. 205.
14. D. Heitmann and J. P. Kotthaus, *Physics Today* **46(6)**, 56 (1993).
15. R. Leon, P. M. Petroff, D. Leonard, and S. Farad, *Science* **267**, 1966 (1995).
16. C. B. Murray, C. R. Kagan, and M. G. Bawendi, *Science* **270**, 1335 (1995).
17. T. Vossmeier, G. Reck, L. Katsikas, E. T. K. Haupt, B. Schulz, and H. Weller, *Science*, **267**, 1476 (1995).
18. C. B. Murray, C. R. Kagan, and M. G. Bawendi, to be published.
19. F. Capasso, C. Sirtori, and A. Y. Cho, *IEEE J. Quantum Electron.* **22**, 1853 (1986); R. Ferreira *et al.*, *Phys. Rev. B* **45**, 11782 (1992).
20. V. M. Agranovich and M. D. Galanin, *Electronic Excitation Energy Transfer in Condensed Matter*, (North-Holland Publishing Company, New York, 1982). Th. Förster, in *Comparative Effects of Radiation*, edited by M. Burton, J. S. Kirby-Smith, and J. L. Magee, (Wiley, New York, 1960), p. 301; D. L. Dexter, *J. Chem. Phys.* **21**, 836 (1953).
21. M. W. Windsor, in *Physics and Chemistry of the Organic Solid State*, Vol. 2 (Intersciences, New York, 1965), p. 343.
22. A. A. Lamola, in *Energy Transfer and Organic Photochemistry*, Vol. 14 (Intersciences, New York, 1969), p.17.

23. C. R. Kagan, C. B. Murray, M. Nirmal, and M. G. Bawendi, *Phys. Rev. Lett.*, **76**, 1517 (1996).
24. C. R. Kagan, C. B. Murray, and M. G. Bawendi, *Phys. Rev. B*, in press.
25. A. Rose, *Concepts in Photoconductivity and Allied Problems*, (Wiley, New York, 1963); R. H. Bube, *Photoconductivity of Solids*, (Wiley, New York, 1960).
26. H. Inokuchi and Y. Maruyama, in *Photoconductivity and Related Phenomena*, edited by J. Mort and D. M. Pai, (Elsevier Scientific Publishing Co., New York, 1976), p. 155.
27. F. Capasso, K. Mohammed, A. Y. Cho, R. Hull, and A. L. Hutchinson, *Phys. Rev. Lett.*, **55**, 1152 (1985); F. Capasso, K. Mohammed, and A. Y. Cho, *Physica*, **134B**, 487 (1985).
28. J. Kommandeur, *J. Phys. Chem. Sol.*, **22**, 339 (1961).
29. B. O. Dabbousi, C. B. Murray, M. F. Rubner, and M. G. Bawendi, *Chem. Mater.*, **6**, 216 (1994).
30. C. B. Murray, Ph.D. Thesis, Massachusetts Institute of Technology, 1995.
31. A. Guinier, *X-ray Diffraction*, (Dover Publications, Inc., New York, 1994), p.319.
32. H. P. Klug and L. E. Alexander, *X-ray Diffraction Procedures*, (Wiley, New York, 1954), p. 586.
33. W. K. Burton, N. Cabrera, and F. C. Frank, *Phil. Trans. Roy. Soc. London*, **A243**, 299 (1950).
34. Y. P. Varshni, *Physica*, **34**, 149 (1967).
35. *Landolt-Bornstein Numerical Data and Functional Relationships in Science and Technology*, New Series, Group III, Vol. 17b, edited by K. H. Hellwege (Springer-Verlag, Berlin, 1982).
36. T. Vossmeier, L. Katsikas, M. Giersig, I. G. Popovic, K. Diesner, A. Chemseddine, A. Eychmuller, and H. Weller, *J. Chem. Phys.*, **98**, 7665 (1994).
37. V. Colvin, M. Schlamp, and A. P. Alivisatos, *Nature* **370**, 354 (1994); B. O. Dabbousi, M. G. Bawendi, O. Onitsuka, and M. F. Rubner, *Appl. Phys. Lett.* **66**, 11 (1995).
38. L. Brus, *Appl. Phys. A* **53**, 465 (1991).
39. T. Takagahara, *Optoelect. Dev. Tech.* **8**, 545 (1993); T. Takagahara, *Surf. Sci.* **267**, 310 (1992); Y. Kayanuma, *J. Phys. Soc. Jpn.* **62**, 346 (1993).
40. R. C. Powell, *J. Lumin.* **11**, 1 (1975); S. I. Golubov and Yu. V. Konobeev, *Phys. Stat. Sol. (B)* **79**, 79 (1977).
41. S. Lloyd, *Science*, **261**, 1569 (1993).
42. Y. Arakawa and T. Takahashi, *Optoelectronics* **3**, 155 (1988); Y. Arakawa in *Confined Electrons and Photons*, edited by E. Burstein and C. Weisbuch, Series B: Physics Vol. 340, (Plenum Press, New York, 1995), p.647; R. Ugajin, *J. Appl. Phys.* **76**, 2833 (1994).
43. B. O'Regan and M. Grätzel, *Nature* **353**, 737 (1991); G. Redmond, D. Fitzmaurice, and M. Graetzel, *Chem. Mater.* **6**, 686 (1994); G. Hodes, I. D. J. Howell, and L. M. Peter, *J. Electrochem. Soc.* **139**, 3136 (1992).
44. *Dictionary of Organophosphorous Compounds*, edited by R. S. Edmundson (Chapman and Hall Ltd., New York, 1988), p.828.
45. J. I. Pankove, *Optical Processes in Semiconductors*, (Dover Publications, Inc., New York, 1971), p. 89.

46. G. Liu and J. E. Guillet, *Macromolecules*, **23**, 1388 (1990).
47. C. R. Kagan, C. B. Murray, and M. G. Bawendi, *Mat. Res. Soc. Symp. Proc.*, **358**, 219 (1995); L. Spanhel and M. A. Anderson, *J. Am. Chem. Soc.* **112**, 2278 (1990).
48. T. Pullerits and A. Freiberg, *Chem. Phys.*, **149**, 409 (1991); T. Pullerits and A. Freiberg, *Biophys. J.*, **63**, 879 (1992); O. J. G. Somsen, F. van Mourik, R. van Grondelle, and L. Valkunas, *Biophys. J.*, **66**, 1580 (1994).
49. V. A. Markel, V. L. Shalaev, E. B. Stechel, W. Kim, and R. L. Armstrong, *Phys. Rev. B*, **53**, 2425 (1996).
50. H. van Kempen, J. G. A. Dubois, J. W. Gerritsen, and G. Schmid, *Physica B*, **204**, 51 (1995).
51. D. L. Klein, P. L. McEuen, J. E. Bowen Katari, R. Roth, and A. P. Alivisatos, *Appl. Phys. Lett.*, **68**, 2574 (1996).
52. D. B. Janes, V. R. Kolagunta, R. G. Osifchin, J. D. Bieldfeld, R. P. Andres, J. I. Henderson, and C. P. Kubiak, *Superlatt. and Microstruct.*, **18**(4), 275 (1995); R. Houbertz, T. Feigen span, F. Mielke, U. Memmert, U. Hartmann, U. Simon, G. Schön, and G. Schmid, *Europhys. Lett.*, **28**, 641 (1994).
53. Y. Wang, in *Advances in Photochemistry*, edited by D. C. Neckers, D. H. Volman, and G. von Bunau, vol. 19, 179 (1995).
54. W. Hoheisel, V. L. Colvin, C. S. Johnson, and A. P. Alivisatos, *J. Chem. Phys.*, **101** 8455 (1994).
55. W. D. Gill, in *Photoconductivity and Related Phenomena*, edited by J. Mort and D. M. Pai, (Elsevier Scientific Publishing Co., New York, 1976), p. 303.
56. J. Mort, M. Machonkin, R. Ziolo, and I. Chen, *Appl. Phys. Lett.*, **61** (15), 1829 (1992).
57. D. M. Pai and R. C. Enck, *Phys. Rev. B* **11**, 5163 (1975).
58. L. Onsager, *Phys. Rev.* **54**, 554 (1938); A. Mozumder, *J. Chem. Phys.*, **60**, 4300 (1974).
59. J. Lee (private communication).
60. *CRC Handbook of Chemistry and Physics, 71st Edition*, edited by D. R. Lide, (CRC Press, Boston, 1991), p.12-84.
61. J. Noolandi and K. M. Hong, *J. Chem. Phys.*, **70**(7), 3230 (1979); R. H. Batt, C. L. Braun, and J. F. Hornig, *H. Chem. Phys.*, **49**(4), 1967 (1968).
62. J. I. Steinfeld, *Molecules and Radiation*, (The MIT Press, Cambridge, 1974), p.29.
63. A. Sacra, Ph.D. Thesis, Massachusetts Institute of Technology, 1996.
64. A. J. Rumberg, T. R. Ho, and J. Clarke, *Phys. Rev. Lett.*, 4714 (1995).
65. R. Houbertz, T. Feigen span, F. Mielke, U. Memmert, U. Hartmann, U. Simon, G. Schön, and G. Schmid, *Europhys. Lett.*, **28**, 641 (1994).
66. A. A. Middleton and N. S. Wingreen, *Phys. Rev. Lett.*, **71**, 3198 (1993).
67. N. F. Mott and E. A. Davis, *Electronic Processes in Non-crystalline Materials*, (Clarendon Press, Oxford, 1979), p.32.
68. K. C. Kao and W. Hwang, *Electrical Transport in Solids*, (Pergamon Press, New York, 1981).
69. R. Ionov, D. Nesheva, D. Arsova, *J. Non-Cryst. Sol.*, **137 && 138**, 1151 (1991).
70. R. H. Fowler and L. Nordheim, *Proc. Roy. Soc. (London)*, **119A**, 173 (1928).
71. H. Killesreiter and H. Baessler, *Chem. Phys. Lett.*, **11**, 411 (1971).

72. M. Nirmal, B. O. Dabbousi, M. G. Bawendi, J. J. Macklin, J. K. Trautman, T. D. Harris, and L. E. Brus, submitted.
73. P. Roussignol, D. Ricard, D. Likasik, and C. J. Flytzanis, *J. Opt. Soc. Am. B*, **4**, 5 (1987).
74. M. Campos, *Molecular Crystals and Liquid Crystals*, **18**, 105 (1972).
75. J. C. Scott, L. Th. Pautmeier, and W. E. Moerner, *J. Opt. Soc. Am. B*, **9**, 2059, (1992).

Acknowledgments

This thesis would not have been possible without the guidance and instruction of many professors and teachers. As a young student my behavior was less than exemplary. Fortunately my teachers saw beyond my behavior and believed I was capable of more than my performance made obvious. Mrs. Alice Garr had ideas about my potential accomplishments that at age 13, I couldn't conceive. Mrs. Gloria Weiss tried to discipline me by subjecting me to "work detail," teaching me the fine art of cleaning glassware in her chemistry lab after school. My high school guidance counselor, Marjorie Jacobs, took the time to talk and learn about my interests and to lead me in the right direction.

Professor Peter K. Davies my undergraduate academic and thesis advisor gave me the opportunity to experience what it was like to do research. After expressing his disappointment in my academic performance, he asked me if I was interested in working for a professor in the Materials Science and Engineering department. Sure, why not. He then informed me that I was now working for him. It was an invaluable experience for a student unsure about which career path to follow. He also set a tacit expectation that I would earn A's in my classes.

Moungi gave me the opportunity to follow my interests and do research in his laboratory and to become a member of his group. He has always been patient and taken the time to talk through and think about ideas and experiments. His enthusiasm about science has really made doing research a lot of fun. I also thank him for wishing me luck before I was about to run an experiment.

I have really enjoyed working with fellow members of the Bawendi group -- Chris Murray, Manoj Nirmal, David Norris, Ann Sacra, Bashir Dabbousi, Fred Mikulec, Ken Kuno, Stephen Empedocles, Catherine Leatherdale, Dimitry Dinega, and Jinkyu Lee. Discussions with them have made the long days in the lab interesting.

Mike Frongillo, Neil Rowlands, Joe Walsh, and Rich Perilli took the time to teach me how to operate equipment in central facilities at MIT. Felice Frankel emphasized the importance of color and composition in communicating scientific information using images.

Most important to me are my friends and family. It is their support that is the key to my accomplishments and it is the time that we share that is central to my happiness. My friends Laura, Jessica, Chris, and Ann have made the time I have spent in graduate school really enjoyable and have always been there when I needed advice. My parents and sister although not quite sure what it is that I am doing have been very supportive of my efforts. My mom is always there for those important questions, like what do I wear? My dad always reminds me that if a career in science doesn't work out I can spend 6 months in California becoming a certified American Gemologist. My sister and I became friends during graduate school -- she lived down the block for 4 of those years.